ABSTRACT

Wireless Propagation Channel Modeling and Antenna Design for On-Body Applications

Dong Xue, Ph.D.

Mentor: Yang Li, Ph.D.

The Wireless Body Area Networks (WBAN) is promising in a variety of applications, such as remote health monitoring and assisted living. A typical WBAN consists of wearable body sensor units (BSU) and a body control unit (BCU). The BCU can receive physiological signal data from the BSUs and relay them to a remote access point regarding impending emergencies. One important issue in implementing a WBAN is to ensure reliable and efficient wireless communication links on a human body. This is particularly challenging since the human body represents a difficult propagation environment where body tissues introduce high loss to electromagnetic waves propagating along, around and through the body. The antenna radiation performance may also be affected due to the presence of the human body.

Extensive research involving on-body propagations have been conducted over the past decade through experiments, simulations and theories. However, most studies focus only on signal strength attenuation loss of on-body waves at a single frequency on a non-moving human body. Wearable antennas have been designed for on-body applications, but most designs concentrate on optimizing conventional antenna performance on the human

body. It remains to be studied how to design compact antennas which can couple on-body wave mechanisms efficiently over a broad range of frequencies.

In this dissertation electromagnetic wave propagations over a broad frequency band (300 MHz - 3GHz) and within short ranges (< 50 cm) are investigated for on-body wireless channel communications. Experimental, simulation and theoretical methods are used to examine two scenarios: along and around the body surface. The study is conducted on both non-moving and moving human bodies. Both signal strength and phase delay are studied. Dominant propagation mechanisms are extracted and analyzed. An electrically-small wearable antenna as well as directive array are designed for on-body applications, and human body effects on antenna performance are discussed.

Wireless Propagation Channel Modeling and Antenna Design for On-Body Applications

by

Dong Xue, B.E.

A Dissertation

Approved by the Department of Electrical and Computer Engineering

_____

Kwang Y. Lee, Ph.D. Chairperson

Submitted to the Graduate Faculty of
Baylor University in Partial Fulfillment of the
Requirements for the Degree
of

Doctor of Philosophy

Approved by the Dissertation Committee

_____

Yang Li, Ph.D., Chairperson

_____

Charles Baylis, Ph.D.

_____

Randall Jean, Ph.D.

_____

Mike Thompson, Ph.D.

_____

Brian Garner, Ph.D.

Accepted by the Graduate School

May 2017

_____

J. Larry Lyon, Ph.D., Dean

Page bearing signatures is kept on file in the Graduate School.

TABLE OF CONTENTS

LIST OF FIGURES

LIST OF TABLES

LIST OF ABBREIVATIONS

AFD – Average Fade Duration

AR – Autoregressive

BCU – Body Control Unit

BMI – Body Mass Index

BSU – Body Sensor Unit

CST – Computer Simulation Technology

DTW – Dynamic Time Wrapping

EBG – Electromagnetic Band Gap

ECG – Electrocardiography

EEG – Electroencephalography

EM – Electromagnetic

EMG – Electromyography

ESPRIT – Estimation of Signal Parameters via Rotational Invariance Techniques

FCH – Folded Cylindrical Helix

FDTD – Finite Difference Time Domain

FSH – Folded Spherical Helix

GA - Genetic Algorithm

GTD – Geometrical Theory of Diffraction

HF – High Frequency

ISM – Industrial, Scientific and Medical

LCR – Level Crossing Rate

LOS – Line-of-Sight

MBANs – Medical Body Area Networks

MICS – Medical Device Radio communications

MMNs – Medical Micropower Networks

MOM – Method of Moments

NEC – Numerical Electromagnetic Code

NLOS – Non-Line-of-Sight

PCB – Printed Circuit Board

PEC – Perfectly Electrical Conducting

PIFA – Planar Inverted-F Antenna

PSO – Particle Swarm Optimization

QoS – Quality of Service

RF – Radio Frequency

RSSI – Radio Signal Strength Indication

RX – Receiver

SMA – Subminiature version A

TM – Transverse Magnetic

TX – Transmitter

UWB – Ultra-Wideband

VHF – Very High Frequency

VNA – Vector Network Analyzer

WBAN – Wireless Body Area Network

WMTS – Wireless Medical Telemetry System

ACKNOWLEDGMENTS

I would like to express my sincere gratitude to my advisor Dr. Yang Li, who gave me this great opportunity to do research and guided me to the field of Antennas and Propagation. His deep knowledge, patience and encouragement on my research have been the source of inspiration through my doctorate program, and will be constantly inspiring me in the pursuit of my future career. I would also like to thank to Dr. Brian Garner, for his kind help and support with my research project. I need to acknowledge that the hard work of past and current students from Antennas & Propagation Lab: Kyle Martin, Trae Liller, Michael Canova, Andrew Hoeckel, Erik Forrister, George Lee and Bin Xu, who contributed in some fashion to this work. I am grateful for Mr. Orr, Mr. Hynan, and Mrs. Kerr for their assistance during my school years. I wish to thank all my other dissertation committee: Dr. Baylis, Dr. Jean and Dr. Thompson, for their guidance with my proposal and research.

This study is supported in part by funds from the National Science Foundation and the Collaborative Faculty Research Investment Program of Baylor University, Baylor Scott & White Health and Baylor College of Medicine.

To my mother and father,

The reason of what I become today,

Thanks for your great support and continuous care

CHAPTER ONE

Introduction and Background Information

The motivation of this dissertation originates from recent development in wireless body area networks (WBAN) [1]. The work of this dissertation gives a comprehensive study of the interaction between the human body and wireless techniques from electromagnetic aspects, including electromagnetic wave propagation, dynamic wireless channel modeling, and wearable antenna design for on-body WBAN applications.

1.1 Overview of Wireless Body Area Networks (WBAN)

The emerging technology of WBAN is promising for a variety of applications such as healthcare, assisted living, sports and entertainments. A typical WBAN consists of one or more body sensor units (BSUs) and a single body control unit (BCU) [2-3], as can be seen in Fig. 1.1. The BSUs, such as electrocardiography (ECG) and accelerometer, can be implanted inside the body or surface-mounted on the body. They continuously collect physiological and kinematics data and send the data to the BCU. The BCU (e.g. a smart phone) is a data hub and can provide user interface for control and management of BSUs. It relays the information through a cellular or Wi-Fi link to an external network, such as a medical caregiver's computer center, realizing the goal of remote health monitoring [4].

In order to implement a highly-efficient and reliable WBAN, a number of technical challenges need to be addressed in the application layer, network layer and physical layer [5-8]. At the application layer level, safety is the first thing considered to prevent harm to the human body from a wearable or implanted sensor. The device must be miniaturized

and unobtrusive so it can be easily placed on the body or clothes. At the network layer level, the security and privacy are essential as they will protect sensitive personal information for users. Data storage ability is required to archive data for signal analysis. At the physical layer level, power consumption and signal outage need to be taken into account, which are closely related to battery life and data transmission reliability. Despite efforts for power saving, such as adaptive power control and low-power circuitry, currently, those large bulky batteries only last for several days, which is not enough for a long-term health care monitoring situation that requires need months or years [7-8]. Signal outage and data loss are also undesirable as they will affect Quality of Service (QoS) and real-time data delivery.

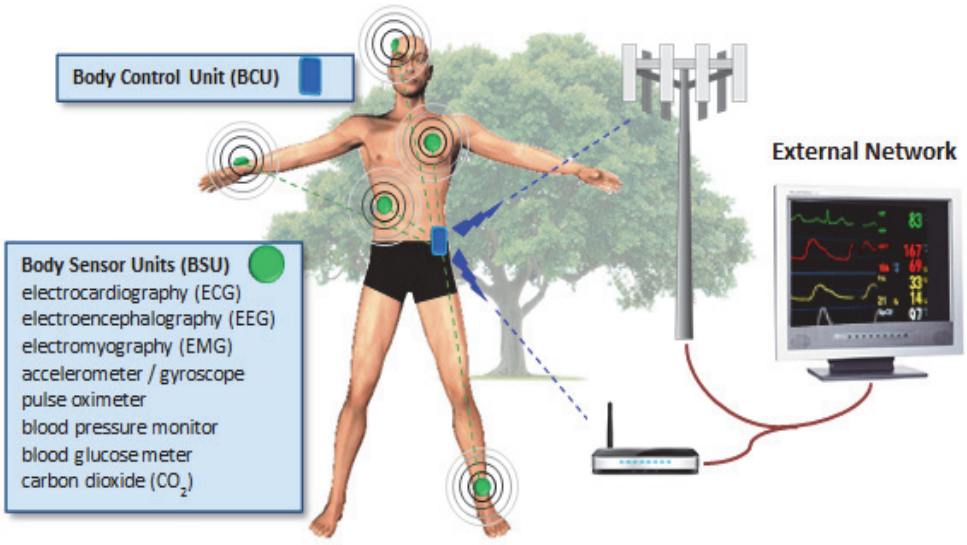

Fig. 1.1. The structure of WBAN. The body sensor nodes transmit physiological and motion data to the body control unit, which relay the information through Wi-Fi or cellular link to the external network, e.g. the medical center.

This dissertation will address two critical issues in WBAN physical layer design, namely, electromagnetic (EM) wave propagation and wearable antenna design for on-body wireless communications. Due to the presence of the human body and its movements, EM wave propagation will be scattered and diffracted from the body surface. The signal may be blocked and thus attenuate dramatically due to the body shadowing effect. Aspects of wearable antenna design in need of investigation are frequency detuning, pattern distortion and decreasing efficiency that may occur if an antenna is placed on the body surface. Although we mainly focus on the physical layer study, applicability will also be considered through the study, e.g. the miniaturization and flexibility for the antenna design. Our long-term goal is to reduce the wearable sensor's power consumption and avoid the signal outage. Therefore the sensor can have a long battery life and high data transmission reliability.

1.2 RF Frequency Bands and Standards for WBAN

In order to establish a reliable and efficient WBAN, the wearable device, e.g., medical device needs to provide accurate data transmission and low latency. Therefore, its operating frequency bands must be properly selected. Throughout the world there are several frequency bands that have been assigned to medical data transmission. Different countries have different criteria and certifications governed by regulatory agencies for the use of the medical data transmission. Table 1 listed below shows examples of RF frequency bands that are commonly used for wireless medical device production. In this dissertation 300 MHz - 3 GHz are chosen to cover all potential medical frequency bands.

Table 1. RF frequency bands for medical applications [9].

Standard	Frequency
Industrial, Scientific, and Medical bands (ISM)	13.553-13.567, 433.05-434.79, 902-928 MHz etc.
Wireless Medical Telemetry System (WMTS)	608-614, 1395-1400, 1427-1429.5 MHz
Medical Device Radio communications (MICS)	401-406 MHz
Medical Micropower Networks (MICS)	413-419, 426-432, 438-444, 451-458 MHz
Medical Body Area Networks (MBANs)	2360-2400 MHz
802.11b Wi-Fi	2.4 GHz
802. 15. 1 Bluetooth	2.4 GHz
802. 15.4 Zigbee	868, 915 MHz, 2.4 GHz

1.3 Review of Previous Studies

The following subsections review the previous research works for on-body wave propagation on non-moving human (static case) and moving human (dynamic case), and on-body antenna design.

1.3.1 On-body Wave Propagation: Static Case

Over the past decade, extensive studies, involving measurements, simulations and theories, have been conducted to understand wave propagation characteristics on a non-

moving body. In the experiment campaigns, Hall *et al* measured path gains for different channels by placing transmitting and receiving antennas on various body locations such as head, arms and legs [10]. They plotted the mean path gain against the distance of the antenna separation and used linear regression to extract wave attenuation loss, as shown in Fig. 1.2. Later, a number of measurements have been conducted and various statistical methods have been applied to extract channel fading characteristics [11-13]. Similar methods have been deployed for ultra-wideband (UWB) on-body communications [14-16]. The measurement has also been conducted on a skin-equivalent phantom model at 60 GHz [17].

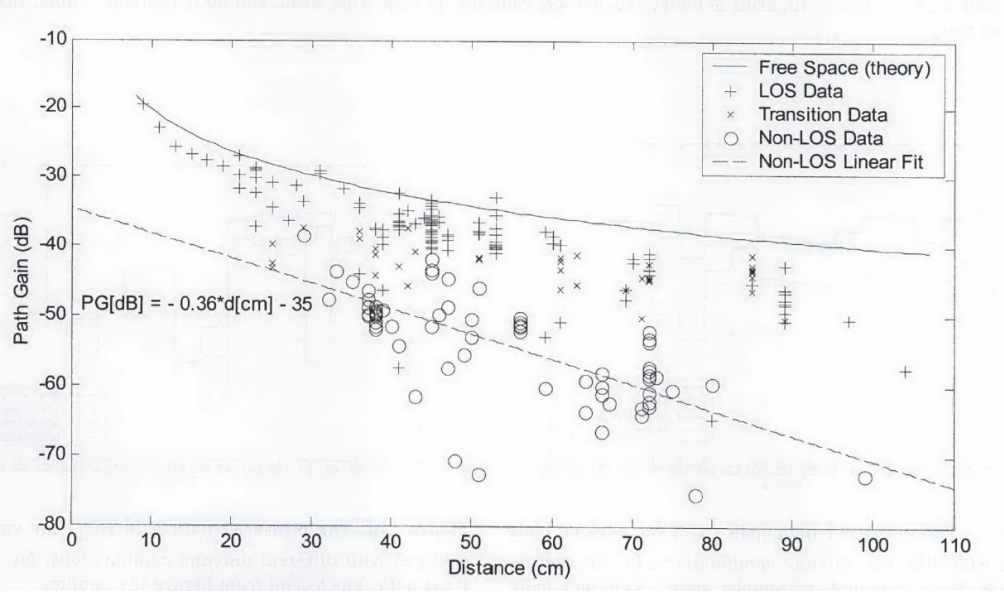

Fig. 1.2. The distance dependence of the mean path gain with the data classified according to the type of path, e.g. line of sight (LOS), non-line-of-sight (non-LOS), and a transition between the two. The frequency was 2.45 GHz [10].

Simulations are introduced to simplify the scenarios as well as validate the experiment results. Various human phantom models have been used in the simulations. For example, anatomically accurate human models, derived from the National Library of

Medicine Visual Human Project [18], were used for the on-body wave simulations [19-20], as shown in Fig. 1.3. In addition, simplified human phantom models were proposed to reduce computational time and complexity [21-23]. For example, Conway [22] derived an elliptical cylinder model and Grimm [23] proposed a human trunk model, filled with either homogenous or inhomogeneous tissue properties.

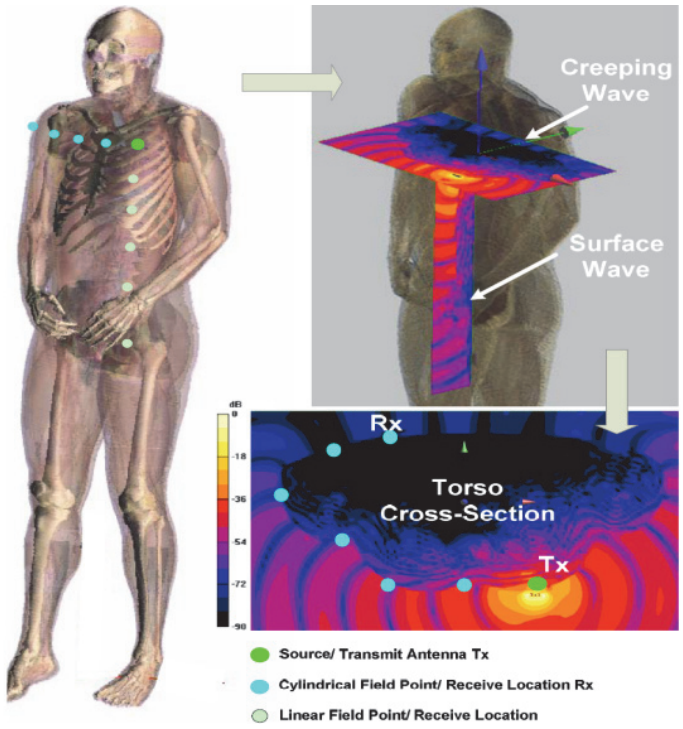

Fig. 1.3. FDTD simulation of whole body adult male numerical phantom illustrating on-body propagation with E-field magnitude slice data along and around the body with field point measurement locations highlighted [20].

For the theoretical analysis, researchers attempted to use either mathematical or classic ground wave solutions to characterize the channel response based on assumptions of body geometries [24-33]. For example, for the propagation around body (non-line-of-sight, NLOS), in Fig. 1.4, Chandra [24-25] derived an elliptical-based link loss model around human torso by using the geometrical theory of diffraction (GTD) [34-35]. Alves

[27] proposed a cylinder-based analytic model based on Wait's creeping wave theories [36-37]. For the propagation along the body surface (line-of-sight, LOS), Lea [31] derived a theoretical model based on Norton surface waves [38-40]. Grim [34] used Bannister's wave solutions [41-42] for different frequencies.

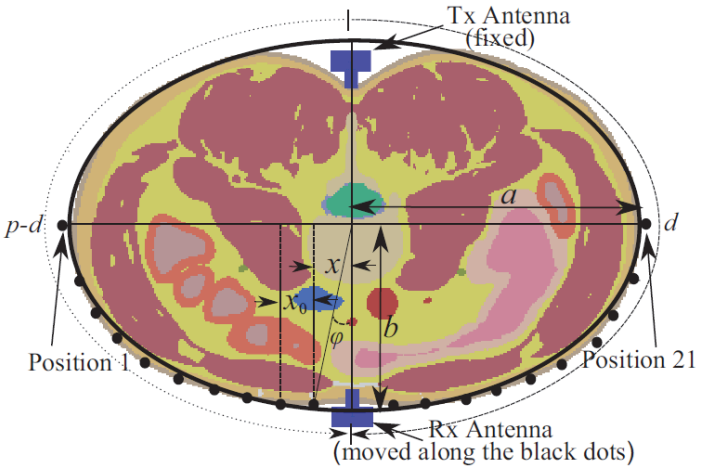

Fig. 1.4. The elliptical approximation of the cross-section human torso at the antenna level [24].

Combined with the above methodologies, different environmental effects are also taken into consideration such as anechoic chamber, office rooms, hallways, outdoors etc. Population varieties are concerned such as ages, genders and body mass index (BMI).

1.3.2 On-body Wave Propagation: Dynamic Case

More recently, there is a growing interest of EM wave propagation study on a moving human body. Experiments of dynamic on-body propagations have been conducted for different activities such as walking and sitting with various antenna configurations. For example, Nechayev investigated dynamic wave propagation on human body at 2.45 GHz [12]. The time-domain channel characteristics were studied via statistical analysis, e.g. the probability distribution of the signal strength, the level-crossing rate (LCR), average fade

duration (AFD) etc. Similar time-variant channel experiments were conducted and an autoregressive (AR) model was proposed for fading estimations [13]. The dynamic channel modeling was also investigated at various frequencies, e.g. relatively low radio-frequency (RF) 45 MHz [43], and for both narrowband [44] and UWB band [45]. In order to validate body experiments results and replicate real-time scenarios for further study, a set of simulation models and techniques were proposed. The simple action can be replicated by using a mechanical phantom model. For example, Yamamoto *et al* developed an arm-swing dynamic phantom model to represent the arm motions for walking and running, as can be seen in Fig. 1.5 [46]. More researchers are in favor of using computer software packages to investigate the various effects of radio links caused by antenna placements, activities, frequencies, etc. For instance, the animation software POSER generates a movie such as a walking cycle and can be imported into EM software XFDTD for a dynamic wave simulation [10, 44, 47], as shown in Fig. 1.6. The researchers also attempted to use the motion capture in conjunction with the EM software to imitate more realistic human walking motions [48] and antenna positions [49]. The simulations and measurements are generally in good agreements.

Another emerging dynamic on-body propagation study is the activity recognition by wireless channel characteristics. Compared to the traditional motion classification methods, which rely on physical sensor such as accelerometer and gyroscope, the EM propagation provides a low-cost, power-efficient way for activity predictions. Recently, Quwaider and Biswas used Radio Signal Strength Indication (RSSI) to detect walking and running with a wearable sensor network [50]. Munoz *et al* applied frequency analysis to identify four different activities and extract physiological signals such as heart rate [51].

Wang and Zhou reviewed various radio based activity recognition such as ZigBee and Wi-Fi [52]. The radio based activity classification methods need to be exploited to identify rich biomechanical information as well as establish a nonintrusive, high-accuracy WBAN system.

Fig. 1.5. The structure of the arm-swing dynamic phantom model [46].

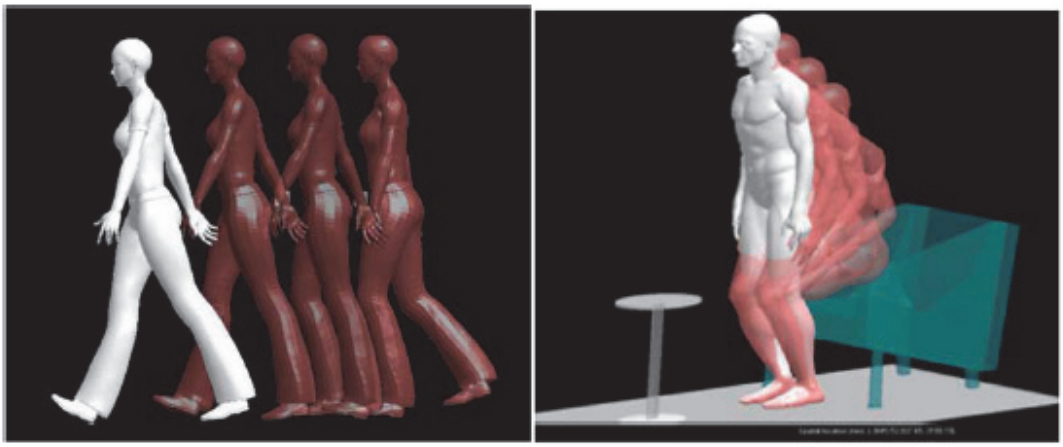

Fig. 1.6. Simulated body movements in POSER software: (a) avatar Jessica walking, (b) avatar James standing up [47].

1.3.3 On-body Antenna Design

A number of researchers have conducted extensive studies for wearable antenna design. The performances of several types of conventional antennas, including monopoles, loops and microstrip patches, have been studied on the human body [10, 20, 33, 53]. It is found that the monopole placed normal to the body surface gives the lowest link loss, as can been seen in Fig. 1.7. This can be attributed to the monopole antenna pattern and polarization: it has omnidirectional patterns with the maximum radiation on the horizontal direction and is vertically polarized with TM wave, which couples into the surface wave propagating along the body surface [10]. To make the antenna more practical and adaptive to the realistic environment, researchers have sought to exploit various solutions. For example, pattern and polarization diversity feature have been deployed on antennas to accommodate different environments and channel links [54-56]. The frequency bands are considered such as dual-band [57], triple-band [58] and UWB bands [59]. The bent and conformal shape of antennas have been invented, e.g. for wristbands in Fig. 1.8 [60]. Textile antennas are proposed so that they can be easily sewed on clothes or backpacks [61-63], as can been seen in Fig. 1.9 (a)-(f). To help increase the gain and efficiency, several antenna arrays have been developed, e.g. fractal geometry with electromagnetic band-gap (EBG) array [64], beam steering parasitic array [65], surface wave array [66] etc.

1.4 Motivations and Objectives

While previous studies have successfully identified on-body propagation mechanisms and their variations during body movements, three important problems remain to be solved for a thorough understanding of on-body wireless communication channels. First, most of previous studies focus on the signal strength attenuation loss of on-body

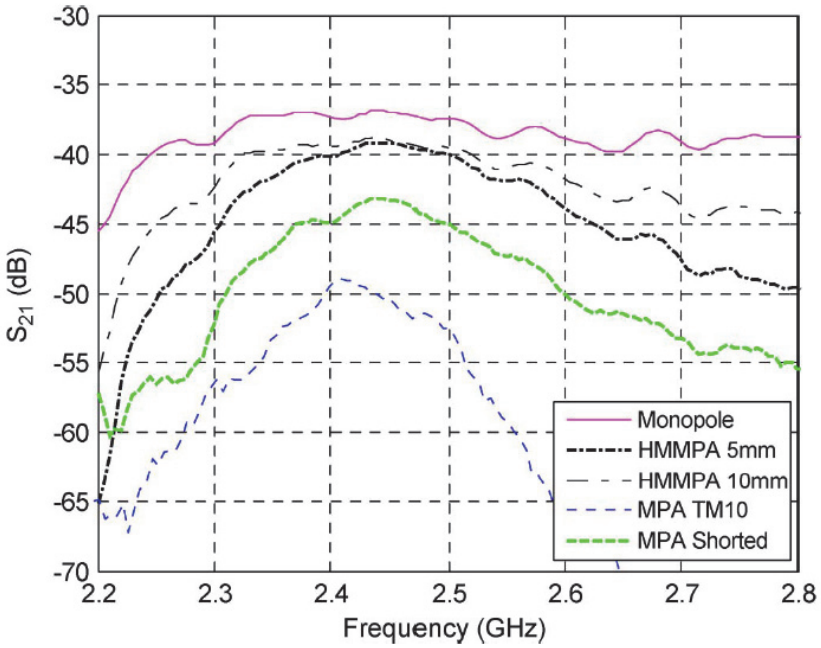

Fig. 1.7. Comparison of measured $|S_{21}|$ path loss for on-body antennas [22].

Fig. 1.8. Radiation-pattern-reconfigurable antenna applied on Fitbit Flex [60].

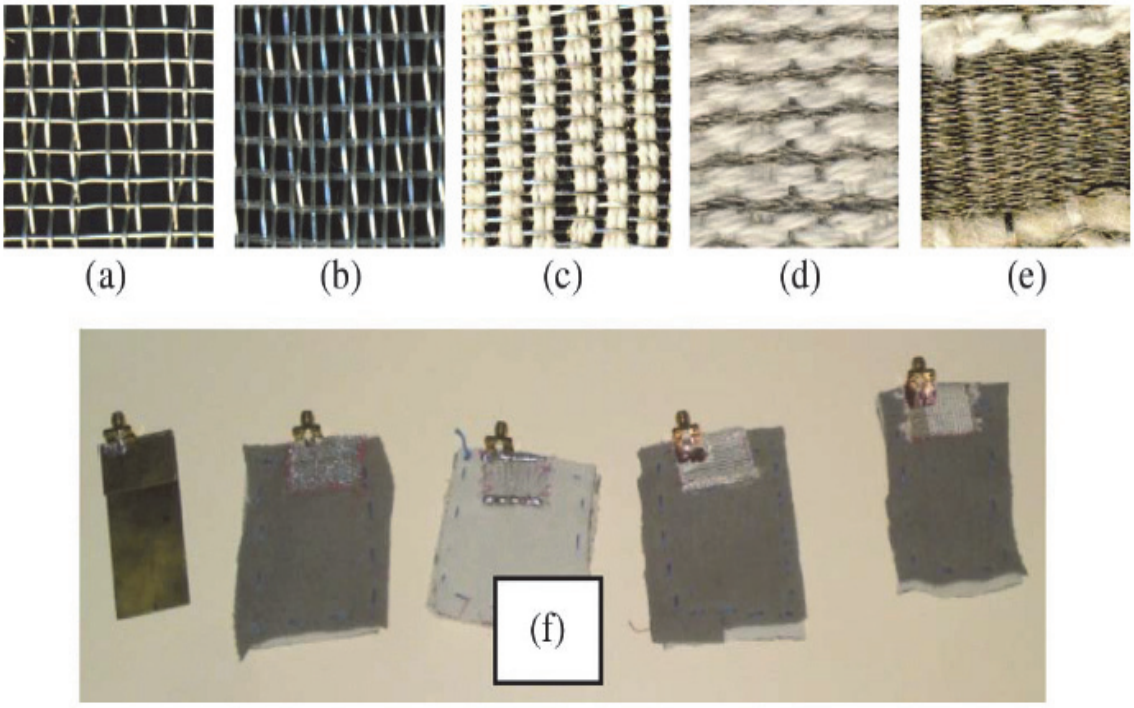

Fig. 1.9. Textile materials and antennas. (a) Metal mesh. (b)Metal polyester. (c) Metal cotton. (d) Conductive yarn cotton—part 1. (e) Conductive yarn cotton—part 2. (f) Manufactured planar inverted-F antenna (PIFA) [61].

waves. However, another important feature of wave propagation, the phase delay, remains to be studied. The phase delay is related to the propagation constant and can reveal how fast a wave propagates. It will provide additional valuable information such as the number of modes and propagation mechanisms. The phase delay is also a vital parameter for the surface wave antenna array design [67-68]. Second, previous studies mainly investigated on-body wave propagation in high frequencies such as 2.45 GHz or UWB. Few have attempted to focus on low frequency ranges. In general high-frequency waves have greater transmission loss and attenuate faster than those of low frequencies, which require more transmitting power level and result in higher energy consumption. In addition, it is desirable to use lower frequencies (<1 GHz) for low data rate applications (e.g. heart beat tracking). The physical size of the antennas at low frequencies may become large and

impractical. The recent development of electrically small antennas can be a potential candidate for the solutions [69]. The wave propagation in low frequency bands are more complicated since the receiving antenna may be located in the near field region of the transmitter. The propagation characteristics and mechanisms remain to be investigated. Last but not least, for the dynamic wave propagation study, the measurements and simulations are based on a pseudo-dynamic scenario, which means the motion is divided into several position snapshots [45, 48]. It is insufficient to study wave propagations in a low sampling rate as the human cannot do robotic movements in daily activities and signals can be varied by transitions of different stages. Besides, the Doppler effects exist in the continuous movements and should not be neglected [70-72]. It is highly desirable to develop a method to continuously, simultaneously record both kinematic parameters as well as EM signals to improve dynamic wave studies, taking both experiments and simulations into account.

While wearable antennas have been extensively studied, several concerns need to be raised for the enhancement of the body antenna performance. First, antennas are mainly designed at high frequencies such as 2.45 GHz. Few have attempted to develop them in relatively low frequency ranges because the antenna physical size can be substantially large, e.g. 7.85 cm length for a quarter wavelength monopole at 915 MHz. Some researchers have attempted to optimize the size for the patch antenna but end up with a poor gain [73]. Second, most studies concentrate on optimizing conventional antenna performance on the human body. Few have utilized the propagation channel to design antennas. By coupling antenna radiation into surface wave propagation, we expect both antenna efficiency and path gain can be boosted. Akhoondazdeh *et al* proposed a parasitic

surface wave antenna array but the path gain is still 10 dB lower than the monopole [66], as can be seen in Fig. 1.10. This is because the proposed antenna array is horizontally polarized and cannot couple with the surface body as strongly as vertically polarized antennas. Therefore, the main problem for the wearable antenna reveals that a better design would be a vertically polarized antenna, but with a small size in a broad range of frequencies.

The objectives of my dissertation study are as follows. First, the broadband, short-range wave propagation will be investigated on a non-moving human from the experiments, simulations and theoretical aspects. Both magnitude decay and phase delay will be studied. The dominant propagation mechanism as well as specific propagation constants will be extracted. Second, the dynamic propagations on both male and female subjects will be explored by the vector network analyzer (VNA) and motion capture, which can simultaneously record EM and kinematic data. The measurement data will be analyzed and simulation models are created. The signal processing technique will be applied for the motion classification. Finally, an electrically-small and directive wearable antenna (array) will be designed for on-body applications.

1.5 Organization of the Dissertation

In Chapter Two, broadband, short-range wave propagation is investigated on a non-moving human body. Two scenarios are considered: wave propagation along the body (line-of-sight, LOS) and around the body (non-line-of-sight, NLOS). In Chapter Three, dynamic wave propagations on both male and female subjects are explored by the experiments and simulations. The signal processing technique is applied to classify motions. In Chapter Four, electrically-small antennas are designed for on-body

applications and human effects on antennas are discussed. Chapter Five illustrate the design of 1-D closely-spaced, multi-element, surface wave antenna array. Chapter Six summarizes findings and discusses future work.

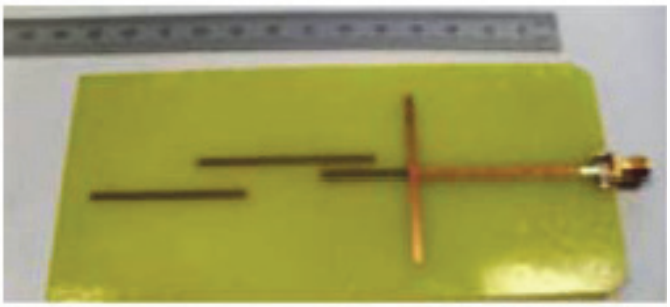

(a)

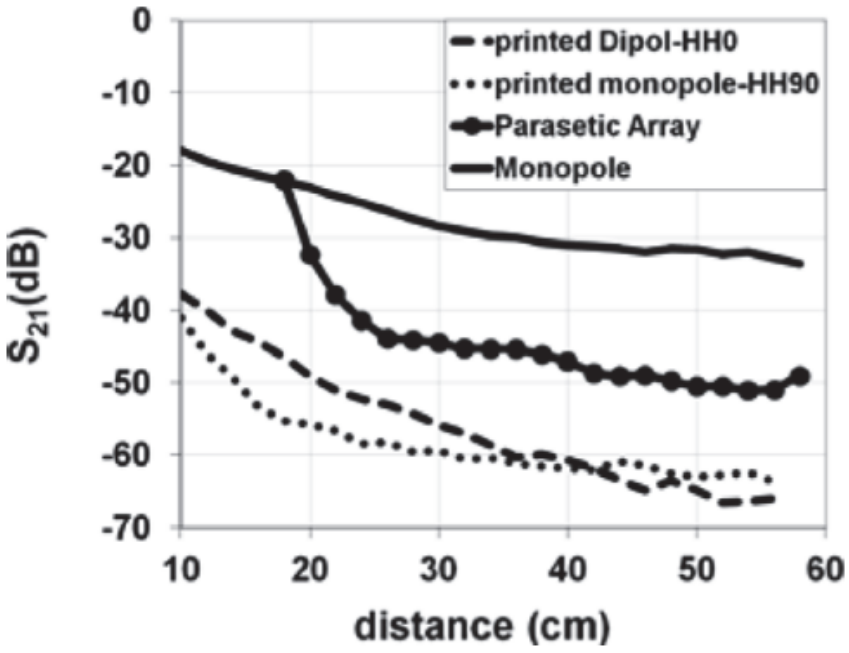

(b)

Fig. 1.10. Fabricated printed surface wave parasitic antenna. (a) Prototype. (b) Measured path gain of different antenna pairs on the muscle-equivalent liquid phantom inside an anechoic chamber [66]

CHAPTER TWO

Electromagnetic Wave Propagations on a Non-Moving Human Subject

In this chapter on-body EM wave propagation for line-of-sight (LOS) transmissions along the body, and for non-line-of-sight (NLOS) transmissions around the body torso are investigated. The study focuses on the frequency band between 300 MHz and 3 GHz, and short transmission distances up to 40 cm for LOS cases, and up to 50 cm for NLOS cases. In each case the dominant propagation mechanisms are extracted from measurements and explained by comparing to simulations and theoretical predictions.

2.1 Electromagnetic Wave Propagation in Open Space

To establish a baseline of the study, wave propagation is first measured and simulated in an open space environment. Fig. 2.1 (a) shows the measurement setup. Both transmitting and receiving (TX/RX) antennas are quarter-wavelength monopoles mounted on a small ground plane of a bridge shape, as shown in Fig. 2.1 (b). The height of the 'bridge' is set at 1.5 cm to accommodate the SMA connector for antenna feeding. Three pairs of TX/RX antennas are made and used to emit frequencies centered at 433 MHz, 915 MHz, and 2.45 GHz, respectively. The sizes of the ground planes for these antennas are 4.0x4.0 cm^2, 4.0x4.0 cm^2, and 2.5x2.5 cm^2, respectively. For each pair, as the receiving antenna is moved away from the transmitting antenna over the large metal plate, complex transmission data (S_{21}) are recorded using a vector network analyzer (Agilent VNA N5230) by 3-meter-long cables (Workhorse Plus 524). The distance between the antennas ranged from 3 cm to 103 cm with a spacing of 3 cm.

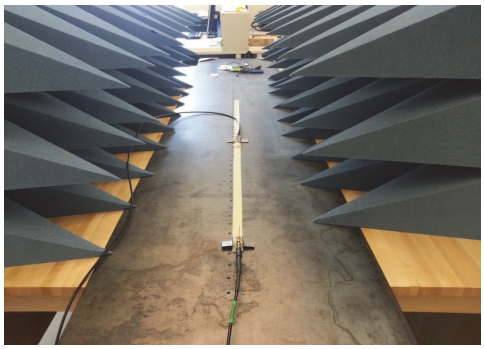

(a)

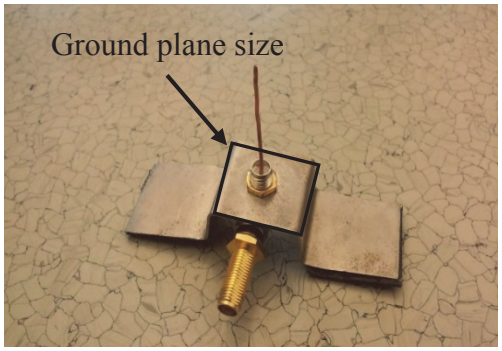

(b)

Fig. 2.1. (a) Open space measurement setup. (b) 'Bridge' monopole antenna.

Both measured magnitude and phase are plotted against frequency and distance in Fig. 2.2 and Fig. 2.3, for antennas operating at 433 MHz, 915 MHz and 2.45 GHz, respectively. In the magnitude plots, the finite resonant frequency bandwidths of the transmitting antennas can be reflected. The receiving signal strength decreases as the distance goes further. The transmission loss becomes higher and signal decays faster for higher frequency antennas. In the phase plots, the phase delay increases fairly linearly against distance, implying there is one dominant propagation mechanism.

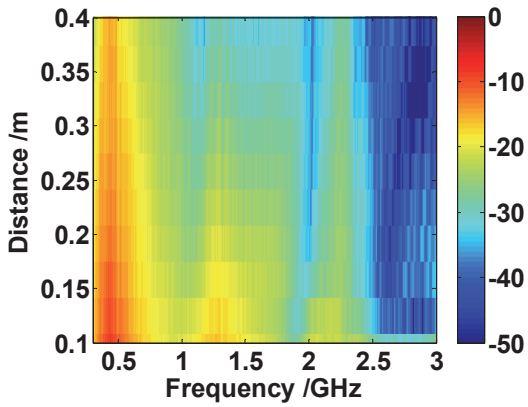

(a)

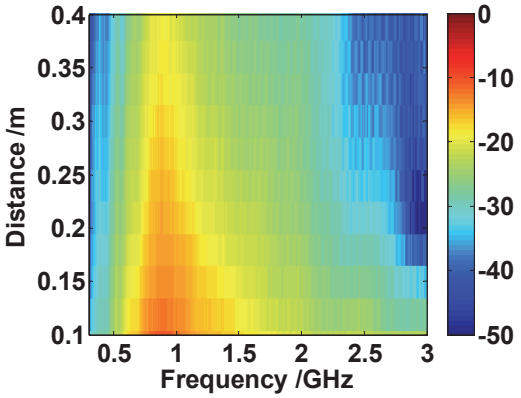

(b)

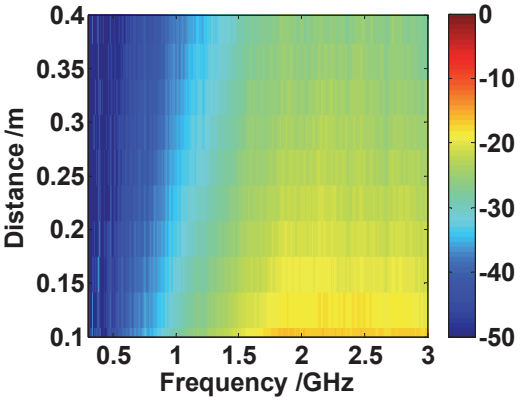

(c)

Fig. 2.2. Normalized transmission loss (in dB scale). (a) Open space for 433 MHz antenna. (b) Open Space for 915 MHz antenna. (c) Open Space for 2.45 GHz antenna.

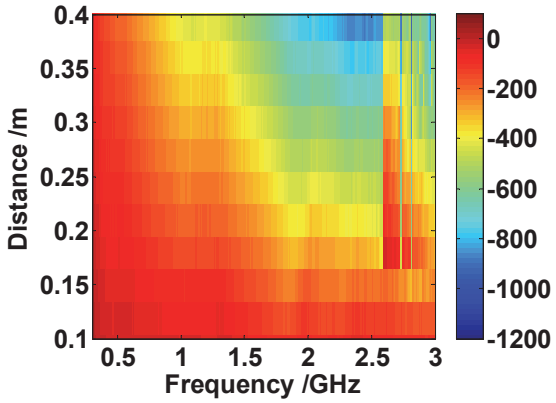

(a)

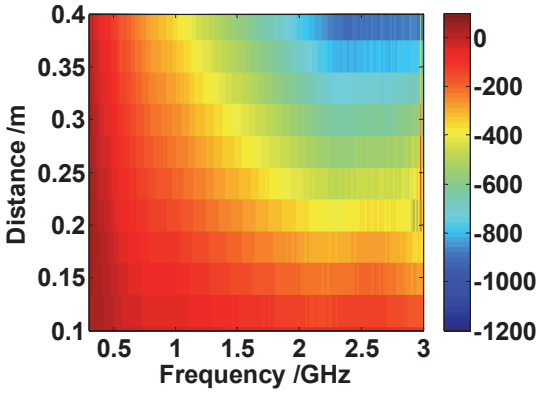

(b)

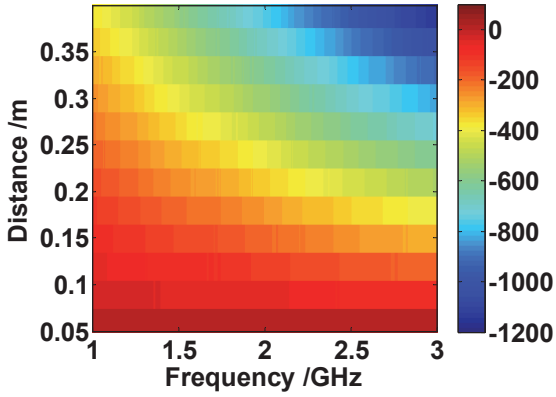

(c)

Fig. 2.3. Phase delays (in degrees). (a) Open space for 433 MHz antenna. (b) Open Space for 915 MHz antenna. (c) Open Space for 2.45 GHz antenna.

In order to validate experimental results, the Numerical Electromagnetic Code (NEC) program is applied to simulate the transmission data. Figure 2.4 (a) and (b) plot the comparison of magnitude and phase of S_{21} at 2.45 GHz. Good agreement is achieved between measurement and simulation results. The wave propagates at the speed of light and experiences $1/r^2$ signal power decays, as expected for the free space case.

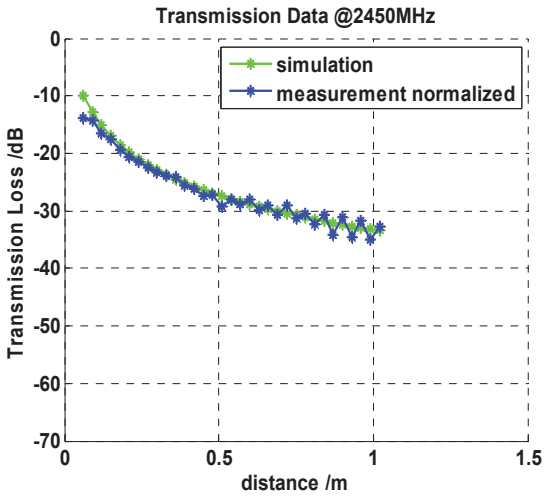

(a)

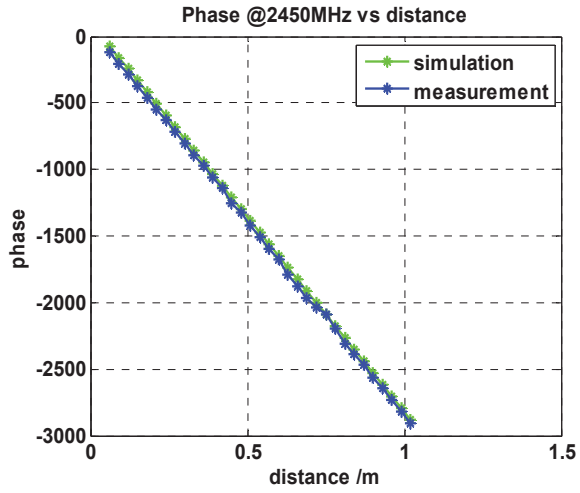

(b)

Fig. 2.4. Comparison of simulation and measurement in open space at 2.45 GHz. (a) Transmission loss. (b) Phase delays.

2.2 Electromagnetic Wave Propagation along the Human Body

In this section electromagnetic wave propagation along the human body (LOS) will be studied through experiments, simulations and theoretical methodologies.

2.2.1 Measurement of Transmission Data

Similar measurements of EM wave transmission data are performed along the body of a male volunteer (age 21 years, height 173 cm, and weight 150 lbs). The experiments are approved by the Baylor University IRB, and the volunteer gave informed consent. The volunteer posed in a fixed, natural, standing position wearing a body suit equipped with a hook-and-loop attachment surface (see Fig. 2.5). A transmitting antenna (TX) with hook-and-loop backing is placed at the front central waist area. A receiving antenna (RX) is placed at various, fixed points along a vertical line up the front, middle torso (see white strip in Fig. 2.5). The fixed points are spaced at 3 cm increments ranging from 3 cm to 40 cm away from TX. Both transmitting and receiving antennas are the same bridge quarter-wavelength monopoles as before and pointed normal to the body surface. The vertical, orientated monopoles are selected since they are widely used for on-body propagation studies [10, 22, 33, and 53] and can strongly excite on-body wave mechanisms. Broadband transmission data are measured at each fixed position of the receiver, and for three pairs of antennas.

The human body effects on the antennas are examined first. It is known that the existence of the human body may affect antenna performance such as by reducing antenna radiation efficiency, detuning antenna resonant frequency, and distorting and depolarizing antenna radiation patterns. Fig. 2.6 shows the comparison between free space and human body of the measured antenna reflection coefficients S_{11} for different antennas. It is seen

that the resonant frequencies of antennas shift only slightly, implying the detuning effects of the human body are negligible in this scenario.

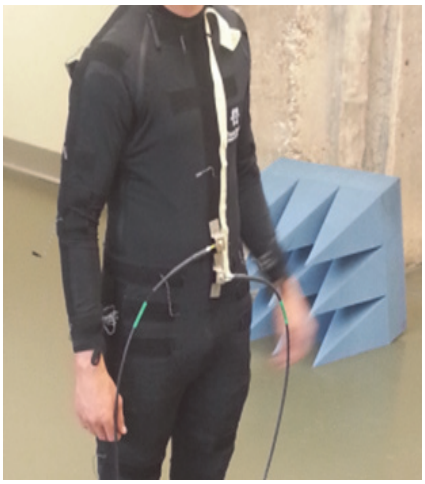

Fig. 2.5. Wave propagation along the human middle chest measurement setup.

Figs. 2.7 and 2.8 show the normalized S_{21} magnitude and phase, respectively, plotted against frequency and the distance between TX and RX along the human middle chest. In Figs. 2.7, the finite resonant frequency bandwidths of the transmitting antennas are reflected in the magnitude plots. The signal strength is weaker and attenuates faster against distance with the higher frequency antennas. The phase plots of Figs. 2.8 show that the phase delay increases fairly linearly against the distance on the human body, indicating there is one dominant propagation mechanism. To better identify the difference between open space and human body transmission, the normalized S_{21} magnitude and phase comparison are plotted against distance between TX and RX at a fixed frequency, e.g. 2.45 GHz, as in Figs. 2.9. It is found that the on-body receiving signal strength is not only weaker, but decays much faster comparing to the free space case. The phase of the transmission data is plotted in Figure 2.9 (b).

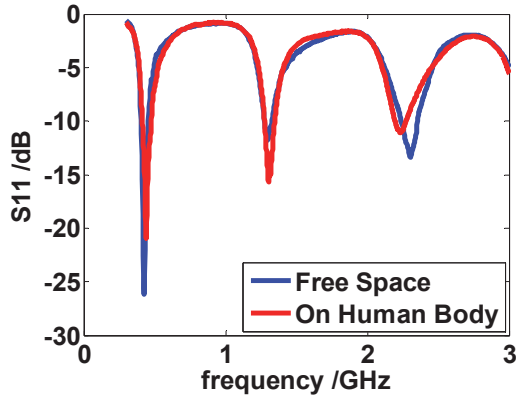

(a)

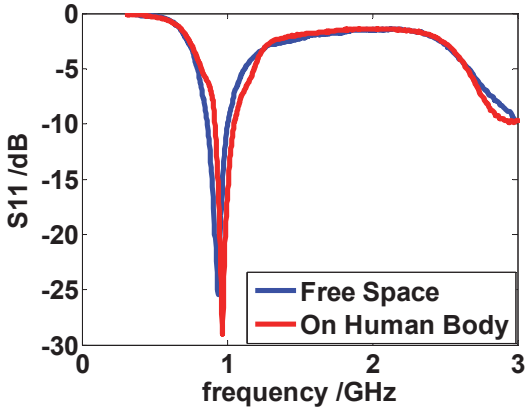

(b)

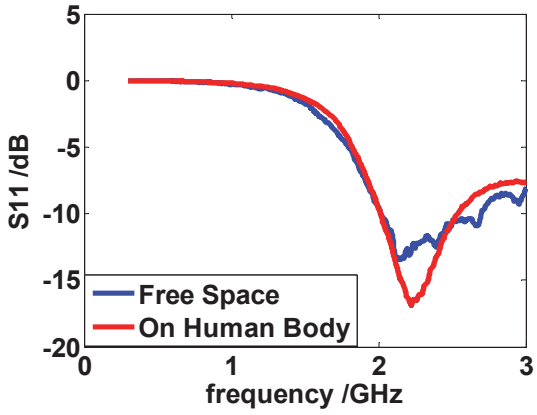

(c)

Fig. 2.6. Reflection Coefficients Comparison between free space and human body. (a) Antenna operating at 433MHz. (b) Antenna operating at 915MHz. (c) Antenna operating at 2.45 GHz.

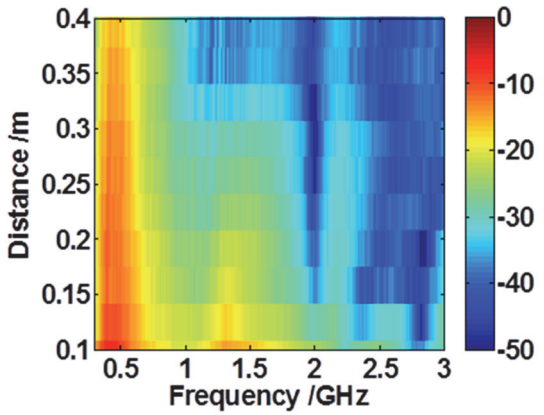

(a)

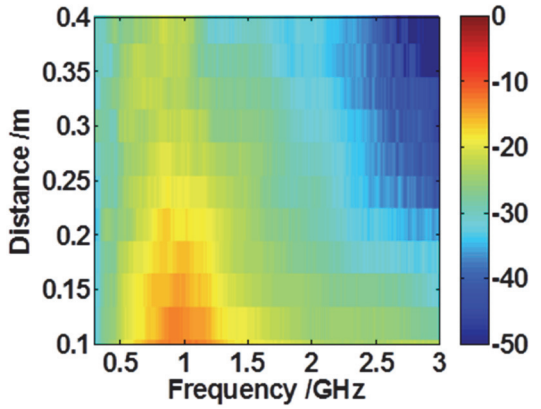

(b)

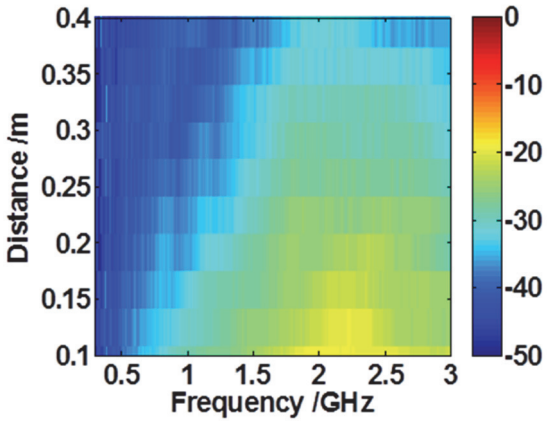

(c)

Fig. 2.7. Normalized transmission loss (in dB scale). (a) Along human middle chest for 433 MHz antenna. (b) Along human middle chest for 915 MHz antenna. (c) Along human middle chest for 2.45 GHz antenna.

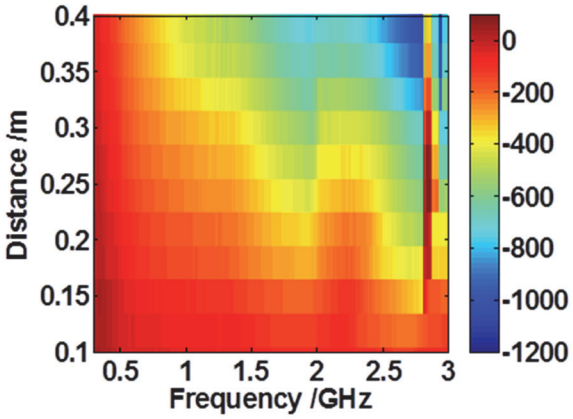

(a)

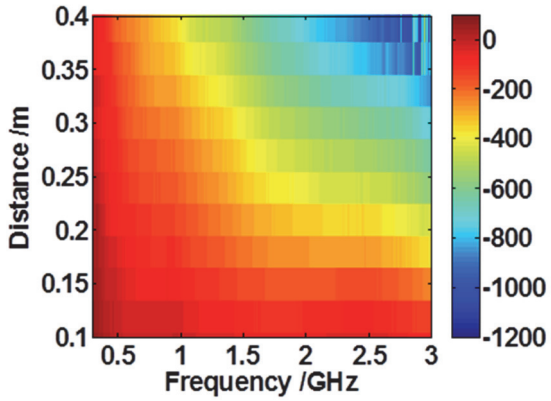

(b)

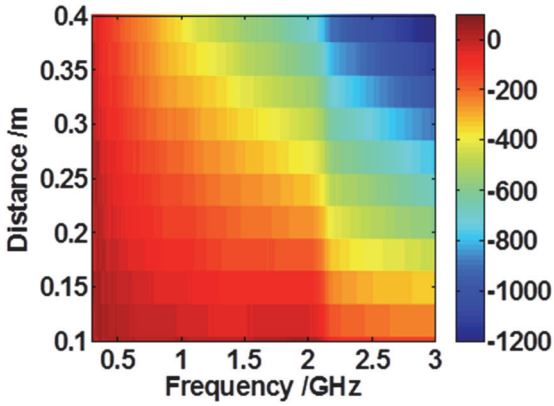

(c)

Fig. 2.8. Phase delays (in degrees). (a) Along human middle chest for 433 MHz antenna. (b) Along human middle chest for 915 MHz antenna. (c) Along human middle chest for 2.45 GHz antenna.

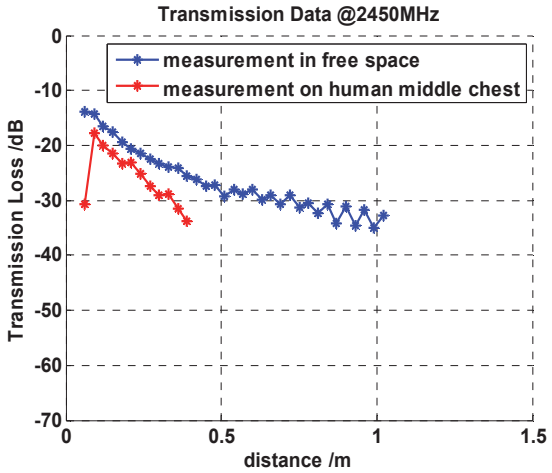

(a)

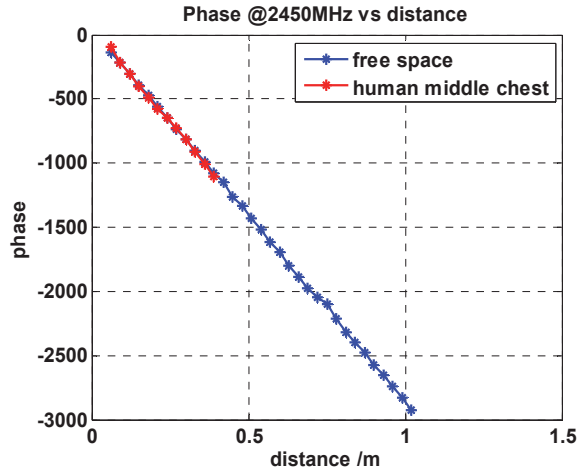

(b)

Fig. 2.9. Normalized transmission loss comparison between open space and human middle chest (LOS) at 2.45 GHz. (a) Magnitude (in dB scale). (b) Phase delays (in degrees).

The slope indicates the speed of the propagating wave. The phase curves are linear in both cases and exhibit the similar slope, implying there is one dominant propagation mechanism along the body and its propagation speed is approximate to that of light in free space. In the next section the specific on-body dominant propagation mechanism will be explored.

2.2.2 Extraction of LOS Dominant Mechanisms Using ESPRIT

The complex transmission data measured at the receiver represents the total of all field components, which may include propagation through the human body, diffraction around the human body, and scattering from nearby objects such as the ground and human arms. Although this data provides a qualitative description on how quickly the field attenuates and propagates, it does not distinguish among the various possible wave mechanisms. By decomposing the total field into different travelling wave modes, we can better investigate each mode's contribution to the propagation channel and identify the dominant wave mechanisms.

To better understand the LOS on-body wave mechanisms, the on-body S_{21} magnitude is normalized to that of open space. This normalization approximately removes the open space magnitude decay in the transmission data. The normalized data is then modelled as a summation of *N* modes, each with its own complex strength c_n and complex propagation constant β_n:

$$\frac{S_{21\_on\,body}}{|S_{21\_open\,space}|} \cong \sum_{n=1}^{N} c_n e^{-j\beta_n d}\,, \tag{1}$$

where d is the distance between TX and RX. The super resolution spectral estimation algorithm ESPRIT [74] is applied to extract β_n and c_n. The extraction results are plotted in Figs. 2.10 for the three pairs of antennas. Only the two strongest modes are shown in the plots since the magnitudes of higher order modes are much weaker and can be safely neglected. In each plot, there is a single prominent line along which the β values increase fairly linearly with increasing frequency. In certain regions (e.g. 2-3 GHz in Fig. 2.10 (a)) the propagation constants cannot be extracted reliably due to the low signal-to-noise ratio.

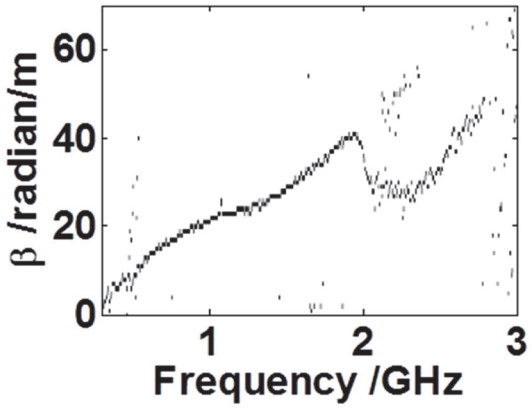

(a)

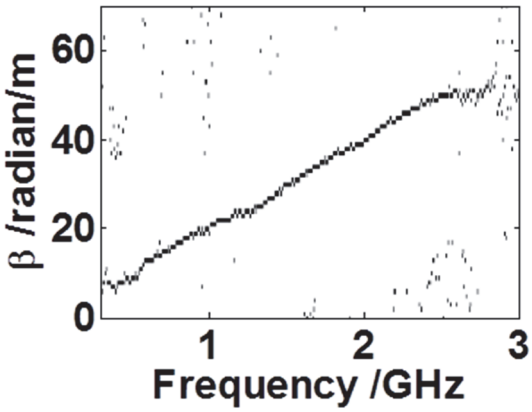

(b)

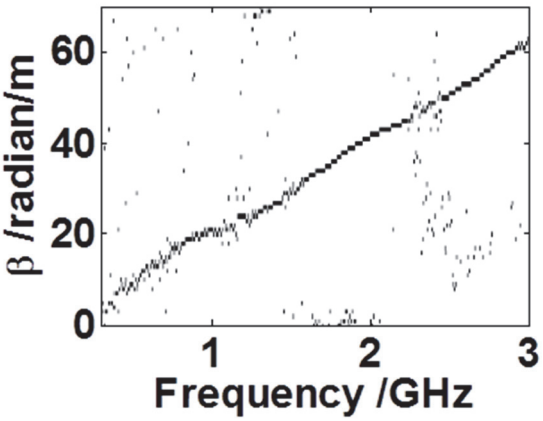

(c)

Fig. 2.10. Extracted propagation constants along human middle chest (a) 433 MHz antenna (b) 915 MHz antenna (c) 2.45 GHz antenna.

2.2.3 Analytical Model Based on Bannister's Ground Wave Theory

Further physical insights about the extracted dominant modes are pursued by employing analytical modelling based on the ground wave theory [38-42]. The human torso is modelled as an infinitely-large plane composed of two layers having homogeneous properties equivalent to muscle and air, respectively. Although a more complicated, multi-layer model (air, skin, fat, and muscle) can also be implemented, the two-layer model has proven sufficient for use below 3 GHz [31]. Also, an anatomically-correct body model can be implemented, but it requires more computational time, and previous studies have not found substantial difference between such models and the simplified, infinitely-large ground model [20, 33]. Based on this simplified model, Norton's solution, which is originally developed for ground wave propagation over the earth's surface, can be applied to derive the receiving field strength [31]. However, Norton's solution works only in the far-field regions. To address this limitation and include the near field effects, Grimm introduced Bannister's solution and verified the results through FDTD simulations for application to arbitrary distances [33]. In the remainder of this section we compare Bannister's solution to our in-situ experimental results, which have been described in section 2.2.1.

Fig. 2.11 shows a diagram of the infinite-plane model. The infinitesimal dipole is located at height h_a above the ground. The receiver is located at height h_b. The upper medium is the free space with $\gamma_0 = j2\pi/\lambda_0$, while the lower medium is the dissipative ground with $\gamma_1 = \sqrt{j\omega\mu\sigma - \omega^2\varepsilon\mu}$. The direct space wave and the reflective wave paths are shown as R_0 and R_1, respectively. Bannister applied the finitely-conducting earth-imaging theory technique to determine the antenna near fields and far fields [41-42]. The

only restriction is that the index refraction $|n|^2 = |\frac{\gamma_0}{\gamma_1}|^2 \gg 10$. In our case, the ground is filled with homogeneous muscle tissue. $|n|^2$ is calculated from Table 2 in [75], and the conditions are satisfied. For the vertical polarized infinitesimal dipole located above ground, the receiving electric field in the z-direction is expressed as follows (for a time factor $e^{j\omega t}$):

$$E_z = E_0 \left[A_{D,z} \frac{e^{-\gamma_0 R_0}}{R_0^3} + A_{R,z} \frac{e^{-\gamma_0 R_1}}{R_1^3} + (1-\Gamma)F(w)cos^2(\varphi_1)\gamma_0^2 \frac{e^{-\gamma_0 R_1}}{R_1} \right] \quad (2)$$

Direct Space Wave Reflect Space Wave Norton Surface Wave

where E_0 is a reference value denoting the excitation value. $A_{D,z}$, $A_{R,z}$ are the summarized expressions of the terms in Bannister's paper [42]. Γ denotes the Fresnel reflection coefficient for vertical polarization. $F(\omega) = 1 - j\sqrt{\pi\omega}e^{-\omega}erfc(j\sqrt{\omega})$ represents the Sommerfeld attenuation function. The numerical distance $\omega \approx -\frac{\gamma_0 R_1}{2}[sin(\varphi_1) + \frac{\gamma_0}{\gamma_1}]$. From (2) it is seen that the *z*-directed *E* fields are separated into components of the direct space wave, the reflect space wave, and the Norton surface wave.

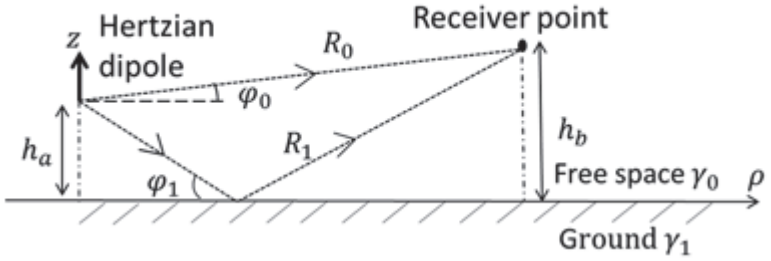

Fig. 2.11. Electrical current above a dissipative planar ground [20].

Table 2. Human muscle tissue properties [75].

Frequency (MHz)	433	915	2450
Relative permittivity ε_1	56.873	54.997	52.729
Conductivity σ (S/m)	0.80484	0.84809	1.7388
Index Refraction $\|n\|^2$	65.9499	57.4620	54.2483

In the model the path gains are calculated with the heights of the transmitter and receiver set to 1.5 cm and 1.7 cm, respectively, to match those of the experiments. Figs. 2.12 compare the transmission loss between the measurements and the Bannister model at discrete frequencies of 433 MHz, 915 MHz, and 2.45 GHz, respectively. It can be seen that the analytical model shows reasonable agreement with the measurement, particularly at higher frequencies. To identify the dominant wave mechanisms, the total electrical fields are decomposed into space and surface wave components (see Figs. 2.13). At all three frequencies the space wave is dominant when the distance is small, but it decays much faster than the surface wave. The reason is that the heights of our source and observation points are relatively small compared to the long distance range. At longer distances the reflection coefficient becomes negative, and the reflected wave cancels the direct space wave, leaving only the Norton surface wave component. It can also be observed that the intersection point of the space wave and surface wave shifts left as the antenna frequency increases. These results indicate that the space wave is the dominant wave mechanism for the LOS case in our measurements when the range is small over the body surface (below 0.4 m).

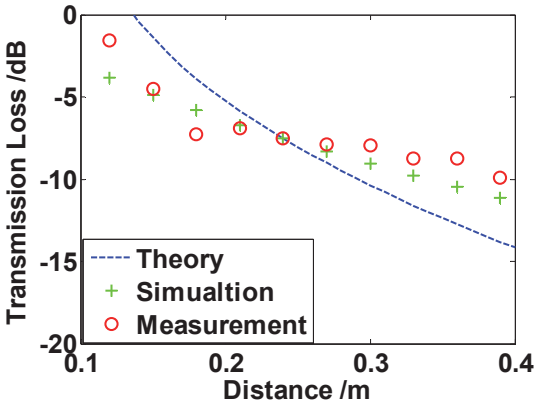

(a)

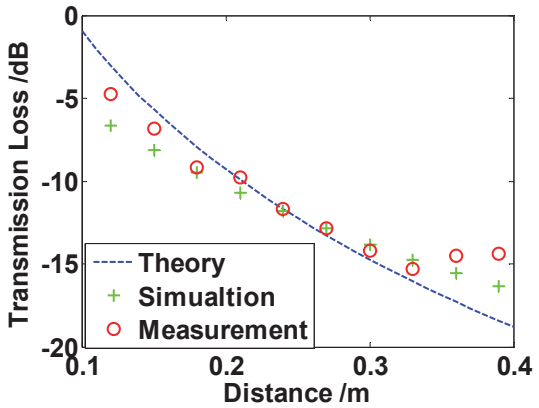

(b)

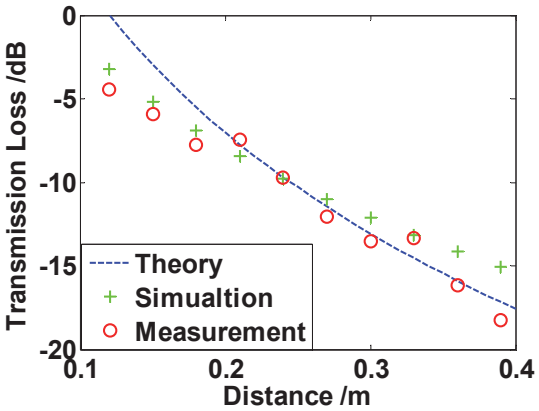

(c)

Fig. 2.12. LOS transmission loss comparison at a single frequency (The simulation and Bannister's model are normalized at distance 0.24 m to the experimental data (a) 433 MHz (b) 915 MHz (c) 2.45 GHz.

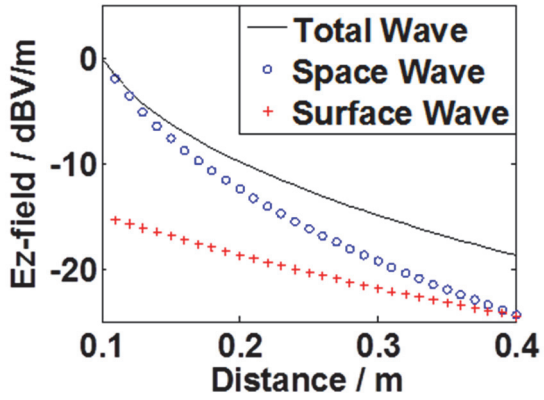

(a)

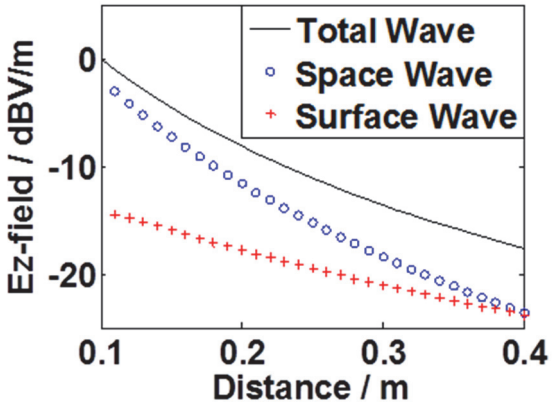

(b)

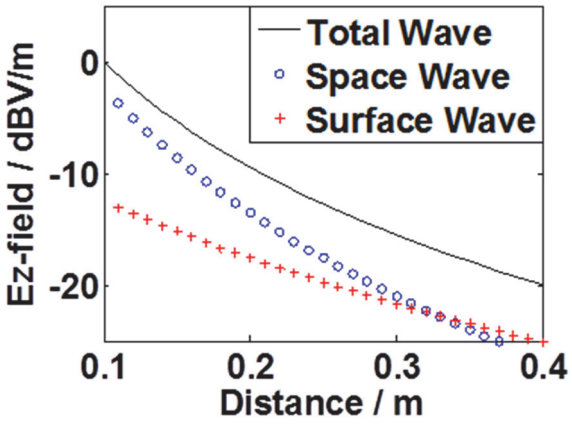

(c)

Fig. 2.13. Normalized electric fields (in z direction) of decomposed wave components (a) 433 MHz (b) 915 MHz (c) 2.45 GHz.

2.2.4 Full Wave Simulations for LOS On-body Propagation

In order to validate the analytical model and measurement data, MOM-based FEKO full-wave simulations are performed on a simplified human torso model. In Fig. 2.14 (a), a monopole antenna (corresponding to the measurement setup) is placed 1.5 cm above an infinite homogenous ground filled with muscle property. The upper space is free space. The near electric field is collected 1.7 cm above the ground at every 3 cm along the surface. The simulation results are added to Figs. 2.12. It can be found that the simulation data agree well with the measurement and analytical model results for different antennas and frequencies.

To justify use of an infinitely-large plane as a model for the human body at lower frequencies (e.g., at 433 MHz the wavelength is larger than 70 cm), a test MOM-based FEKO simulation is performed using an elliptical cylinder model sized to match the torso of our human subject (in Fig. 2.14 (b)). It shows very similar results to that using the infinite ground plane, as shown in Fig. 2.15, justifying our use of the infinitely-large muscle ground at 433 MHz.

2.3 Electromagnetic Wave propagation around the human body

In this section electromagnetic wave propagation around the human body (NLOS) will be studied through experiments, simulations and theoretical methodologies.

2.3.1 Measurement of Transmission Data

Having completed the LOS on-body propagation study, a similar methodology is applied to study NLOS wave propagation around the human body.

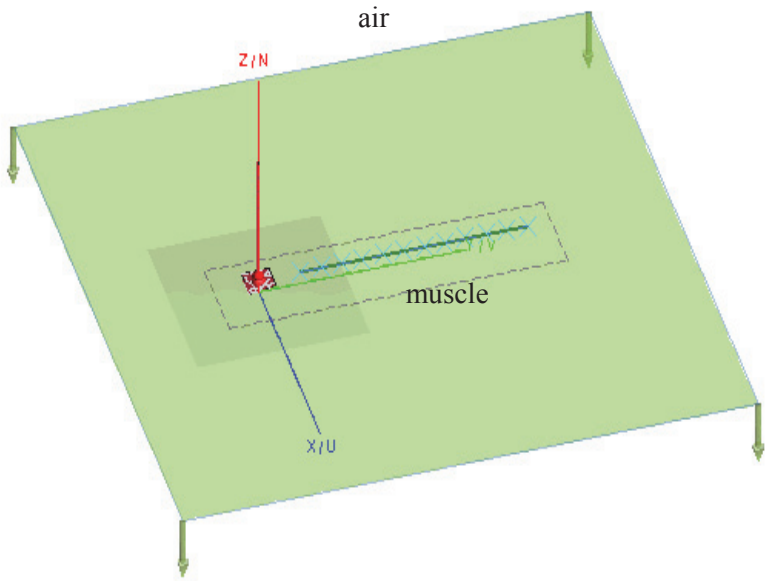

(a)

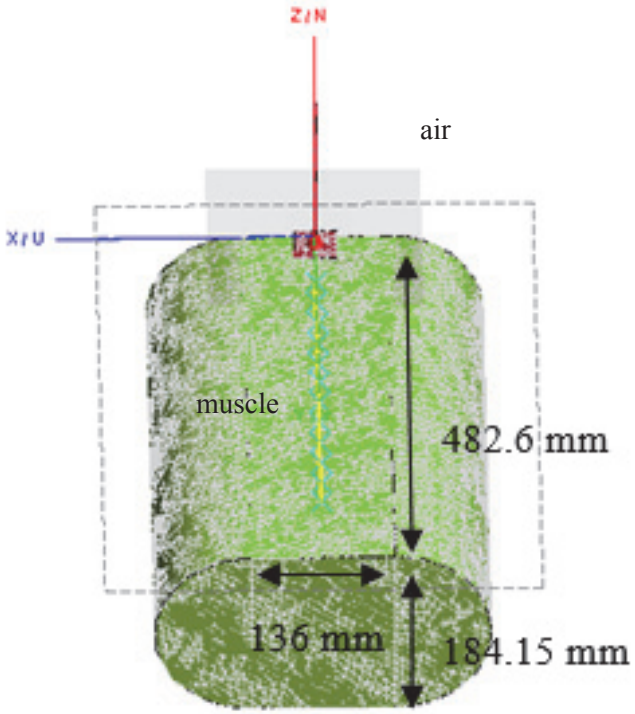

(b)

Fig. 2.14. Simulation Setup in FEKO (a) Infinitely large ground filled with homogenous muscle tissue (b) Elliptical cylinder filled with homogenous muscle tissue.

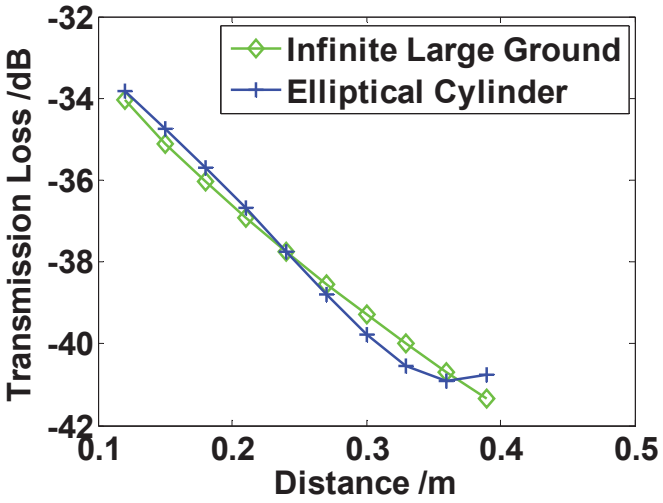

Fig. 2.15. Transmission Loss Comparison between infinitely large ground plane model and elliptical cylinder model.

To begin, broadband transmission data are measured in a new set of experiments using the same three sets of 'bridge' monopole antennas, and the same male volunteer. The experimental setup is shown in Figs. 2.16 (a) and (b). The volunteer posed in a fixed standing position with both arms raised to the side to avoid interference with wave propagation paths. TX is placed at the front center of the subject's chest, and RX is placed at fixed points in the transverse (horizontal) plane every 3 cm around the torso. At each point, and for each pair of antennas, the broadband transmission data are measured as before.

Figs. 2.17 show the transmission data for antennas resonating at 433 MHz, 915 MHz, and 2.45 GHz, respectively. These plots show that, for a given frequency, the signal decays quickly as the receiver moves away from the transmitter, then steadies to a fairly constant level as the receiver crosses the back center of the torso, and finally increases again to the initial level as the receiver returns around to the front center chest. It can also be observed that the attenuation rate of the signal increases with increasing frequency.

(a)

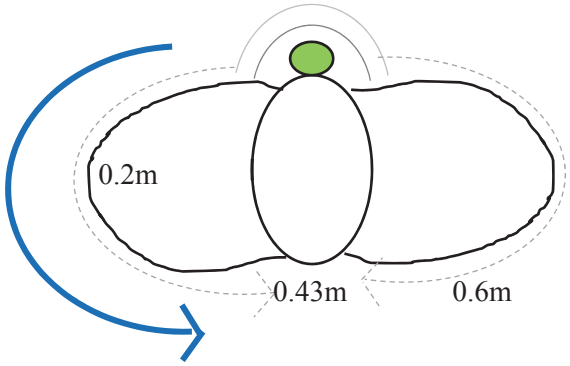

(b)

Fig. 2.16. Wave propagation around human middle chest (a) Measurement setup (b) Geometry of the human torso.

Figs. 2.18 show the corresponding unwrapped phase data against distance around the torso across a wide frequency band. The abrupt changes in the phase plots (e.g., 1.3 GHz for 433 MHz antenna) correspond to the antenna resonant frequencies, as shown in the magnitude plot. Overall the phase data is fairly linear against distance and exhibit symmetric patterns, implying two waves travelling at similar speed around the human body but in opposite directions (clockwise and counter-clockwise). The phase delay becomes larger as the frequency increases.

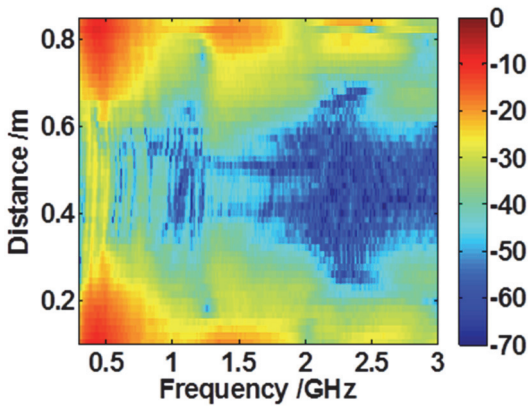

(a)

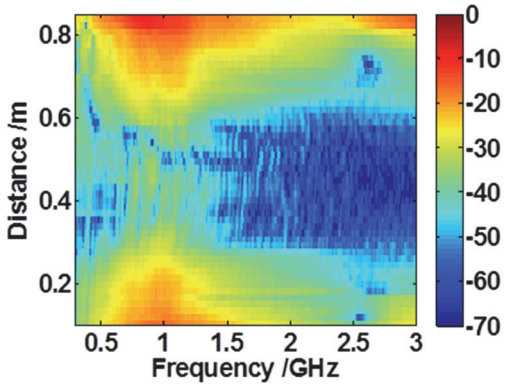

(b)

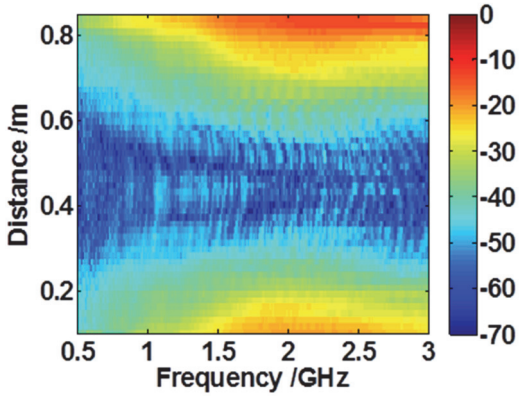

(c)

Fig. 2.17. Around human middle chest (a) Normalized transmission loss (in dB scale) for antenna operating at 433 MHz (b) Normalized transmission loss (in dB scale) for antenna operating at 915 MHz (c) Normalized transmission loss (in dB scale) for antenna operating at 2.45 GHz.

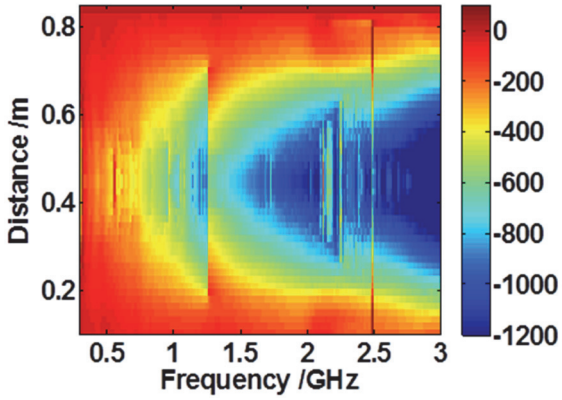

(a)

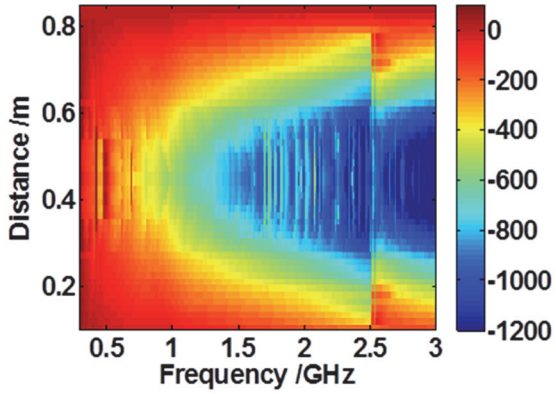

(b)

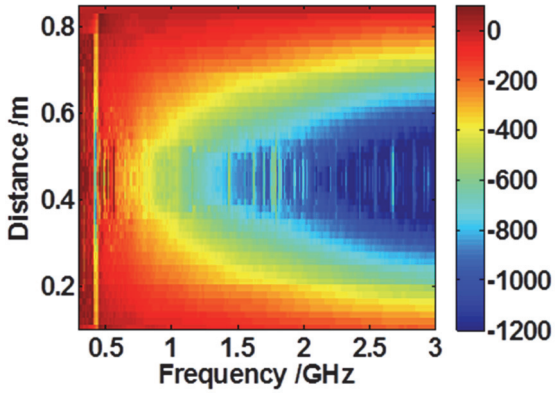

(c)

Fig. 2.18. Around human middle chest (a) Phase delays for antenna operating at 433 MHz (b) Phase delays for antenna operating at 915 MHz (c) Phase delays for antenna operating at 2.45 GHz.

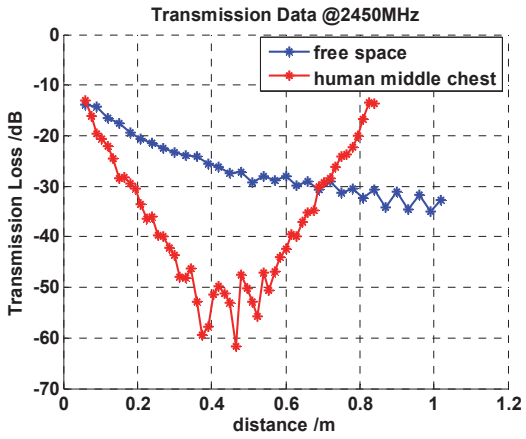

(a)

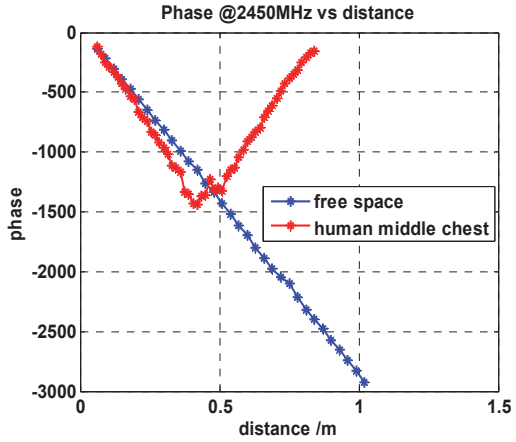

(b)

Fig. 2.19. Normalized transmission loss comparison between open space and human body middle chest (NLOS) at 2.45 GHz (a) Magnitude (in dB scale) (b) Phase delays (in degrees).

We also compare the on-body propagation with that of the free space. As shown in Figs. 2.19, we can see the magnitude of receiving signal strength attenuates much faster for on-body case. In fact, it is an exponential decay. The symmetrical pattern across the distance implies wave propagating in two opposite directions. The slope of the on-body phase curve is slightly larger than that of the free space, indicating a slower wave propagation speed. Next the specific propagation constants will be extracted.

2.3.2 Extraction of NLOS Dominant Mechanism Using ESPRIT

As with the LOS case, the ESPRIT algorithm is applied to extract the dominant mechanism for the NLOS case. Fig. 2.20 shows that two dominant wave modes are extracted at 2.5 GHz. The color indicates the strength of the wave mode against distance on a decibel scale. The normalized propagation constants of the waves are $\pm 1.23 k_0$, where k_0 is the free space wave number, indicating two slow waves travelling in opposite directions. The attenuation constants of the waves are similar to each other (α_+=14.9, α_-= -14.7 Np/m), implying the slow waves experience large exponential decay while propagating around the human body. The strengths of other wave modes are much weaker and can be safely neglected. Summing the two dominant wave modes can nearly reconstruct the original transmission data.

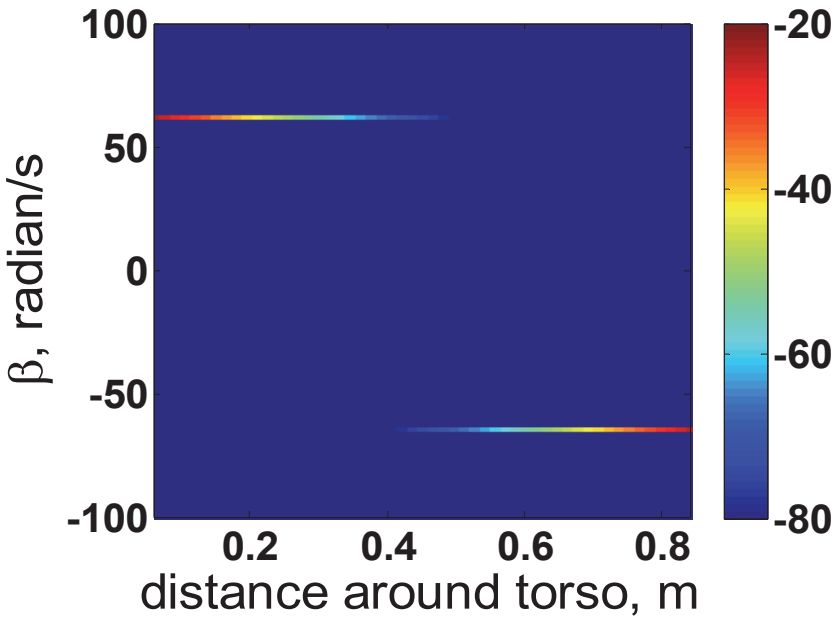

Fig. 2.20. Extracted dominant propagation modes at 2.5 GHz (NLOS).

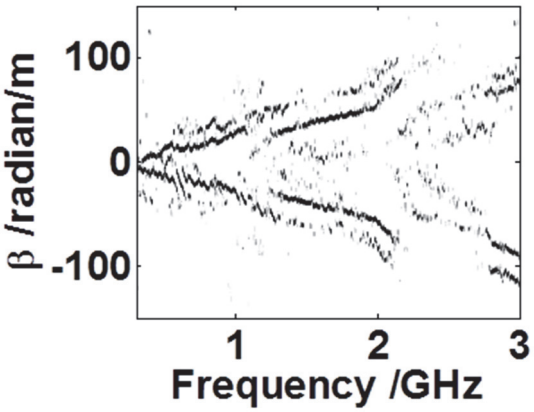

(a)

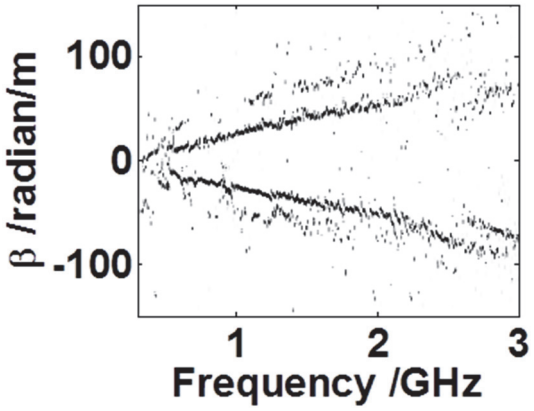

(b)

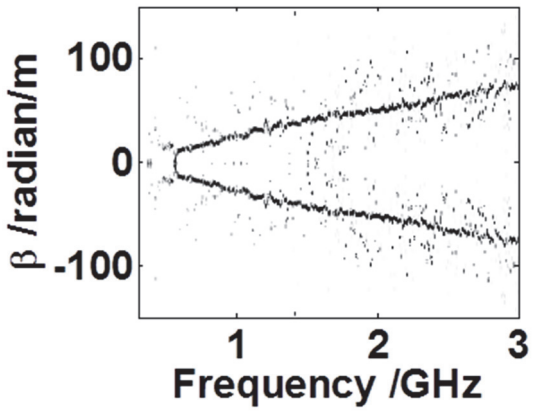

(c)

Fig. 2.21. Extracted propagation constants for antenna operating at (a) 433 MHz (b) 915 MHz (c) 2.45 GHz.

For multiple frequencies, the extracted β values of the four most significant modes are plotted versus frequency in Figs. 2.21. Two distinct tracks with similar propagation constants but opposite directions can be observed for the 915 MHz and 2.45 GHz antennas, indicating two dominant wave propagation mechanisms. For the 433 MHz antennas, more tracks appear in the plot in addition to the two dominant ones, which can be attributed to multiple-path effects (e.g. reflections from the walls, ground, and other parts of the body) since signals experience less attenuation at lower frequencies.

2.3.3 Analytical Model Based on Wait's Creeping Wave Theory

The most popular theory explaining around-body propagation is the creeping wave theory, which was originally developed by Wait for radio wave propagation around the earth [36]. Ryckaert *et al.* first identified creeping waves for propagation around the human body [19]. Conway derived the analytical model based on Wait's theory using a summation of various modes [20]. Later, Alves proposed a more concise model but under the assumption of short wavelengths, which worked for high frequency antennas [27]. In this paper a simplified model is derived based on Wait's theory and applied for broadband transmission. For this model the torso is considered as a homogenous cylinder filled with the properties of muscle tissue, as in [20].

The model is illustrated in Fig. 2.22. For the vertical electric dipole source of moment *Idl* normal to the surface, the radial electric field intensity $|E_r|$ is expressed as [37]:

$$|E_r| = E_0 F(x, q) \tag{3}$$

Where E_0 and $F(x,q)$ are the reference fields and the propagation factor, respectively. Details of these expressions can be found in [37]. By calculating various creeping wave modes and comparing with the measurement data, we find that there is one dominant mode t_1 and other modes can be neglected. Therefore the formula can be simplified as follows:

$$|E_r| = -\frac{j\mu_0\omega I dl}{2\pi d} e^{-\gamma_0 d} \sqrt{\frac{\pi A(d/R)}{j}} \frac{w(t_1-y_a)w(t_1-y_b)e^{-jA(d/R)t_1}}{w^2(t_1)(t_1-q^2)} \quad \text{'Clockwise'}$$

$$-\frac{j\mu_0\omega I dl}{2\pi d_c} e^{-\gamma_0 d_c} \sqrt{\frac{\pi A(d_c/R)}{j}} \frac{w(t_1-y_a)w(t_1-y_b)e^{-jA(d_c/R)t_1}}{w^2(t_1)(t_1-q^2)} \quad \text{'Counter Clockwise'} \quad (4)$$

Where

$$A = \sqrt[3]{(-j\gamma_0 R)/2} \quad (5)$$

$$y_a = -\frac{j\gamma_0 h_a}{A}, \quad y_b = -\frac{j\gamma_0 h_b}{A} \quad (6)$$

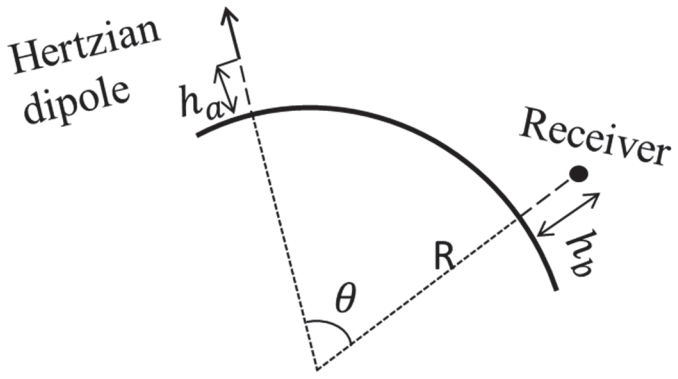

Fig. 2.22. Vertical electrical dipole above a curve surface.

The arc distance between the source and receiver are $d = R\theta$ (clockwise) and $d_c = R(2\pi - \theta)$ (counter clockwise), respectively. To be consistent with LOS, γ_0 is used here

to represent the propagation constant of air. $w(t)$ denotes the Airy integral function, where q and t_1 can be found in [36-37]. Using (4) (5) (6), the normal component of the electric field around the torso *(*$0 < \theta < 2\pi$*)* can be calculated. The comparison between analytical model and experimental data are plotted in Figs. 2.23. It is found that the analytical model achieves good agreement with the experimental data for all three antenna frequencies, confirming that the creeping wave is the dominant propagation mechanism in the around torso propagation scenario.

2.3.4 Full Wave Simulations for NLOS On-body Propagations

Full wave simulation in FEKO is performed for NLOS propagation. In Fig. 2.24, the torso is modelled to be a finite height cylinder filled with homogeneous muscle tissue. The height and perimeter of the cylinder are set to 48.26 cm and 85.09 cm, respectively, corresponding to the height and perimeter of the test human subject. The monopole antenna is placed in front of the middle level of the chest. Near-electric fields are collected via probes placed every 1.5 cm at the same cross section level. The simulation results are added to Figs. 2.23. It can be found that the simulation data agree well with the measurement and analytical model results for different antennas and frequencies, confirming that the torso assumption model and measurement campaigns are valid.

2.4 Summary

This section presents a comprehensive study of short-range, broadband wave propagation along and around a non-moving human body. Experiments are conducted on a non-moving human male and in open space. The ESPRIT method is applied to extract propagation characteristics from the experimental data. Analytical models based on ground

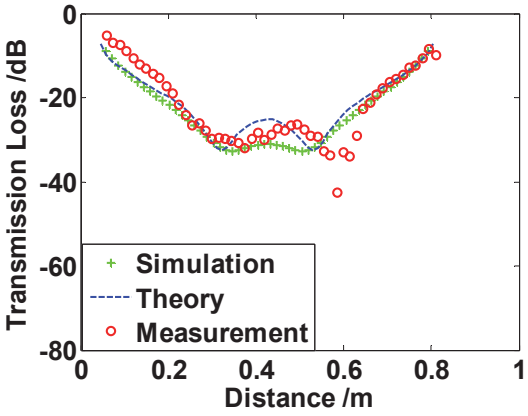

(a)

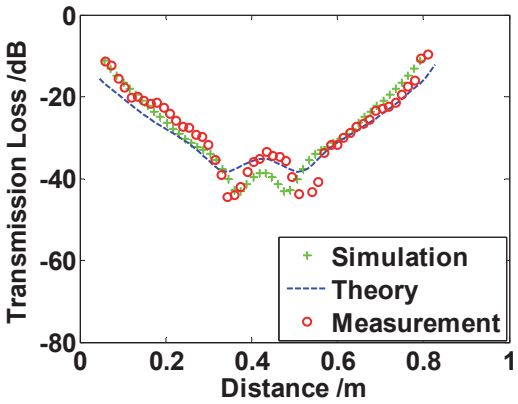

(b)

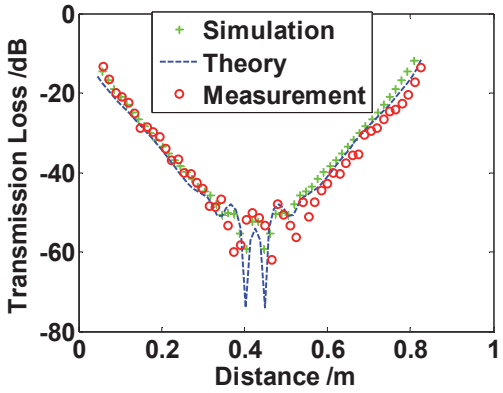

(c)

Fig. 2.23. NLOS transmission loss comparison at a single frequency (The simulation and Wait's model are normalized at distance 0.24m to the experimental data) (a) 433 MHz (b) 915 MHz (c) 2.45 GHz.

and creeping wave theories are derived, taking account of both near fields and far field effects.Full wave simulations are implemented to corroborate with measurement data and theoretical model. It is shown that the space wave is dominant for the LOS case, and the creeping wave (with two modes in opposite directions) is dominant for the NLOS case within short ranges on the human body.

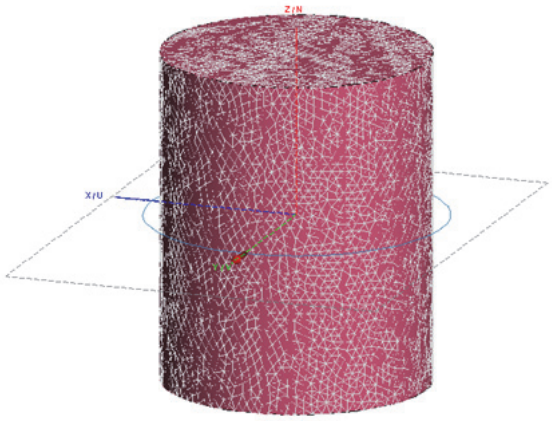

Fig. 2.24. Simulation setup in FEKO (NLOS) – Finite height cylinder model.

CHAPTER THREE

Electromagnetic Wave Propagations on a Moving Human Body and Application for Motion Classification

In the last chapter EM wave propagations on a non-moving human body are studied and dominant propagation mechanisms are identified. In this chapter EM wave propagations on a moving human body are investigated. The measurement campaigns involving VNA and motion capture techniques are demonstrated. A simulation platform for modeling and analyzing dynamic on-body wave propagations is proposed. The comparisons between measurements and simulations are discussed. The characteristics of dominant on-body waves are utilized to classify human motion activities.

3.1 Measurement and Simulation of On-Body Dynamic Wave Propagations

In this section measurement and simulation modeling of wave propagations on moving human body are studied.

3.1.1 Measurement Setup

In the measurement, the motion capture and VNA are applied to record real-time motion data and EM signals simultaneously. Motions are recorded using an eight-camera Phasespace Improv, active-LED Motion Capture system at 120 frames per second (Phasespace, Inc., San Leandro, CA). An adult male volunteer stands in an indoor, open environment wearing a 38-marker, snugly-fitting body suit, as shown in Fig. 3.1. The markers are placed at various points along the torso, head, arms, and legs to capture motions for different body segments. S_{21} complex transmission data are collected using a 2-port

VNA (Agilent N5230C). Quarter-wavelength monopoles are used as the transmitting and receiving antennas, which is the same as of static case. The transmitting and receiving antennas are connected to the VNA using 3-meter long cables. A mechanical switch is used to trigger and synchronized motion capture and VNA. The experiments are approved by the Baylor IRB.

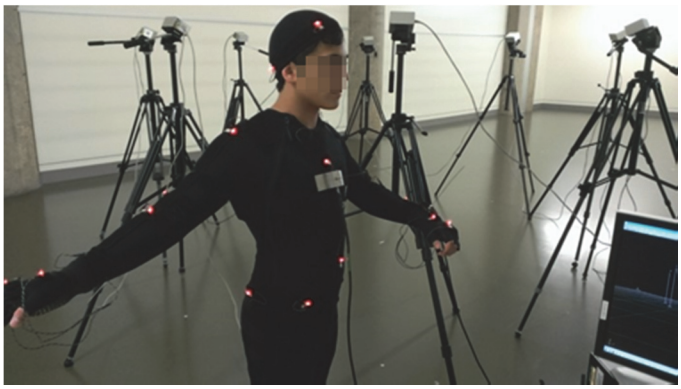

Fig. 3.1. Motion Capture and VNA experiment setup with antennas on the chest and wrist at 433 MHz.

The dynamic wave propagations are measured under two different antenna configurations. In the first configuration the transmitting antenna is placed above the volunteer's left wrist and the receiving antenna is placed on the volunteer's middle chest (see Fig. 3.1). Both antennas are strapped to the volunteer over the body suit. In the second configuration the transmitting antenna is placed on the volunteer's chest and the receiving antenna is placed on the volunteer's back. Three pairs of antennas are used for different trials to cover WBAN frequency bands centered at 433MHz, 915MHz, and 2.45GHz. As the human subjects are performing various activities, complex transmission data S_{21} are recorded using the VNA under continuous time mode with a sampling rate of 120 Hz. The experiments involve six different activities: boxing, hopping, left arm swinging, rowing,

sitting, and both arms swinging, as illustrated in Fig. 3.2. The participants performed each activity continuously for 40 seconds, and for each of three repeated trials. The motion speed is 60 bpm, controlled by a metronome.

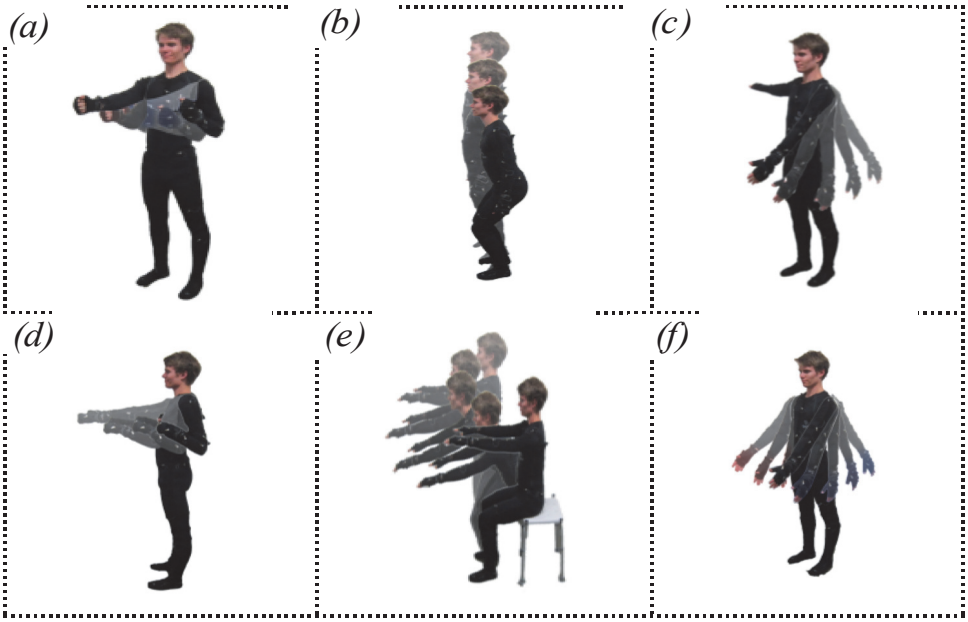

Fig. 3.2. Six human activities: (a) boxing, (b) hopping, (c) left arm swing, (d) rowing, (e) sitting, and (f) both arms swing.

3.1.2 Simulation Modeling Method

Experimental studies of EM propagation around the human body are helpful, but tend to be limited to measurements only at the points of transmission and reception. Computer simulation modeling methods may provide additional insights as a whole cloud of EM probes can be simulated to reveal EM propagation paths around the body between transmitter and receiver. The simulation platform for modeling and analyzing dynamic on-body electromagnetic wave propagations combines motion capture technique, simplified human phantom model construction, and full wave electromagnetic simulations. Based on the motion capture experiments described above, a simulation model is developed in

Recap2 (Phasespace, Inc., San Leandro, CA) to recreate the motion tasks for each of the experimental configurations. A human skeleton model replicates the limb segments and joint degrees of freedom obtained from the motion capture system, as shown in Fig. 3.3. These data are then exported from Recap2 in BioVision (bvh) file format, and reflected a model skeletal hierarchy as shown in Fig. 3.4. The human body model is recreated in CST EM simulation software (Computer Simulation Technology, Inc., Framingham, MA). The model uses simple geometric cylinders to represent each of ten body segments including the head, torso, both upper arms, both forearms, both thighs, and both lower legs (see Fig. 3.5). The model segment dimensions are set to match those of the human volunteer. A CST macro using Visual Basic for Applications is developed position the CST body model according to the .bvh file for each frame recorded in the experiments. The ten cylinder CST model is able to replicate the experimental human motion activity.

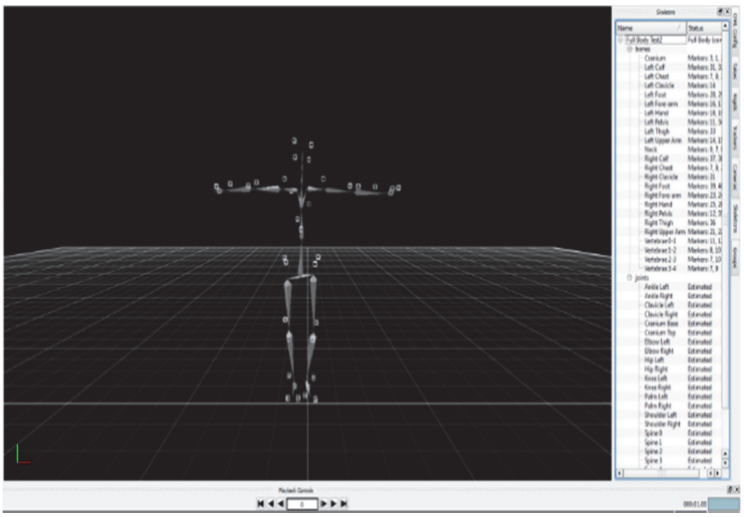

Fig. 3.3. Phasespace Recap2 software showing the human volunteer in a reference "T" position.

```
HIERARCHY
ROOT LeftArm
{
 OFFSET 0.000 0.000 0.000
 CHANNELS 6 Xposition Yposition Zposition Zrotation Xrotation Yrotation
 JOINT LeftForeArm
 {
  OFFSET 32.223 0.000 0.000
  CHANNELS 3 Zrotation Xrotation Yrotation
  JOINT LeftHand
  {
   OFFSET 23.122 0.000 0.000
   CHANNELS 3 Zrotation Xrotation Yrotation
   End Site LeftHand_End
   {
    OFFSET 8.727 0.000 0.000
   }
  }
 }
}
MOTION
Frames: 26743
Frame Time: 0.00416667
10.374 140.587 -26.247 64.426 -76.109 119.617 -11.907 -77.794 19.006 -5.951 0.771 -14.753
10.398 140.571 -26.228 64.210 -76.132 119.429 -11.719 -77.900 19.189 -6.032 0.782 -14.767
10.428 140.560 -26.211 64.331 -76.115 119.585 -11.663 -77.905 19.230 -6.022 0.780 -14.744
```

Fig. 3.4. Sample experimental trial's bvh file hierarchy with three frames of joint position and angle data.

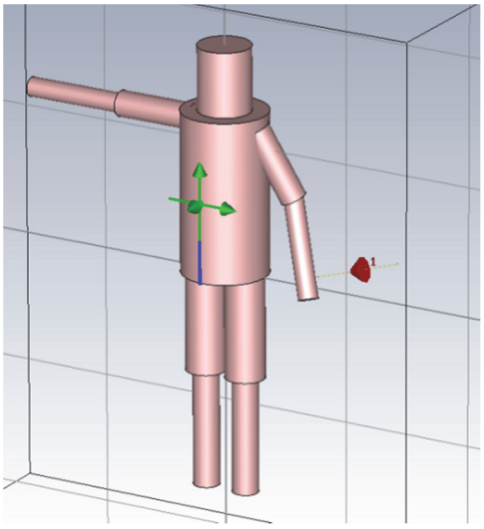

Fig. 3.5. Ten-cylinder model with antenna on the left wrist and probe on the chest.

Antennas operating at different frequencies are placed at user specified body locations to match each of the experimental configurations. The antenna models are defined as half wavelength dipoles, vertically polarized normal to the body surface. Field probes

could then be placed according to user input to sample the receiving field on the body surface. For each configuration a CST simulation is performed at each experimentally-recorded motion capture frame.

Two approximations are assumed in the simulation to save computational time: first, the material property is set to be homogeneous, equivalent muscle at each simulating frequency. For example, the permittivity and conductivity of muscle are 56.8 and 0.8, respectively at 433MHz. Mesh density is carefully selected to ensure the convergence of simulation results (15 lines/wavelength for global mesh and 0.4 inch minimum step for local antenna mesh). Second, the simulations are performed in a free space environment, while in realistic case the neighboring environments (e.g. wall, ground, etc.) must be considered. Despite of these simplifications, the simulations can produce fairly accurate estimates of the receiving signal strength and phase at the probe positions, as verified by the measurement results in the next section.

3.1.3 Comparison between Simulations and Measurements

To illustrate the above simulation method, wireless transmission data between the transmitting and receiving antennas are recorded to investigate how transmission is perturbed due to body motions. Fig. 3.6 (a) and (b) shows the experimental and simulation setup. A sample motion activity is performed during the experiments – the straight left arm is swung back and forth in the sagittal plane while the right arm is held fixed in an abducted, horizontal position. The left arm swinging motion ranges from about 90 degrees of shoulder flexion to about 50 degrees of shoulder extension (Figure 3.6 (a)). One complete cycle of arm swing is coordinated by metronome to take four seconds. The simulation results are compared with measurement data.

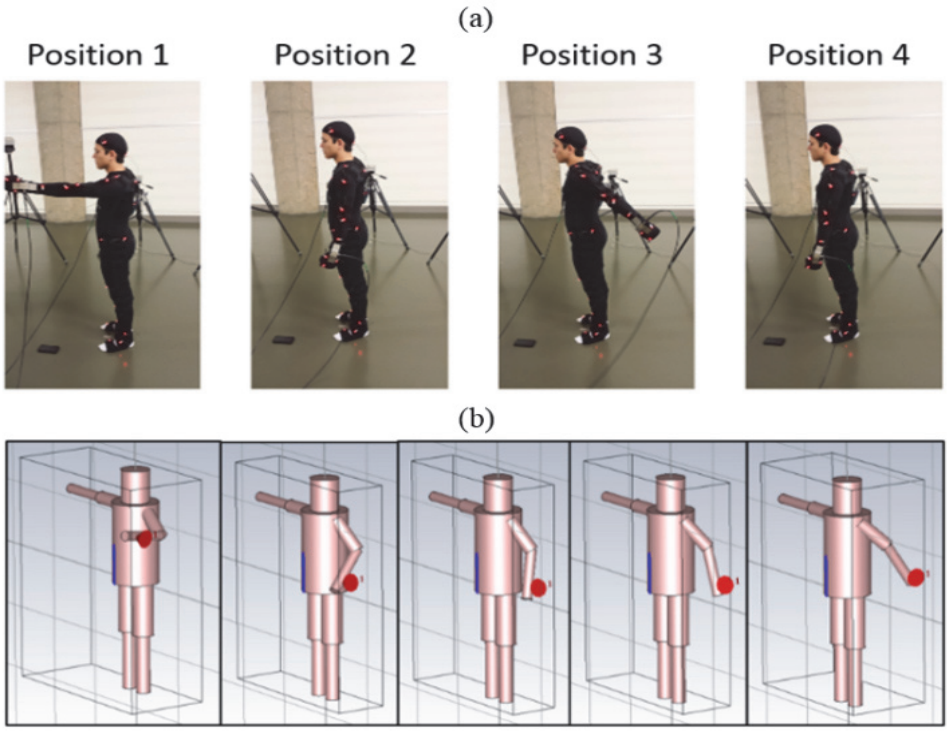

Fig. 3.6. (a) Experimental setup with volunteer wearing the 38-marker body suit and demonstrating the four second arm swing cycle. Approximately one second is taken between the shown arm positions. (b) Simulation setup of the left arm swing test represented in CST by 10 cylinder model at 433MHz. The red cone by the wrist represents the discrete port of the transmitting antenna.

Two cases are exhibited as follows. Case I: Transmitting antenna on left wrist, receiving antenna on front chest. Fig. 3.7 shows a comparison at 433MHz with the transmitting antenna at the left wrist with the receiving probe on the chest. It can be observed that both the simulation and experiment have periodic patterns with the same time interval as the motion pattern. It can also be observed that the signal strength is lower when the arm is alongside the body compared to when it is either in front of the body (shoulder flexion) or behind the body (shoulder extension). The simulation and experiment show decent agreement in terms of amplitude, period, and shape, but there are discrepancies when the arm is in front of the body. Possible reasons are the discrepancies of model

complexity, antenna types, ground plane size and environments between simulation and experiment. Another example that will be illustrated is 915 MHz antennas on the chest and the back torso case.

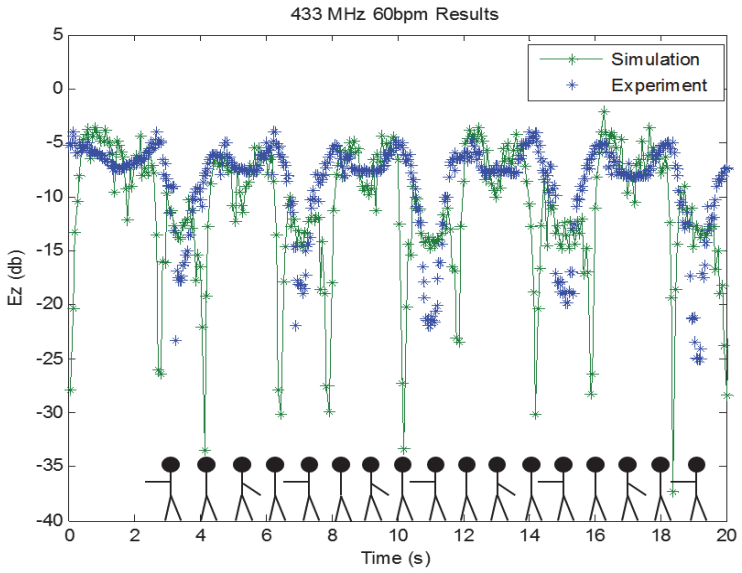

Fig. 3.7. Measured and Simulated S21 date at 433 MHz over 4 cycles of arm swing motion with transmitter on wrist and probe on chest.

Case II: Transmitting antenna on front chest, receiving antenna on back torso. Fig. 3.8 shows a comparison at 915MHz with the transmitting antenna on the chest and the receiving probe on the back, over one and half arm swing cycles. Similar to the 433MHz case, it can be observed that the signal strength is lower when the arm is alongside the body compared to when it is either in front of the body (shoulder flexion) or behind the body (shoulder extension). The 915MHz case also shows decent agreement in terms of amplitude and shape, especially considering that the simulation runs measurements on a series of snapshots of the body position and the experiments are performed with a continuous motion. In fact, apart from the discrepancy occurring around 12 seconds, a fair agreement

can be observed between the simulation and the experiment. Furthermore, this main discrepancy is not seen in the next cycle (around 16 s). Once again, discrepancies between the simplified simulation model and the experiment may be a result of environmental obstacles that were not simulated, such as the floor and walls, model complexity, ground plane size, antenna types etc.

Figures 3.7 and 3.8 are examples of the agreement found between the simulation model and our experiment. The experiment at 915 MHz with the transmitting antenna at the left wrist and the receiving probe on the chest and the experiment at 433 MHz with the transmitting antenna on the chest and the receiving probe on the back are also conducted and results shown decent agreement as well.

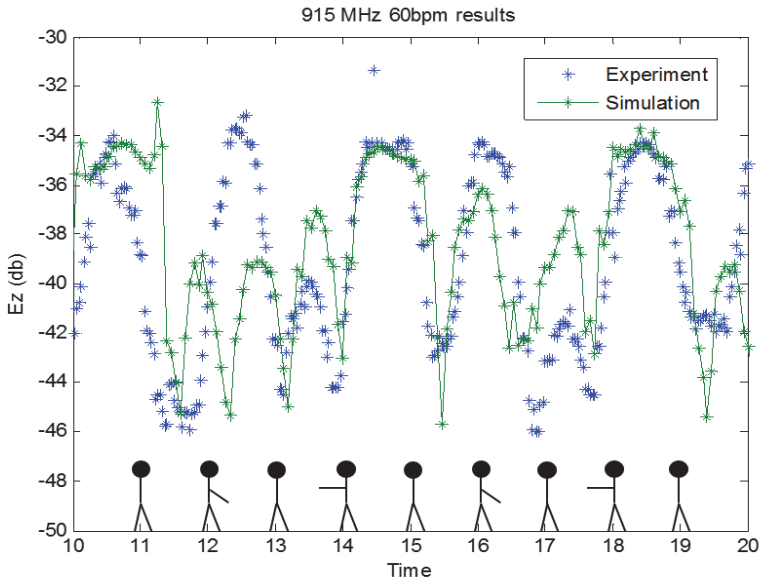

Fig. 3.8. Measured and Simulated S21 date at 915 MHz over 1.5 cycles of arm swing motion with transmitter on chest and receiving on back torso.

3.2 Human Activity Classification based on Dynamic On-body Creeping Wave Channel

In Chapter 2, wave propagations on human body are studied via experiments, simulations and theoretical analysis. It has been discovered that both space wave and surface wave effects can occur for LOS, along-body propagation, whereas creeping wave effects dominate for NLOS, around-body propagation for broadband frequencies. Recently, as mentioned in Chapter 1, several researchers attempt to exploit the on-body wireless propagation characteristics for human activity classification. Most studies to date focus on received signal strength (RSS) of LOS space wave propagation at 2.45 GHz. In this section we investigate using both the magnitude and phase of NLOS creeping waves for motion pattern recognition. We further explore the optimum of different antenna placements (channels) and antenna operating frequencies for human activity classification.

3.2.1 Dynamic Creeping Wave Measurements

Similar to the measurement setup described above, dynamic creeping wave propagation is measured using two antennas fixed respectively at the front and back torso of human body. Three pairs of antennas are used for different trials to cover WBAN frequency bands centered at 433 MHz, 915 MHz, and 2.45 GHz. As the human subjects are performing various activities (Fig. 3.2), complex transmission data S_{21} are recorded using the VNA under continuous time mode with a sampling rate of 120Hz. Two participants are included in the experiments: a 23 years male (171cm height, 62kg weight) and a 25 years old female (164cm height, 50kg weight).

Fig. 3.9 shows representative examples of the measured S_{21} parameters versus time for the six different activities at 915 MHz for both male (solid blue line) and female (dashed red line) participants. The amplitude and unwrapped phase of the signals are normalized to

one and 180 degrees for pattern recognition. It can be clearly observed that both magnitude and phase data exhibit unique periodic features depending on the activity, which implies the creeping wave channel can potentially be used to classify dynamic human movements.

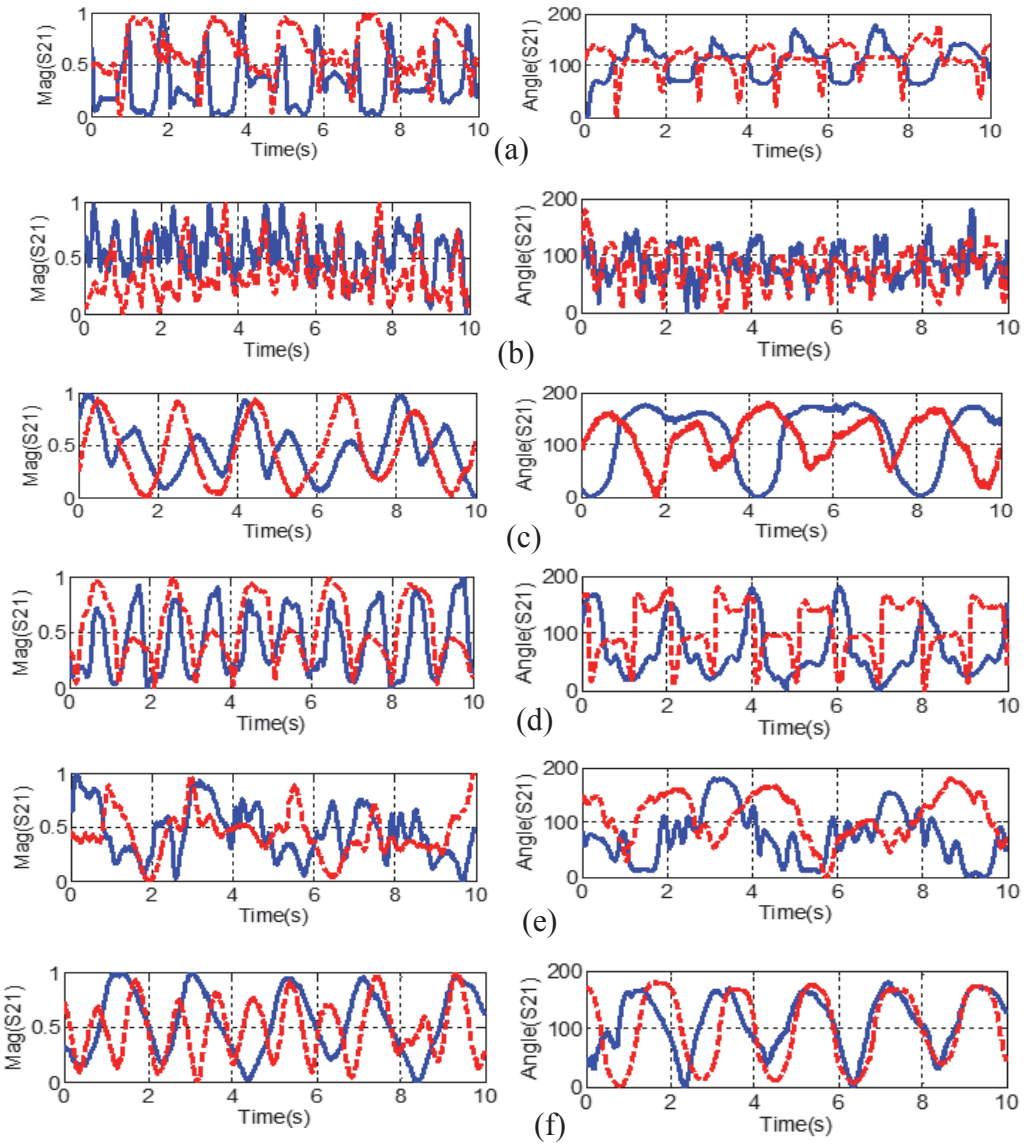

Fig. 3.9. Examples of the S_{21} parameters from chest to back antennas measured at 915MHz for six human activities: (a) boxing, (b) hopping, (c) left arm swing, (d) rowing, (e) sitting, and (f) both arms swing.

Similar observations can be made from the S_{21} measurements at 433 MHz and 2.45 GHz, as shown in Fig. 3.10 and Fig. 3.11, respectively for two representative activities (boxing and both arms swinging). In both plots, the magnitude and phase are normalized to facilitate comparison between different frequencies. It is seen that the signal magnitude decreases with the increase of frequency since the path loss is much larger for creeping waves at higher frequencies. The pattern at 2.45 GHz is difficult to recognize due to the low signal to noise ratio.

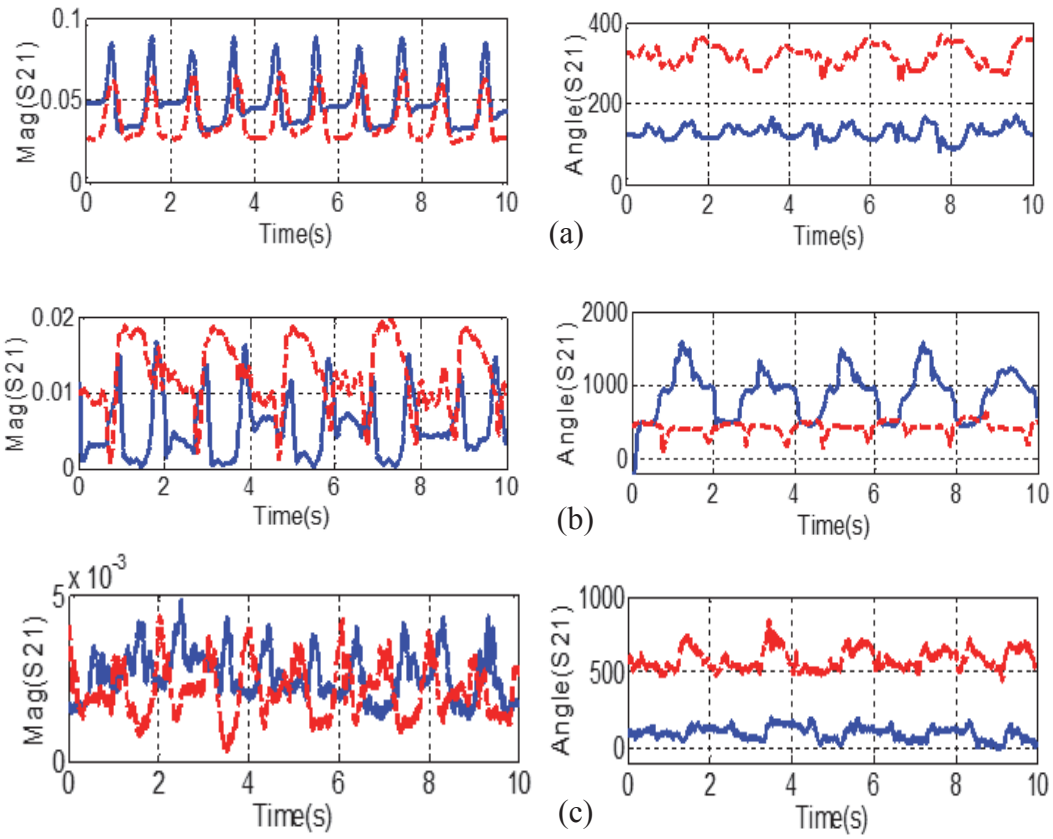

Fig. 3.10. Measured S21 parameters from chest to back antennas for the boxing activity at: (a) 433MHz, (b) 915MHz, and (c) 2.45GHz.

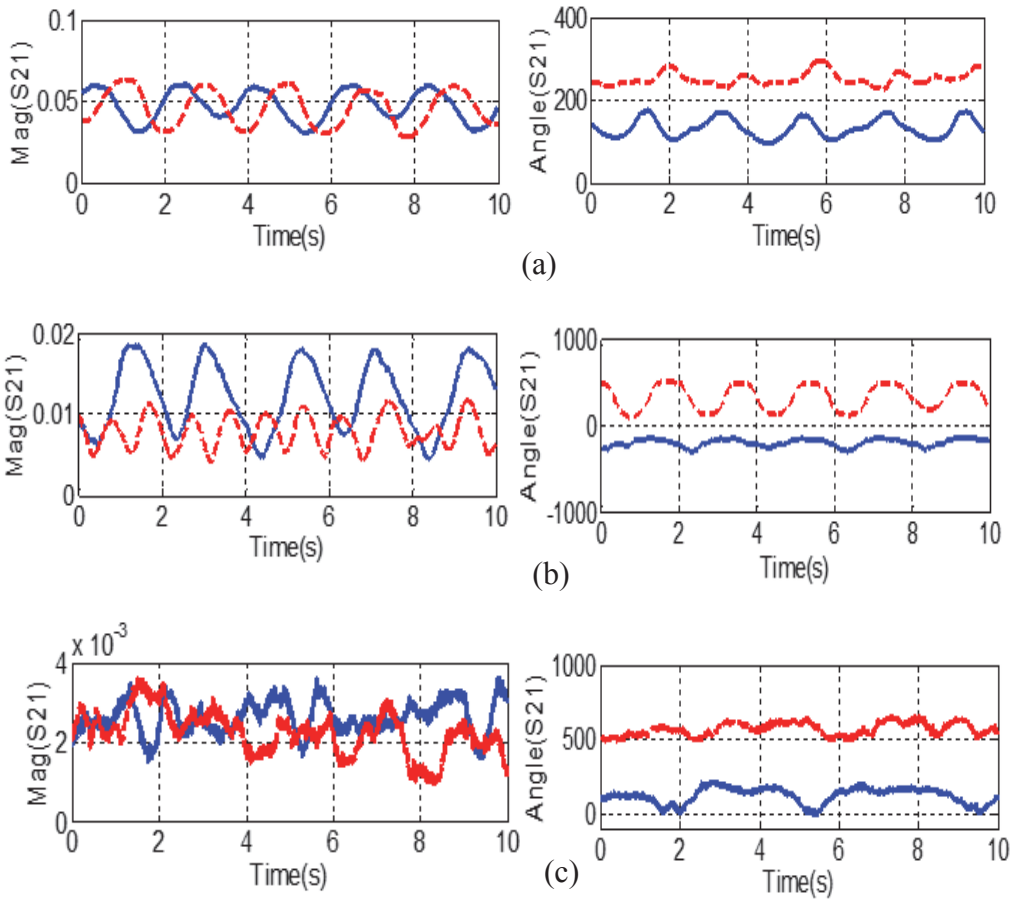

Fig. 3.11. Measured S21 parameters from chest to back antennas for both arms swinging at: (a) 433MHz, (b) 915MHz and (c) 2.45GHz.

3.2.2 Human Activity Classification with Dynamic Time Warping Technique

A dynamic time warping (DTW) algorithm is applied to classify the human motion activities of measured, time-varying transmission data. DTW facilitates assessment of the similarity of two temporal signals when one has linear or nonlinear variations in time with respect to the other [76]. DTW compensates for such time variations, which may include delay offset, acceleration, and deceleration, by optimally warping the two signals in time so that corresponding features of the signals align properly. Once aligned, the signal similarities can be assessed. DTW has been applied in diverse fields including automatic

speech recognition, video and graphic signal analysis, protein sequence alignment, partial shape matching, and micro-Doppler signature recognition [77-79]. DTW is applied in this study because the considered human motions are periodic, but can be executed at different or inconsistent rates from trial to trial.

The DTW algorithm works by creating a local cost matrix where each cell of the matrix represents the pair wise distance between samples of two data sequences, X, and Y, as shown in Fig. 3.12. The matrix diagonal corresponds to the data remaining unwrapped from the lower left cell (first sample of both sequences) to the upper right cell (last sample of both sequences). Off-diagonal cells represent data elements of one or both data sequences being shifted, or warped, in time. The DTW algorithm computes the optimal warping for each sequence by tracing a path from first to last sample such that a total cost function is minimized. The cost function is the sum of the local distance values of all cells traversed over the path. When the best path to cell i, j is defined as cell (i,j), then the next best next cell in the path can be found as:

$$cell\ (i+1, j+1) = local\_distance(i+1, j+1) + MIN(cell(i, j+1), cell(i+1, j)) \quad (1)$$

In the implementation of DTW, the data sequences (X or Y) come from experimental trials. Each of these trials results in S_{21} magnitude and phase data versus time over multiple activity cycles. As an example, X could be magnitude vs. time for one trial of male subject 1, measured at 433 MHz, and performing the sitting activity. Then, Y could be magnitude vs. time for another trial with the same frequency and subject performing the rowing activity. DTW permits us to quantify the similarity between any two experimental trials based on either the magnitude or phase data. Data from both trials are warped in time until

they agree as closely as possible with each other. The resulting, post-warped accumulated distance (cost function) between the two trials represents their DTW similarity, with lowest distance value indicating greatest similarity.

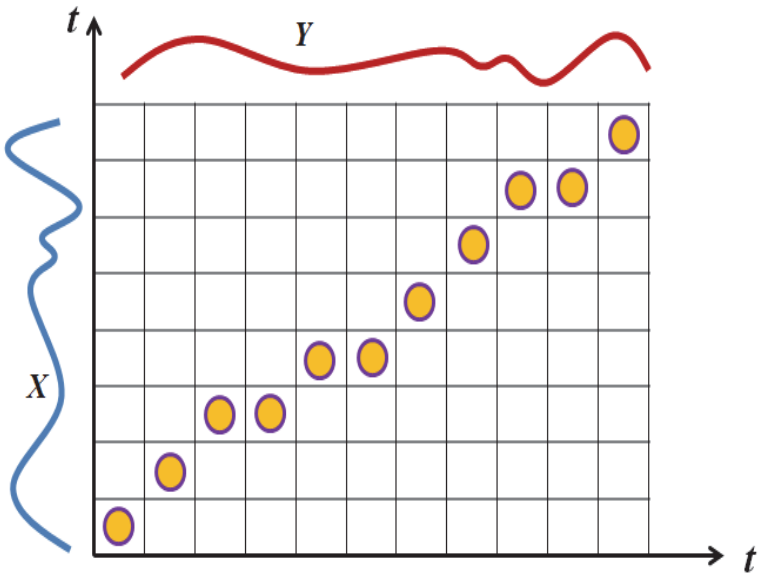

Fig. 3.12. Local cost matrix and warping path between data sequences *X* and *Y* vs. time, t.

To apply the DTW algorithm for activity classification we first selected reference data to represent each of the six activities. Ten seconds of magnitude and phase data are randomly selected from each of five trials of a known activity. The five trials are used in order to include some level of variation in the reference data, and thus to reduce the risk of bias. To classify test data of an unknown activity, an overall activity similarity is computed between the test data and the reference data for each activity. The activity for which the activity similarity is best (i.e., least summed distance) is taken as the activity classification. The classification method is tested for 40 sample data sets (ten seconds each) for each of the six activities (240 sample data sets total).

3.2.3 Results and Discussion

Fig. 3.13 shows the DTW classification results over all activities based on the magnitude and phase of dynamic creeping wave signals for male (a) and female (b) subjects, respectively. The horizontal axis represents trials using three frequencies at 433MHz, 915MHz, and 2450MHz, respectively, and the vertical axis reflects the classification accuracies. It is observed that the creeping wave data at 915MHz generally provides the best classification results for both male and female subjects. This result is likely because the signal variation at 433MHz, with its relatively large wavelength, is smaller than at the other frequencies, and because the information in the 2.45GHz signal may be contaminated by low signal-to-noise ratio. The accuracy at 915MHz for the male subject is 87.5% based on S_{21} magnitude and 88.3% based on S_{21} phase; the corresponding results for the female subject are 95.8% and 75.0%. These results suggest that the creeping wave may be an effective indicator for activity classification.

The study is then extended to compare classification results of the chest to back creeping wave channel (Ch.1) to two other commonly used on-body channels: the chest to the left wrist channel (Ch.2) and the left wrist to the right wrist channel (Ch.3). For these two additional channels we again measured the same human subjects performing the same six activities at the same three frequencies, and the DTW algorithm is repeated to post process the data. Figs. 3.14 (a) and (b) show classification results for the male subject based on S_{21} magnitude and phase. Figs. 3.14 (c) and (d) show the corresponding results for the female subject. Interestingly, it can be observed that the chest to back channel at 915MHz offers the highest classification accuracy.

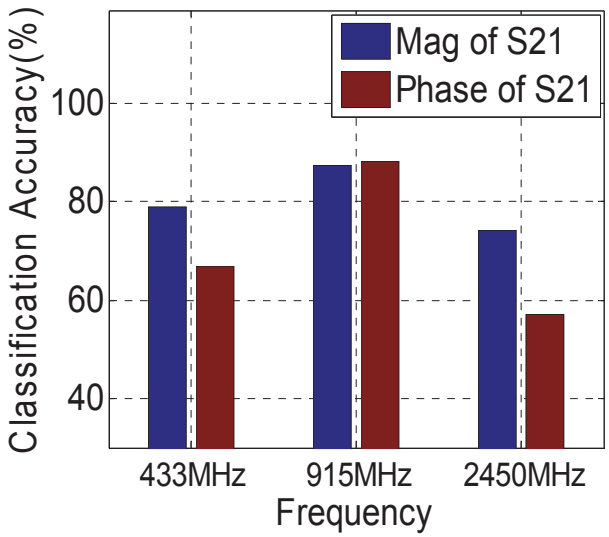

(a)

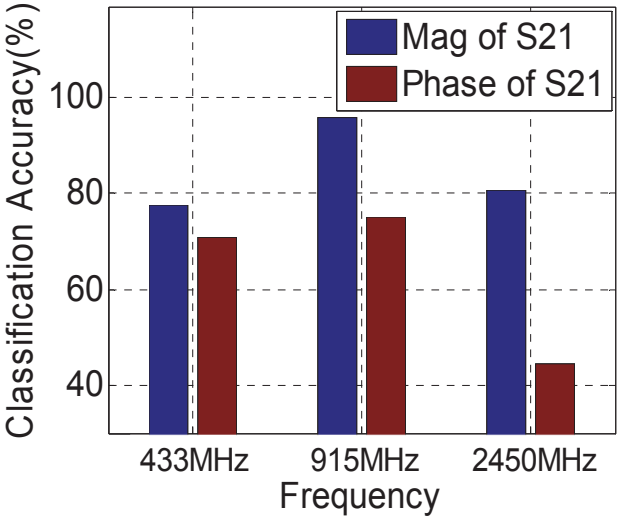

(b)

Fig. 3.13. The classification accuracy using magnitude and phase of S21 for (a) male subject, and (b) female subject.

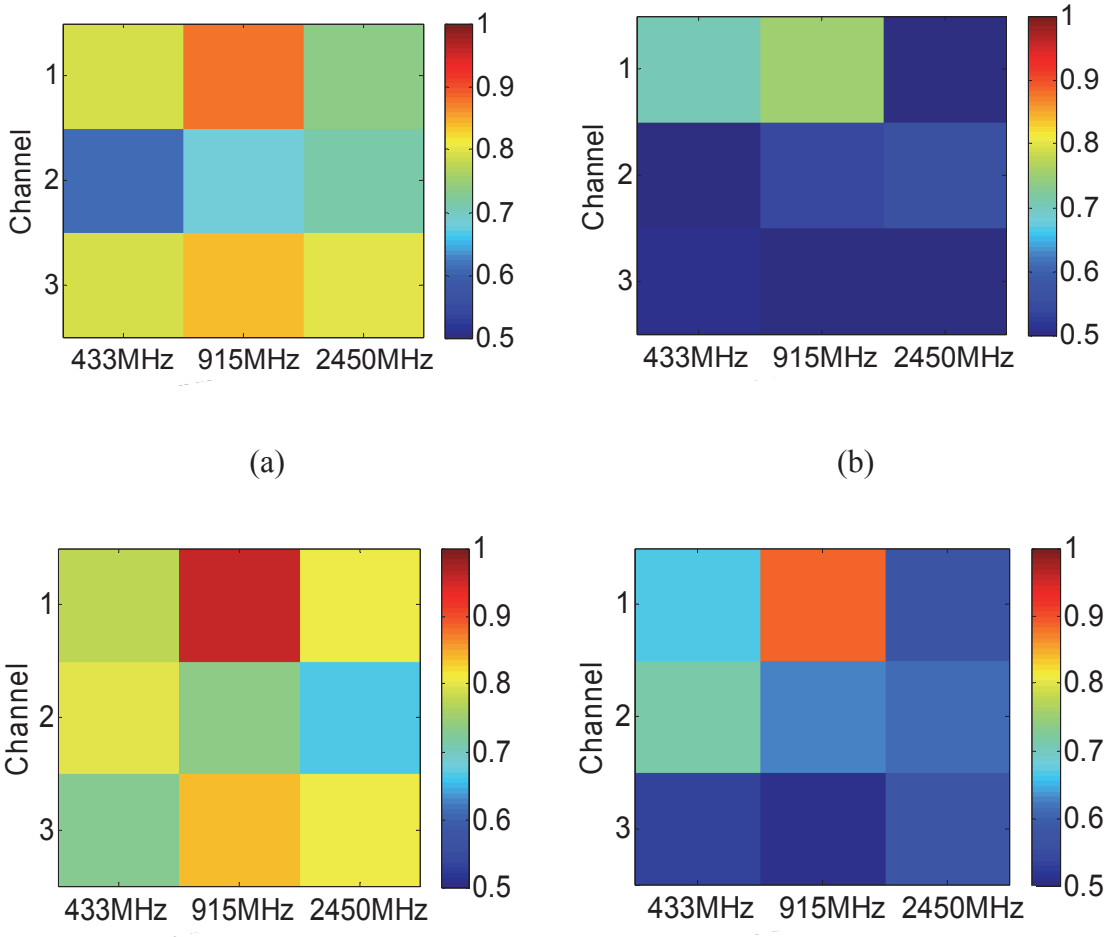

Fig. 3.14. Classification accuracy depending on different channels and frequencies, (a) male subject using magnitude of S_{21}, and (b) male subject using phase of S_{21}, (c) female subject using magnitude of S_{21}, (d) female subject using phase of S_{21}.

3.3 Summary

In this chapter an experiment and simulation platform is established to investigate dynamic on-body wave propagations. The combination of motion capture and VNA can continuously, simultaneously collect kinematic and EM data in the measurement campaign. The proposed simulation methods combine motion capture technique, construction of simplified human phantom model and electromagnetic simulations. The

good agreement is achieved between experimental data and simulated results. It is also found that analysis of on-body creeping wave signals can be effective for classifying six human movement activities. Among the three frequencies 433MHz, 915MHz, and 2.45 GHz, the 915MHz frequency provided the highest classification accuracy. Both magnitude and phase of the creeping wave transmission data provide enough unique signatures for good classification accuracy. Compared to other on-body channels, the chest-to-back creeping wave channel provides the best classification efficiency.

CHAPTER FOUR

Electrically-small Wearable Fold Cylindrical Helix (FCH) Antenna and Two-element FCH Array Design

In this chapter the electrically-small folded cylindrical helix (FCH) wearable antennas are designed at various frequencies. The antenna radiation performances on the human body are studied through experiments and simulations. A two-element FCH array is designed to achieve high gain performance. The human body effects on antenna design are also discussed.

4.1 Electrically Small Folded Cylindrical Helix Wearable Antenna

One critical challenge to implement WBAN is the miniaturization of long-lasting devices, which requires low profile antennas that can be easily worn on human body. Recently S. Best [80-81] studied the performance of several types of electrically-small antennas, and observed satisfactory radiation performances within a small electrical size. Later S. Lim *et al*. applied one of the electrically-small antennas in HF/VHF ground wave transmissions and found transmission loss within 1-2 dB of a commercial whip [82]. In the following we investigate electrically-small folded cylindrical helix (FCH) antennas for on-body applications.

4.1.1 Antenna Design

An antenna is considered to be electrically small when $ka \leq 0.5$, where k is the free space wavenumber and a is the radius of an imaginary sphere circumscribing the maximum dimension of the antenna [80]. With the decreasing size of the antenna, strong coupling

exists between wires, which can lead to undesirable effects including, but are not limited to, poor impedance matching, low radiation efficiency, and narrow bandwidth or high Q. The performance properties of electrically-small antennas are investigated by S. Best [80-81]. In his study several types of antennas, including the folded spherical helix, the folded cylindrical helix, and the disk-loaded dipole are examined. It is found that these antennas have good performance with respect to high efficiency and relatively low Q. Among these antennas, the folded spherical helix and cylindrical helix primarily operate as an electrical dipole and have vertical polarization, which makes them suitable candidates for on-body applications. For the simplicity of the optimization and further fabrication consideration, we select the FCH antenna design for our study.

Fig. 4.1. (a) shows the geometry of our FCH antenna simulation model. The antenna consists of four copper arms. Each arm is a single turn cylindrical helix offset 90 degrees apart from each other on the ground. On top the four arms are folded together to form a criss-cross to get a good impedance match. The modeled antenna is mounted on an infinitely-large, perfectly electrical conducting (PEC) ground model. A voltage source is fed to the base of one arm, where the other three arms connect to the ground. Similar to Best's paper, we first set ka=0.373 and make the height h to be the same as the cylinder radius a. The geometrical parameters and wire radius are scaled to the design frequency 433 MHz and 915 MHz, respectively. In order to examine its performance, we use the conventional quarter-wavelength monopole as a benchmark study, as shown in Fig. 4.1. (b). The reflection coefficients and gains of both antennas at 433 MHz are simulated in MOM-based FEKO software. The results are plotted in Fig. 4.2. (a) - (b).

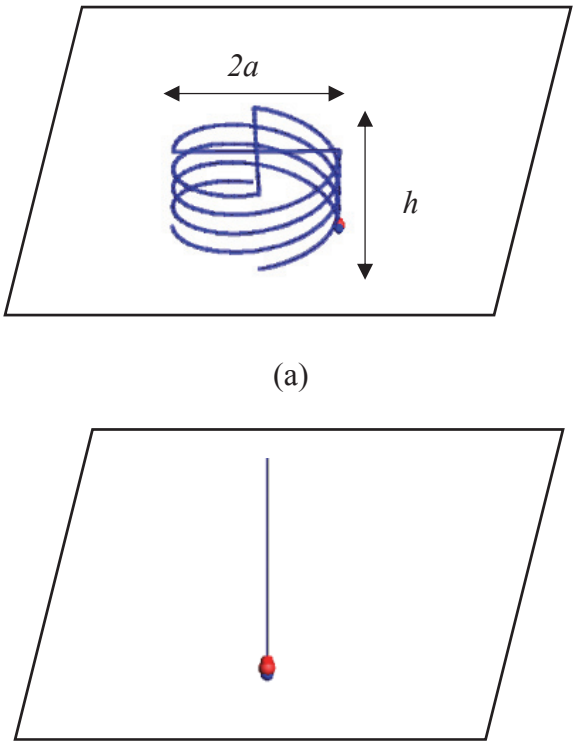

Fig. 4.1. Antenna geometry: (a) folded cylindrical helix (b) monopole.

Fig. 4.2. (a) shows the simulated reflection coefficients against frequency. The geometrical parameters of the antennas are tuned to get the lowest VSWR at the design frequency. The heights and the wire radius of both antennas are listed in Table I. It can be seen that at 433 MHz, the height of the FCH is 3.05 cm, which is less than 1/5 that of the monopole. The wire radius is 0.9 mm, which is thicker than the monopole but still acceptable. The -10 dB bandwidth of the FCH and monopole is 1.62% and 10.16%, respectively. The bandwidth of the FCH is much narrower due to its small electrical size. So there is a tradeoff between size and bandwidth. Fig. 4.2. (b) shows the gains of both antennas. The gain is relatively stable across frequency for both antennas. At the center

frequency, the gain of FCH is 4.73 dBi, which is almost twice that of the infinitesimal dipole. For the monopole, the gain is 5.13 dBi, which is twice that of the half-wave dipole.

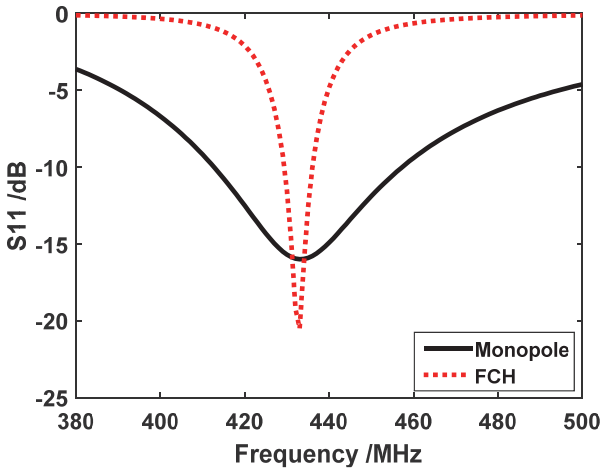

(a)

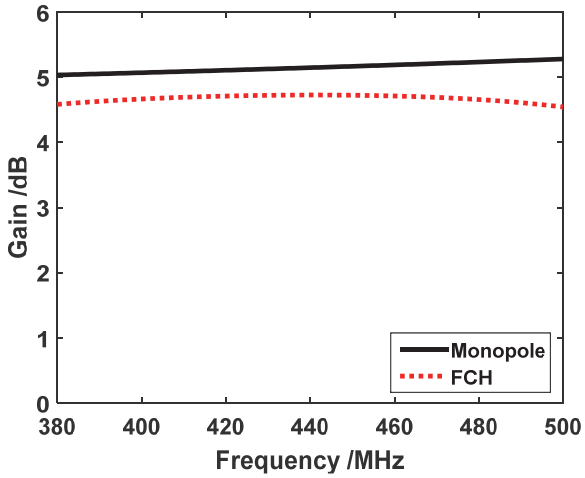

(b)

Fig. 4.2. Simulated (a) reflection coefficient (b) gain for FCH and monopole.

The FCH and monopole are also designed at 915 MHz. The antenna geometrical parameters and performances are compared in Table 3. It can be found that as the frequency increases, the height and wire radius of the FCH decreases. Compared with the monopole,

the height is less than 1/5 while the bandwidth is narrower. Both antennas achieve good gains around 5 dBi. The radiation patterns have been checked for both FCH and monopole (Figs. 4.3) and they are very similar to each other. The maximum gain is in the horizontal direction and the azimuth radiation pattern is isotropic.

Table 3. Comparison of antenna performance

Antenna	433 MHz FCH	433 MHz Monopole	915 MHz FCH	915 MHz Monopole
Height	3.05 cm	16.75 cm	1.44 cm	7.85 cm
Wire radius	0.9 mm	0.5 mm	0.4 mm	0.5 mm
Bandwidth	1.62 %	10.16 %	1.64 %	7.89 %
Gain	4.73 dBi	5.13 dBi	4.69 dBi	5.17 dBi

4.1.2 Simulation on the Human Phantom Model

To investigate the antenna's effect on the human body, full wave FEKO simulations are performed with the FCH antenna placed on the human phantom. In previous chapter, wave propagations from a monopole antenna are simulated on a simplified human phantom model. Two propagation paths: along the body (line-of-sight, LOS) and around the body (non-line-of-sight, NLOS) are studied. For these two paths, the human phantom model can be simplified into an infinitely-large muscle ground and a finitely-sized muscle cylinder, respectively. Therefore, for the FCH, the simulations are done in both paths, LOS and NLOS, respectively.

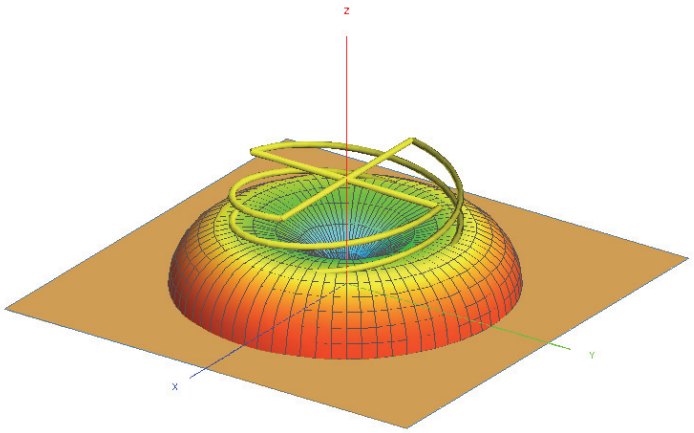

(a)

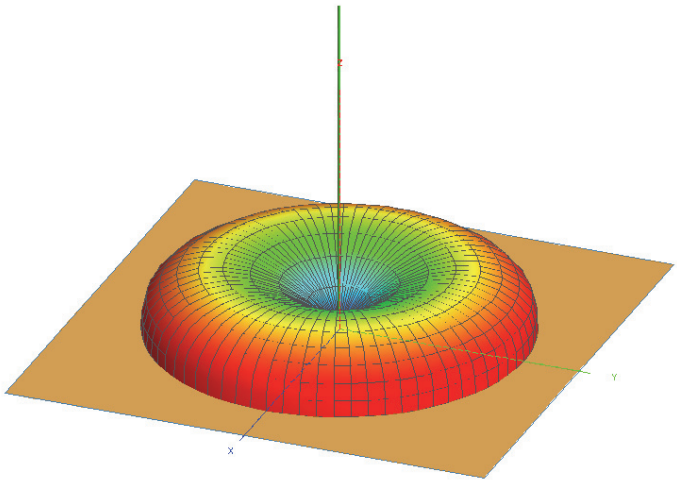

(b)

Fig. 4.3. Simulated 3D far field radiation pattern (a) FCH (b) monopole.

4.1.2.1 Wave Propagation along Human Torso (LOS). In Fig. 4.4, the FCH antenna is placed 1.5 cm above an infinitely-large ground plane filled with homogenous muscle tissue (ε_1=56.87, σ=0.80 for 433 MHz and ε_1=54.99, σ=0.84 for 915 MHz). The upper medium is air. The antenna is attached on a rectangular copper patch ground plane (7 cm

* 7 cm for 433 MHz and 4 cm * 4cm for 915MHz). The near electric fields Ez are collected 1.7 cm above the muscle ground at every 3 cm straight along the y axis.

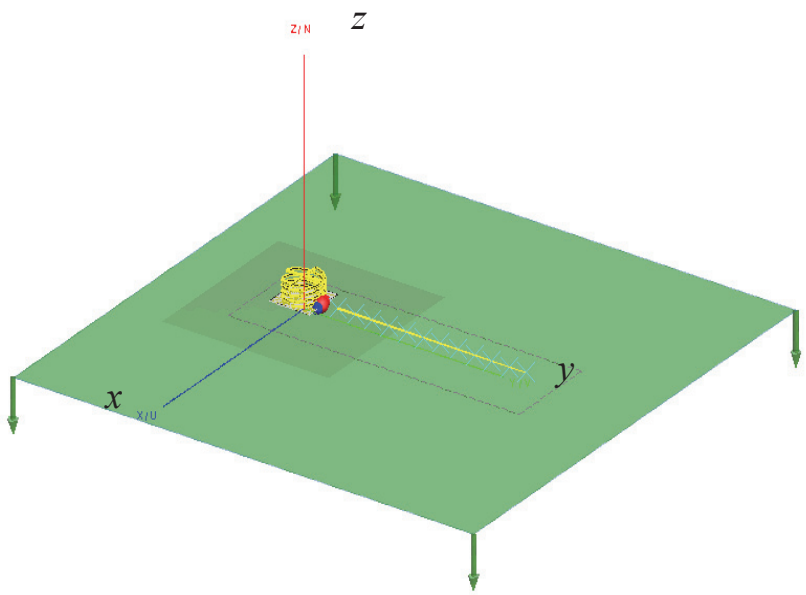

Fig. 4.4. FCH simulation setup for LOS propagation.

Fig. 4.5. shows simulation results compared with those of the previous simulations, along with corresponding experimental data. In the figure the normalized transmission loss is plotted against distance between antenna and various observation points (ranging from 10 to 40 cm away) at 433 MHz and 915 MHz. Specifically, the figure plots normalized $|S_{21}|$ with antenna mismatches $|S_{11}|$ and $|S_{22}|$ removed. The label 'M' stands for monopole.

As can be seen in Fig. 4.5, the signal drops as the distance increases, which is similar to the behavior of ground wave propagation. It can also be seen that the FCH simulation agrees well with both the monopole simulation and measurement results at each frequency. The differences between FCH and monopole simulation results are within 2 dB at any

single frequency. This indicates that the FCH antenna can excite the same wave mechanism as the monopole, but with its much smaller electrical size.

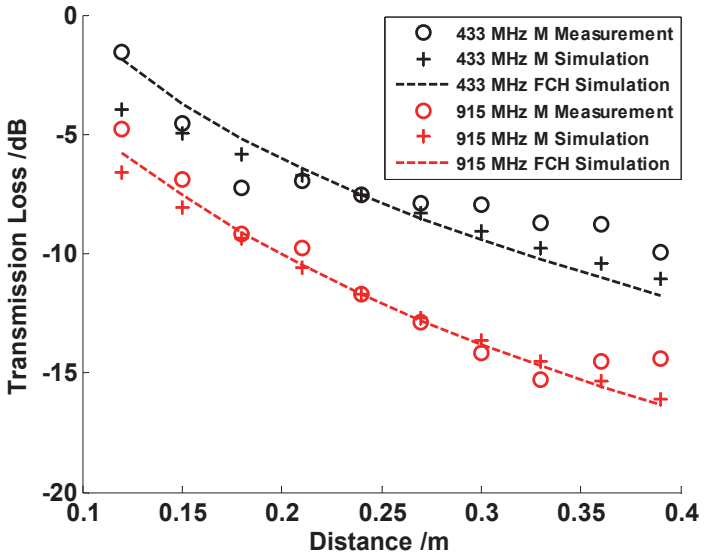

Fig. 4.5. LOS transmission loss comparison of FCH simulation, monopole simulation and monopole measurements.

4.1.2.2 Wave Propagation around Human Torso (NLOS). In Fig. 4.6, the FCH simulation is performed for NLOS propagation. The torso is modeled as a finite-size cylinder filled with homogenous muscle tissue property. The height and circumference of the cylinder are set to 48.26 cm and 85.09 cm, respectively, corresponding to the human test subject. The FCH antenna is oriented radially in front of the cylinder at mid-height level. Near electric field data are collected by probes every 1.5 cm horizontally around the cylinder at the same level.

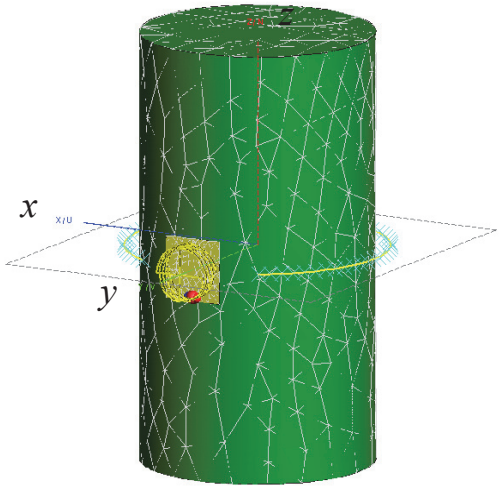

Fig. 4.6. FCH simulation setup for NLOS propagation.

Fig. 4.7 shows the NLOS normalized transmission loss against distance of the observation points around the torso (6 cm ~ 81 cm) for the FCH simulation, monopole simulation, and measurement at the two frequencies. Among these frequency bands, the results show good agreement. At each frequency the receiving field strength first drops very quickly with distance around the torso, then levels out at the human's back, and finally increases again to the initial level. This pattern illustrates the creeping wave phenomena, where the wave creeps around the torso in both directions from the transmitter (left side and right side). As the receiver gets farther from the transmitter around to the left side, the signal strength decreases. When the receiver is at the back, waves from both directions interfere with each other. As the receiver continues around toward the right side, the dominant wave from the right side reaches it with most strength. The smaller FCH antenna design appears able to excite this on-body creeping wave mode like the monopole.

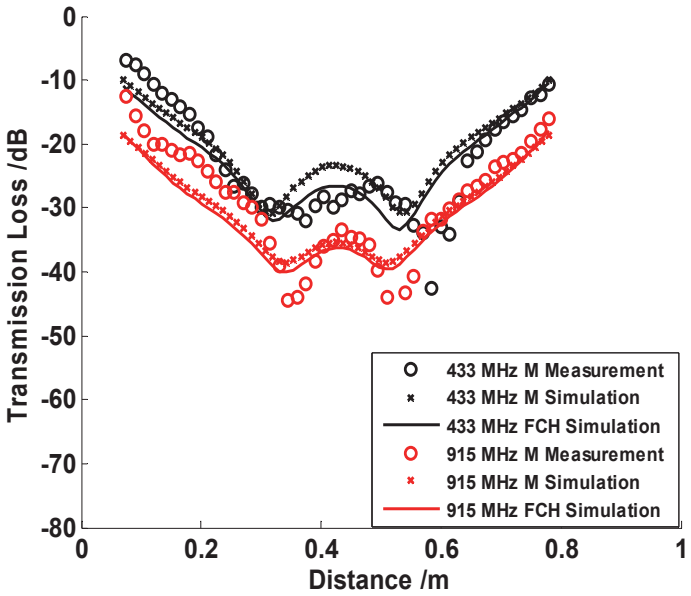

Fig. 4.7. NLOS transmission loss comparison of FCH simulation, monopole simulation and monopole measurements.

4.1.3 Fabrication and Measurement

The FCH antenna prototype is fabricated and measured. Due to the small size, it is difficult to make a sole antenna. A 3D printer (MakerBot Replicator 2) is used to print out the antenna's holding structure with grooves. The material of the structure is polylactic acid (PLA). The 28 Gauge copper wires are wound around the mold. The antennas are soldered on the copper ground plane with 2.5*2.5 cm^2 for 2.45 GHz and 4*4 cm^2 for 915 MHz, respectively. A PCB connector is fed at the bottom side of one arm. The fabricated antenna can be seen in Fig. 4.8 (a) and (b).

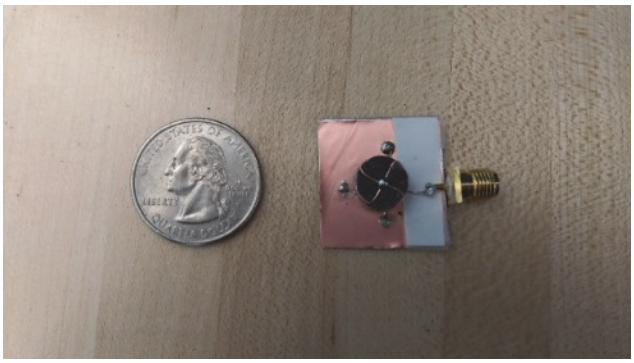

(a)

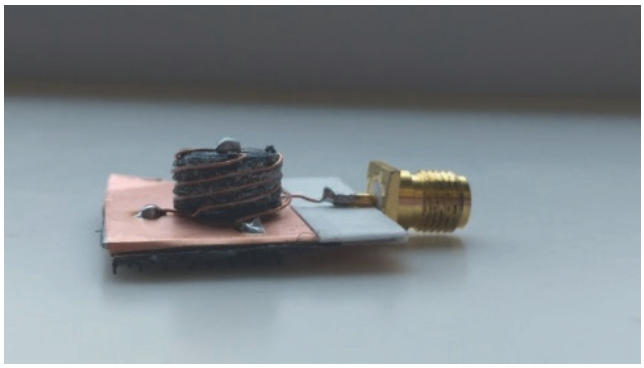

(b)

Fig. 4.8. Fabricated FCH antenna at 2.45 GHz (a) top view compared to a quarter (b) side view.

The measured reflection coefficients are plotted in Fig. 4.9 (a) and (b) for antennas at 915 MHz and 2.45 GHz, respectively. It can be found that the -10 dB bandwidth is narrower for FCH antenna than that of the monopole, as we discussed before. It can also be observed that the resonant frequency shifts to lower ranges, especially for 915 MHz antenna. The discrepancies are possibly due to the plastic mold structure, finite size ground and fabrication issue. The mold effects are studied via FEKO simulations. The dielectric constant of PLA is set to 2.5 [83]. The comparisons of S11 are shown in Fig. 4.10 (a) and (b). Both resonant frequencies of simulation and measurement with mold shift to lower ranges, indicating that the plastic mold can increase the electrical length. A pair of FCH is

applied as TX and RX to measure on-body propagations. Fig. 4.11 (a) shows the measurement setup for NLOS propagation. Fig. 4.11 (b) is the normalized transmission loss between the monopole and FCH at 2.45 GHz. The similarity of two curves indicate that both antennas can excite creeping wave mechanism.

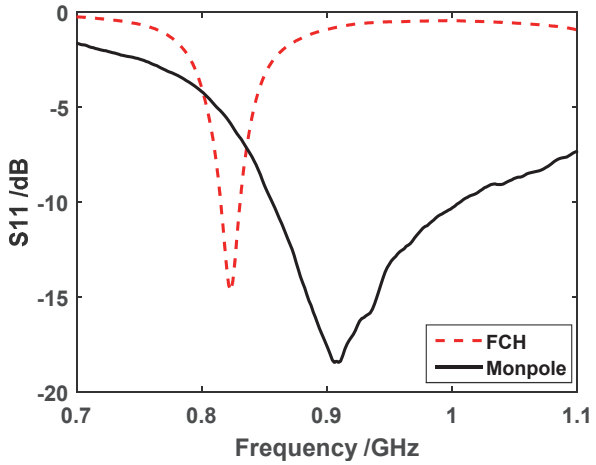

(a)

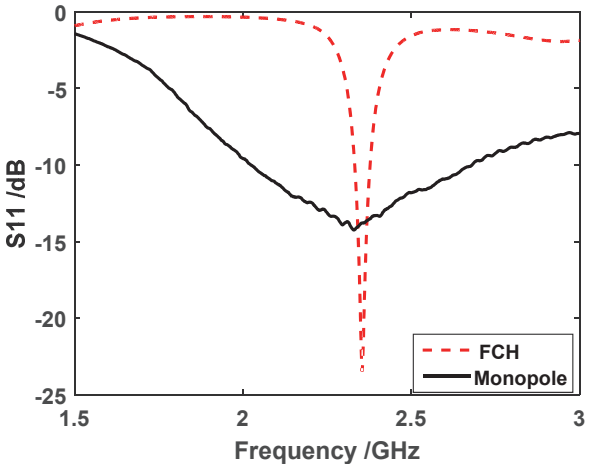

(b)

Fig. 4.9. Measurement of S11 (a) 915 MHz antenna (b) 2.45 GHz antenna.

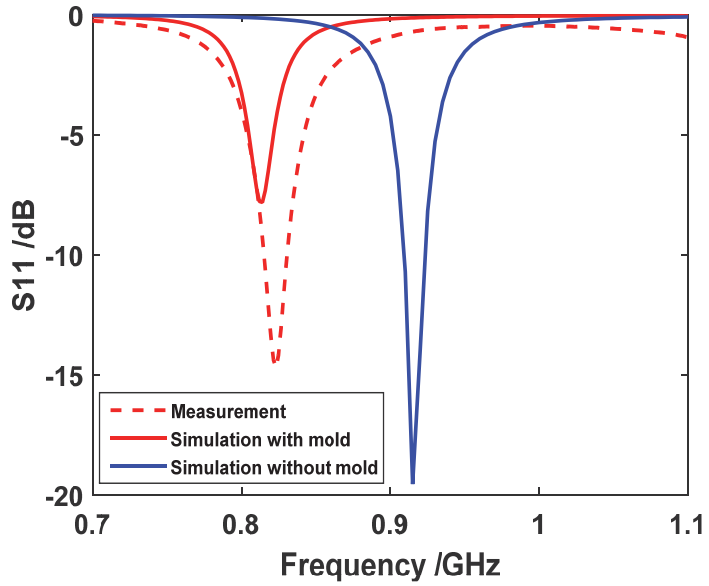

(a)

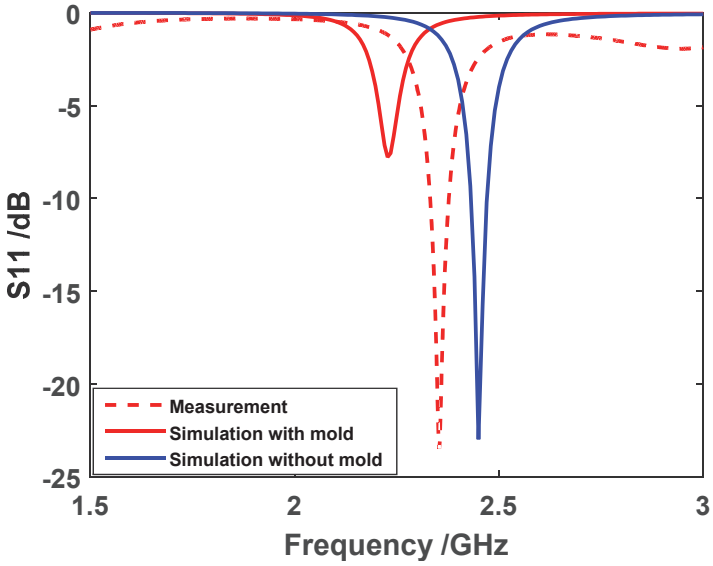

(b)

Fig. 4.10. Mold effects of FCH (a) 915 MHz antenna S11 (b) 2.45 GHz antenna.

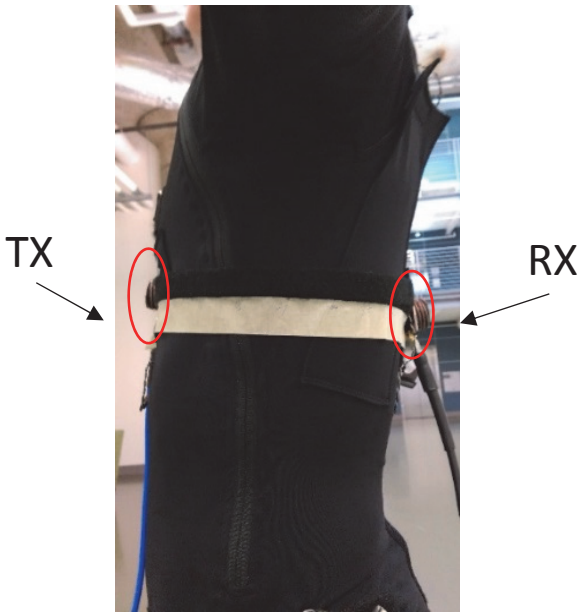

(a)

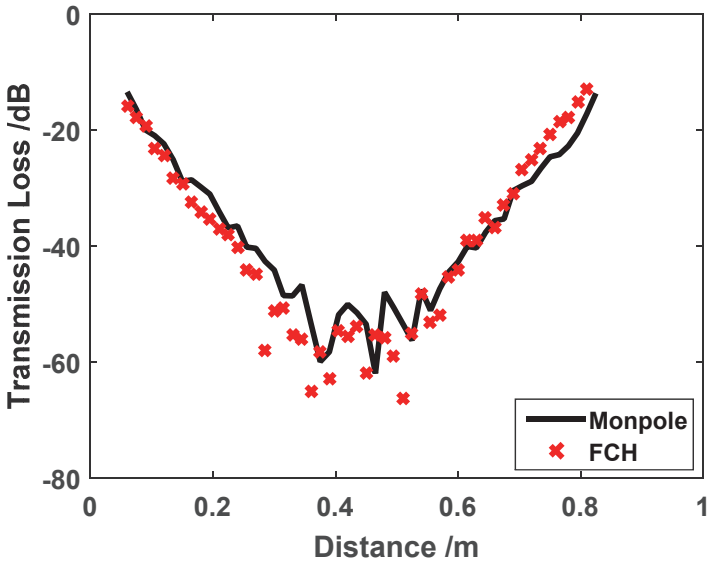

(b)

Fig. 4.11. NLOS FCH propagation measurement (a) measurement setup (b) measured transmission loss at 2.45 GHz.

4.2 Implementation of 1-D FCH Array

In the previous section, the radiation performance of a single FCH is examined and it is similar to that of a monopole case with omni-direction. In order to make the antenna more directive with a high gain, an antenna array is preferred [68]. We first consider a two-element FCH array with setup in Fig. 4.12. Two FCH antennas are placed on an infinitely-large ground plane with heights h_1, h_2 and spacing S_0. The radius of FCH is set to be equal to h_1 and h_2, respectively, as what has been done previously. A 1 V voltage source is fed at the bottom of one arm of the left FCH. The genetic algorithm (GA) is applied to optimize h_1, h_2 and S_0 for the maximum gain at the azimuth plane. The optimum radiation pattern is shown in Fig. 4.12. The maximum gain is 8.71 dBi at -y axis with F/B ratio 5.13 dBi at 2.45 GHz. The optimized h_1=0.042 λ_0, h_2=0.044 λ_0 and S_0=0.283 λ_0, while λ_0 is the free space wavelength at a design frequency at 2.45 GHz.

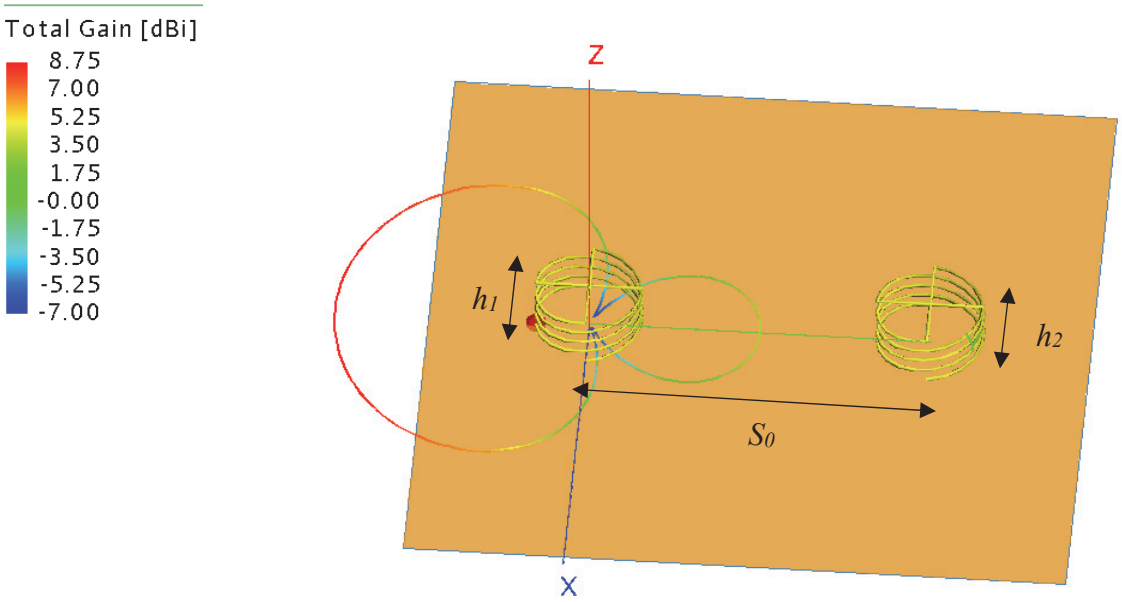

Fig. 4. 12. Optimized radiation pattern of a two-element FCH array on PEC ground.

Further a two-element FCH array with a small copper ground is placed on an infinitely-large homogenous muscle ground plane, as seen in Fig. 4.13. In order to compare with the single FCH case in Fig. 4.4, the antenna array is 1 mm above the muscle ground. The radius of both FCHs are the same with single FCH of height h=0.044 λ_0, the spacing s between two elements is 0.25 λ_0, the copper ground size is $L*W$ = 0.072*0.035 m. A 1V voltage source is fed at the bottom side of one FCH arm.

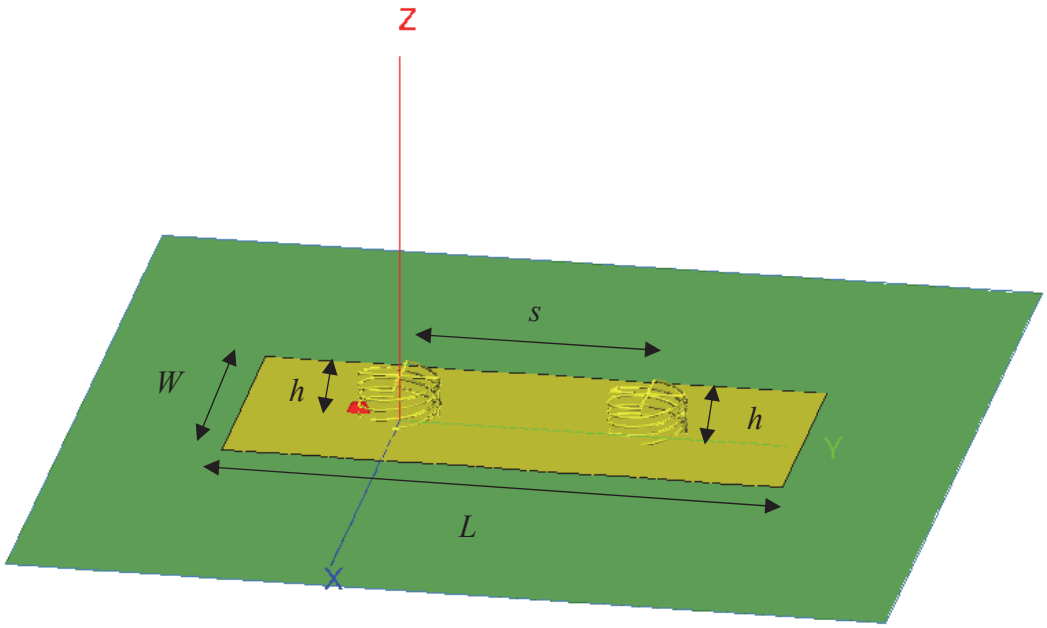

Fig. 4.13. Two-element FCH array on an infinitely-large muscle ground plane.

The comparison of antennas' performances are listed in Table 4. Reflection coefficients and near electrical fields are simulated and collected. The distance d is the length between port and E-field probe. It can be found that the resonant frequency shifts to lower frequency, which is due to the presence of the muscle ground. All antennas resonant at 2.4 GHz. For each frequency, near electrical fields decreases as distance goes further. It

can also be seen that the two-element FCH array gets strongest E-field strengths for each frequency at each distance. This indicates that the two-element FCH can provide strongest signals on the human body.

Table 4. Comparison of antenna and antenna array performances at two frequencies.

FCH	Frequency	S11	E (d=0.2m)	E (d=0.3m)	E (d=0.4m)
Single	2.45 GHz	-3.92 dB	2.53 V/m	1.55 V/m	1.08 V/m
Two-element	2.45 GHz	-7.6 dB	4.06 V/m	2.52 V/m	1.77 V/m
Single	2.4 GHz	-13.7 dB	6.24 V/m	3.83 V/m	2.68 V/m
Two-element	2.4 GHz	-18.78 dB	8.84 V/m	5.55 V/m	3.94 V/m

4.3 Human Body and Other Effects on Antenna Design

In order to place antennas on the human body, ground plane size and type must be considered. An alternative FCH antenna is studied using previous 'bridge' ground plane, as shown in Fig. 4.14. The antenna is fed by a 90 degree SMA connector. The measured reflection coefficients are compared with the PCB feeding antenna, as shown in Fig. 4.15. It can be observed that the resonant frequency of bridge FCH on the human middle chest shifts 15 MHz compared to that of the open space, while the PCB feeding antenna shifts 44 MHz from the open space. The major difference is caused by the ground plane gap from the body surface. Therefore, the effects of different heights above the human muscle ground on FCH are studied and results are plotted in Fig. 4.16. It can be seen that as the antenna is placed closer above the body, the resonant frequency becomes lower. This is due to the dielectric human tissue property. The electrical length becomes longer as the antenna is closer to the body tissue so that the resonant frequency will decrease. The body

tissue also has conductivity, which will cause resistance loss. From the plot we can see that the impedance matches better when the antenna is placed at a higher position, indicating that the ground plane size has a more significant effect than the conductivity of the tissue. The gap effect on the transmission loss is also investigated in Fig. 4.17 and Fig.4.18, for LOS and NLOS cases, respectively. It can be seen that the transmission data (after normalized to S_{11} and S_{22}) has no substantial difference for different gaps, indicating that both PCB feeding and bridge FCHs are able to excite on-body waves efficiently.

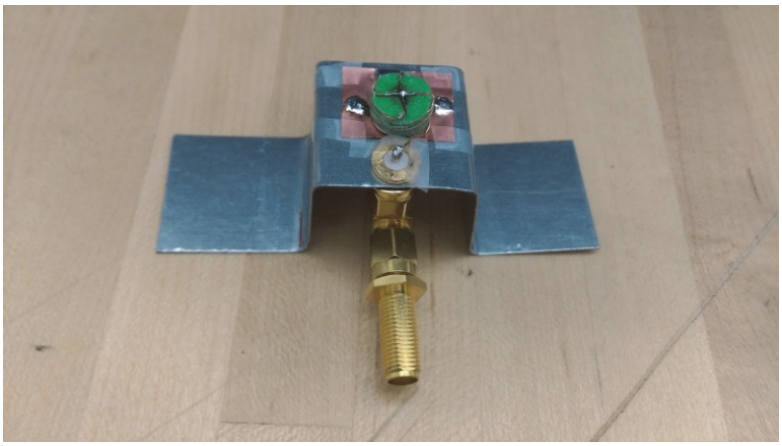

Fig. 4.14. Bridge shape FCH antenna at 2.45 GHz. The ground plane dimension is 2.5*2.5*1.5 cm^3.

As mentioned in Section 4.1.1, the folded spherical helix antenna (FSH) also operates as a vertical monopole. The FSH is investigated in FEKO simulation. The geometry can be viewed in Fig. 4.19. The comparison of reflection coefficients are plotted in Fig. 4.20. It can be seen that both FCH and FSH can achieve good impedance match at 2.45 GHz. The -10 dB bandwidth for FSH (90MHz) is broader than FCH (40 MHz). However, the dimensions of FSH is greater than FCH. So there is a tradeoff between size and bandwidth. The geometries and performances of FCH, FSH and monopole are compared in Table 5. It

can be found that the FCH has the smallest height and wire radius but has a narrower bandwidth. The gain of three antennas are similar between 4.6 and 5 dBi.

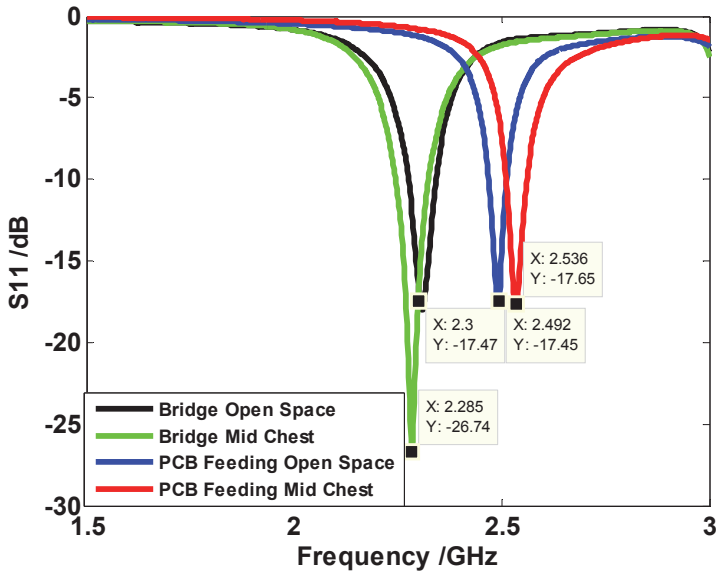

Fig. 4.15. Measured reflection coefficients for bridge shape and PCB feeding antennas at 2.45 GHz.

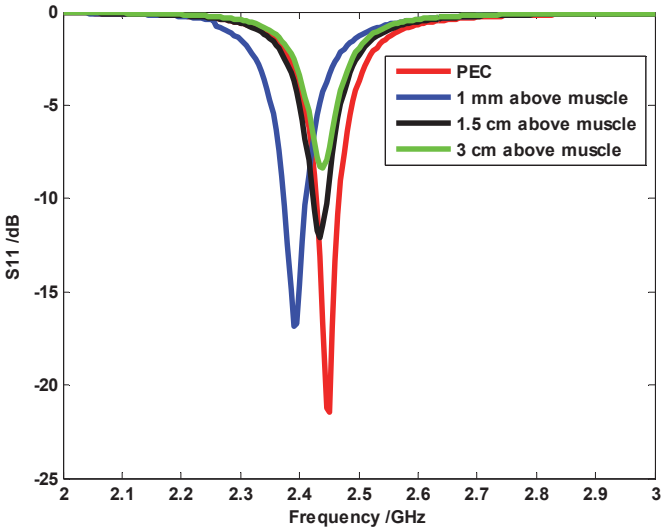

Fig. 4.16. Simulated reflection coefficients for FCH antennas on PEC ground and different heights above the human muscle ground at 2.45 GHz.

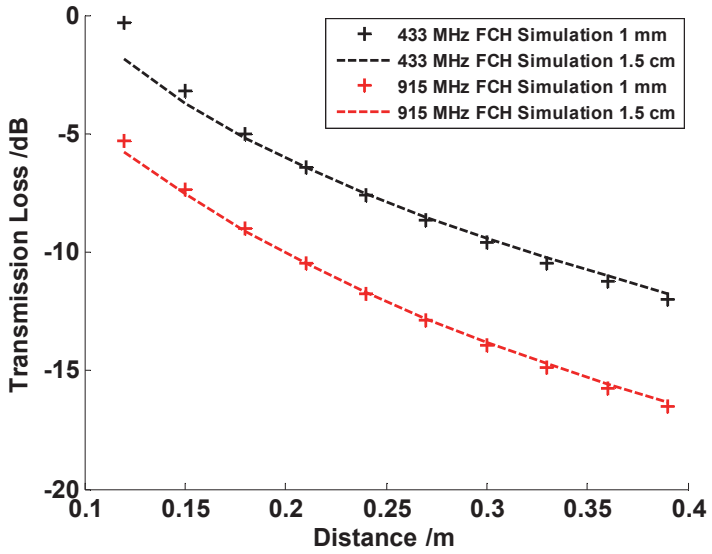

Fig. 4.17. Normalized transmission loss at different heights above the infinitely-large mucle ground plane (LOS) for antenas at multiple frequencies.

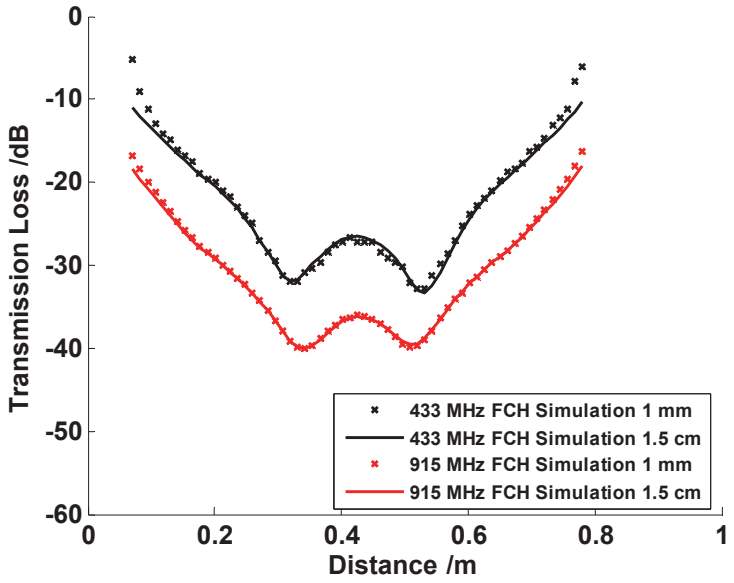

Fig. 4.18. Normalized transmission loss at different heights above the finite height muscle cylinder (NLOS) for antenas at multiple frequencies.

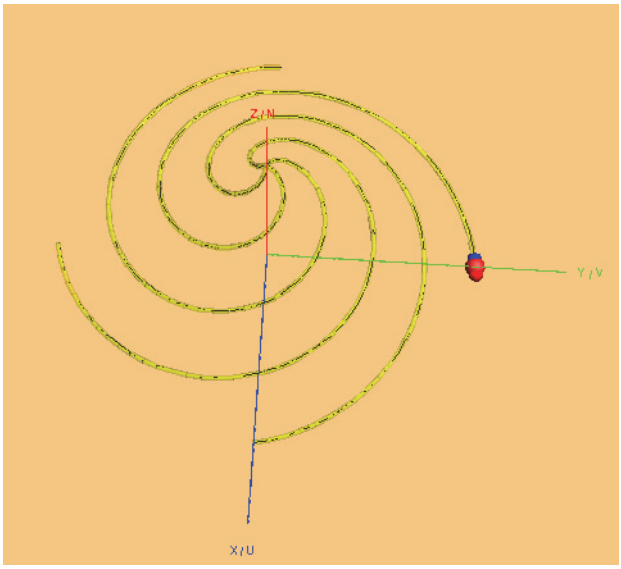

Fig. 4.19. Folded spherical helix antenna prototype in FEKO.

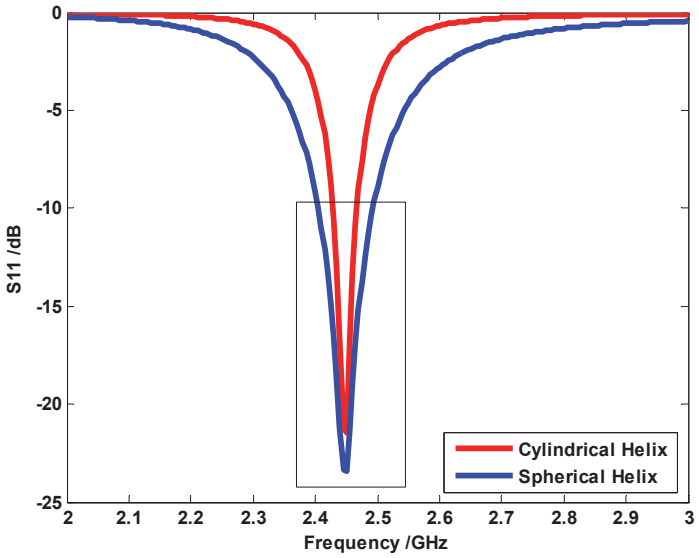

Fig. 4.20. Simulated reflection coefficients comparison for cylindrical helix and spherical helix operating at 2.45 GHz. The rectangular box shows -10 dB bandwidth.

4.4 Summary

In this chapter electrically-small folded cylindrical helix (FCH) antennas are designed at multiple frequencies and the performances on the human body are simulated and measured. It is found that the FCH antenna can achieve a high gain as well as excite the same on-body wave propagation mechanisms as the monopole while its height is significantly reduced. Two element FCH array is proposed using Genetic Algorithm and the radiation performance is enhanced. The study indicates that the FCH is a good antenna candidate for low-profile WBAN communication devices. Human body effects on antenna performance are analyzed and alternative antenna design is discussed.

Table 5. Comparison of three types of antenna performance at 2.45 GHz.

Antenna	Cylindrical Helix	Spherical Helix	Monopole
Height	0.54 cm	1.23 cm	2.91 cm
Wire radius	0.16 mm	0.16 mm	0.5 mm
Bandwidth	1.63 %	3.67 %	15.63 %
Gain	4.62 dBi	4.69 dBi	5.14 dBi

CHAPTER FIVE

1-D Closely-Spaced, Multi-Element Parasitic Antenna Array

Previously we have seen that the two-element antenna array can achieve a higher gain and be more directional than a single antenna. In this section we are going to investigate a closely-spaced, multiple element parasitic antenna array for an electrically small and super directive antenna. The wire array is studied to prove concepts of this kind of antenna array.

5.1 Overview of Parasitic Antenna Array

Design of a closely-spaced parasitic antenna array is of great interest in recent years for its potential application as an electrically small, super directive antenna. O'Donnell and Yaghjian proposed a two-element parasitic array design optimized using the genetic algorithm (GA) [84], in which the spacing between the driving element and the parasitic element is $0.115\lambda_0$. Bayraktar et al. presented a compact, three-element stochastic Yagi-Uda array design using the particle swarm optimization algorithm (PSO) [85]. The spacing between their reflector and driver, and driver and director are $0.11\lambda_0$ and $0.036\lambda_0$ respectively. Lim and Ling utilized GA to design a two-element, electrically small, reconfigurable Yagi antenna for HF skywave applications [86] and they successfully reduced the element spacing to $0.02\lambda0$. Arceo and Balanis reported a three-element, enhanced bandwidth Yagi antenna with inter-element spacing set at $0.053\lambda_0$ [87]. In all the above examples, the spacings between array elements are much smaller than that of a conventional Yagi-Uda antenna which inter-element spacing ranges from $0.15\lambda_0$ to $0.4\lambda_0$.

One common challenge needs to be addressed in the above designs is the strong mutual coupling between array elements due to the reduced spacing. Such strong coupling can result in several undesirable effects including, but not limited to, low radiation resistance, poor radiation efficiency, bad input impedance matching, and narrow frequency bandwidth [84-87]. Global optimization algorithms (e.g., GA or PSO) are introduced to mitigate these coupling effects and make performance trade-offs; however, implementations of these algorithms are so computationally intensive that the number of array elements is restricted to two or three. Further increase in the number of elements will lead to rapid increase in computational resources. In addition, limited physical insights can be gained from these brute-force optimization results.

In this section, we focus on utilizing (rather than mitigating) the strong mutual coupling between elements to design a closely-spaced, multiple-element parasitic antenna array. The design idea is based on our previous study of wave propagation in a closely-spaced parasitic array consisting of finite-height metal wires [88]. A surface wave propagating along the top of the wires is found to be the dominant propagation mechanism, and the phase velocity of the surface wave is extracted and correlated with array geometrical parameters. Motivated by this finding, we can turn the problem of designing a closely-spaced parasitic antenna into the design of a surface wave antenna. But different from traditional design which focuses on maximizing the antenna directivity, input impedance and radiation efficiency also need to be optimized for a closely-spaced surface wave antenna array.

5.2 Methodology

A 1-D closely-spaced, multiple-element parasitic array is shown in Fig. 5.1. Each array element is a copper wire of height h and radius r. The spacing between the elements is a, and the array size is L along the y dimension. All wires are located on a perfect electric conductor (PEC) ground. A voltage source is placed at the bottom of the left-most element. Given the array setup, a strong surface wave can be excited and guided along the structure in multiple frequency bands, which motivates us to explore the idea of a surface wave antenna design. Conventional surface wave antenna design requires the phase velocity of the wave to be carefully chosen so the maximum gain can be achieved for a given array size L [67]. For our array setup the surface wave phase velocity is strongly dependent upon the wire height and spacing, but is weakly dependent upon the wire radius. Therefore, we first simulate the antenna gain for different wire heights and spacing, in the hope of identifying the optimum phase velocity. The array size and wire radius are set at $L=0.5\lambda_0$ and $r=0.001\lambda_0$. Numerical Electromagnetics Code is used for the simulation.

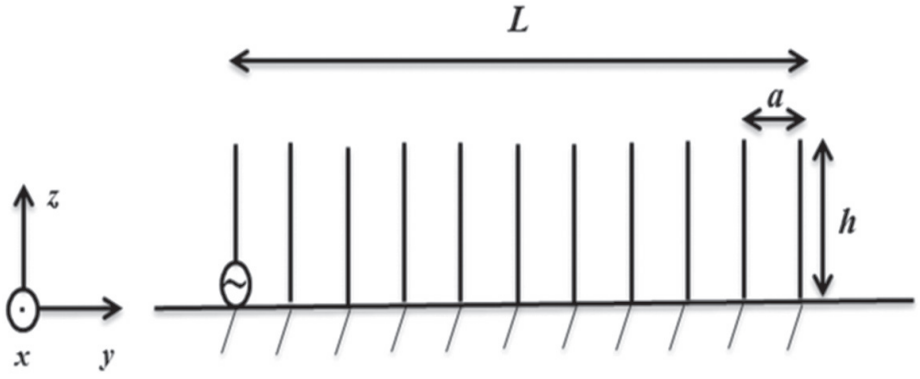

Fig. 5.1. 1-D closely-spaced, multi-element parasitic array setup.

Fig. 5.2 plots the simulated antenna gain on a decibel scale versus normalized spacing and height. It can be observed that for any given spacing a, there exists a unique wire height h, the pairing of which gives the maximum gain. For example, the pair of ($a=0.01\lambda_0$, $h=0.192\lambda_0$) results in the maximum gain of 12.23dB. Interestingly, it appears that this maximum gain value is independent of the choice of the inter-element spacing. As the spacing becomes larger, the wire height can be increased accordingly to maintain the peak gain value, leading to the maximum gain curve (in dark red color) in the plot. Our previous study indicates that a strong surface wave is excited and guided along the array when the spacing between elements is smaller than $0.1\lambda_0$. Furthermore, by increasing inter-element spacing the surface wave phase velocity will be reduced; conversely, increasing wire height will result in larger phase velocity. Therefore we expect the phase velocity to stay the same along the maximum gain curve due to the cancelling effects of two geometrical changes. For verification we extract the wave phase velocity for different optimum combinations of (a, h) using the ESPRIT algorithm. The extraction process has been presented in detail in [87] and will not be repeated here.

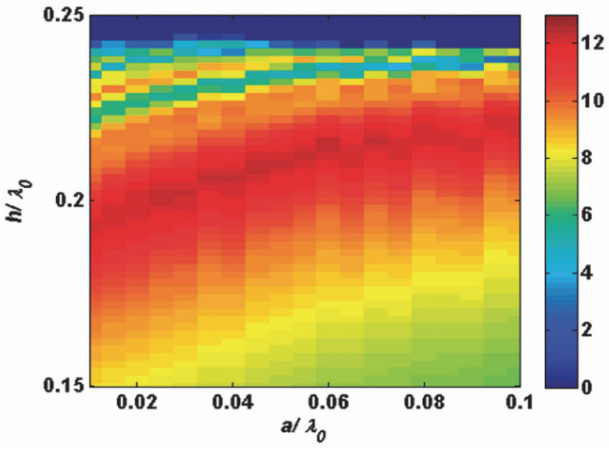

Fig. 5.2. Simulated gain for different wire spacing and height.

The extracted phase velocity is plotted versus spacing in Fig. 5.3, where the blue line is the mean value. The result is as expected and indeed there exists an optimum phase velocity ($0.67c_0$, c_0 is the speed of light) for this fixed size array ($L = 0.5\lambda_0$), which leads to the maximum gain. We also simulate and extract the optimum phase velocity for different array lengths, as shown in Fig. 5.4. The plot can be used to optimize antenna gain for this type of closely-spaced, short length array design. It can be observed that as the total length L decreases, the surface wave has to slow down to achieve the required terminal phase delay between the feeding and ending elements. This finding is consistent with conventional surface wave antenna design principle, but our optimum surface wave phase velocity does not meet the Hansen-Woodyard condition because of the short array size.

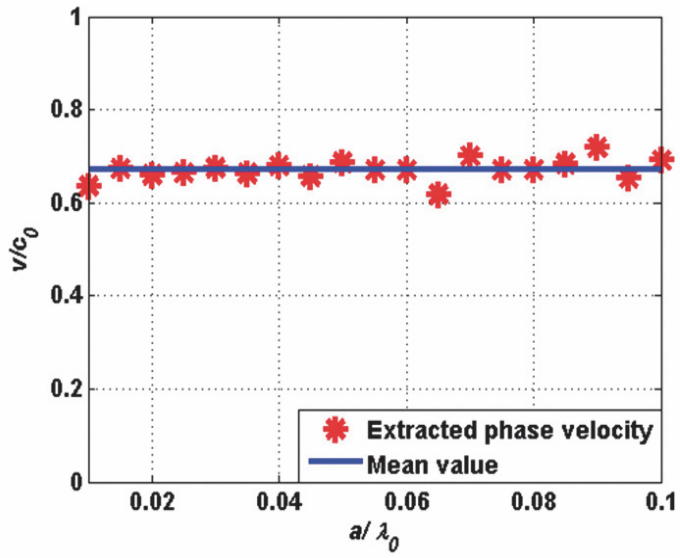

Fig. 5.3. Extracted optimum phase velocity for $L = 0.5\lambda_0$ parasitic array.

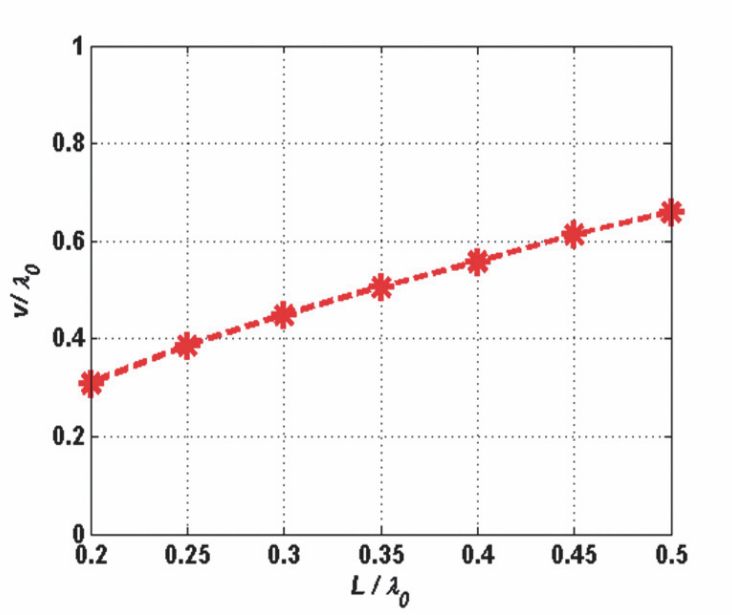

Fig. 5.4. Optimum phase velocity for different array lengths.

Next we investigate whether different optimum combinations of *a* and *h* lead to similar antenna input impedance. Fig. 5.5 depicts the simulated antenna input impedance versus spacing, in which the blue line is the input resistance and the red line is the input reactance. The heights of array elements are determined corresponding to the maximum gain curve in Fig. 5.2. It can be seen that even though the resistance increases and the reactance is less capacitive as the spacing becomes larger, it is challenging to match this surface wave antenna to a 50 Ohm transmission line. For example, the simulated input impedance for a uniform height, equal spacing array (a=0.05λ_0, h=0.204λ_0) is 6.53-j61.31Ohm, which results in poor impedance matching. For improvement we first increase the height of the feeding element *hf* from 0.204λ_0 to 0.238λ_0 in order to tune out the input reactance. Then we apply the folding technique [68] to boost up the resistance to 54.52 Ohm. Both simulation and measurement results will be presented in the next section.

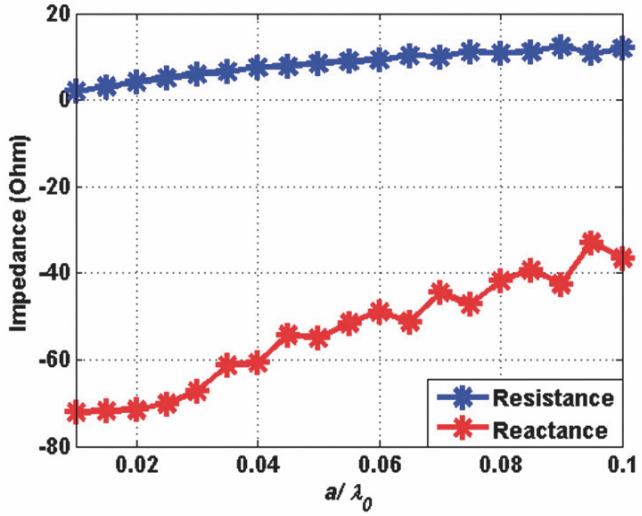

Fig. 5.5. Input Impedance for optimum combinations of *(a, h)*.

5.3 Simulation and Measurement

Following the idea presented in Section 2, we design, simulate and measure a 1-D closely-spaced surface wave antenna array at frequency 1.5 GHz. The array size *L* and wire radius *r* are set at 10 cm ($0.5\lambda_0$ at 1.5 GHz) and 0.05 cm ($0.0025\lambda_0$), respectively. We select the wire height h and spacing a to be 4.08cm ($0.204\lambda_0$) and 1 cm ($0.05\lambda_0$) so a uniform surface wave with optimum phase velocity $0.67c_0$ can be supported along the array. To improve impedance matching, we increase the height of the feeding element *hf* to 4.77cm ($0.238\lambda_0$) to tune out the input reactance and fold it once to boost up the resistance. Fig. 5.6 (a) shows the simulated reflection coefficient of the surface wave antenna and good impedance matching is achieved at 1.5 GHz. The simulated -10dB bandwidth is 50 MHz. We also simulate the gain and radiation pattern at the center frequency, as shown in Figs. 5.6 (b) and 5.7. The maximum simulated antenna gain and the front-to-back ratio are found to be 12.56 dB and 21.26 dB at 1.5GHz.

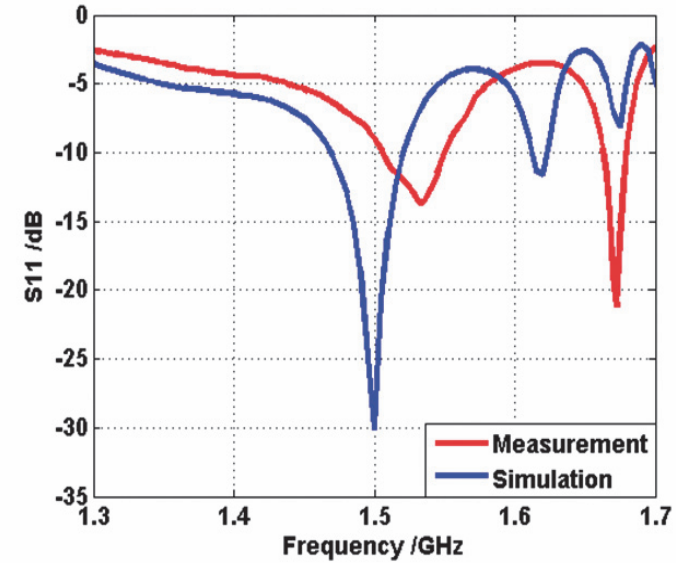

(a)

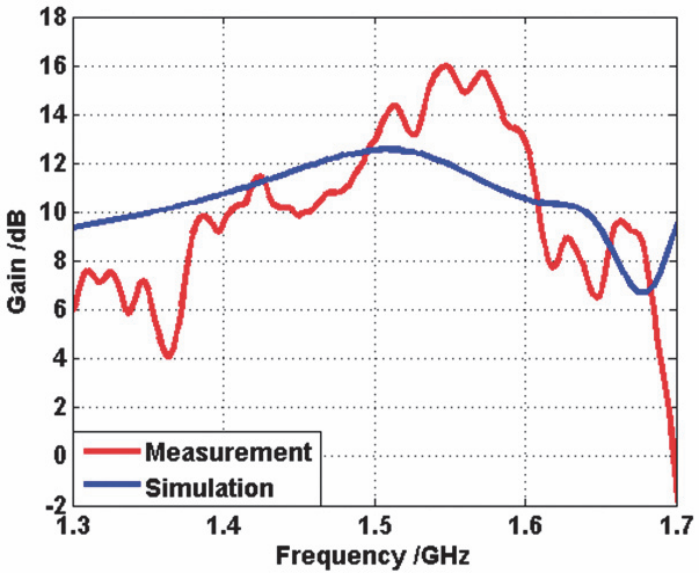

(b)

Fig. 5.6 (a) Simulated and measured reflection coefficients (b) Simulated and measured antenna gain.

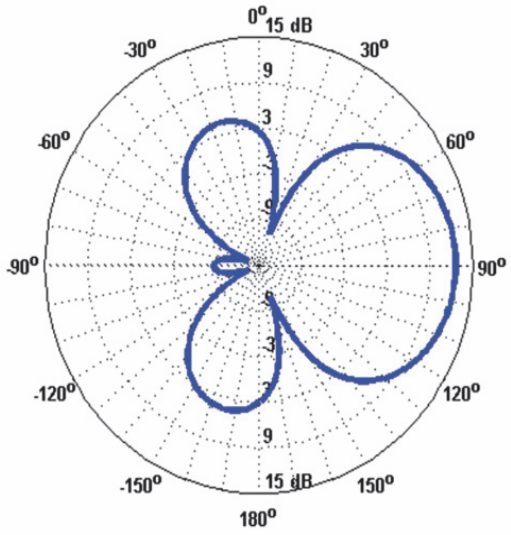

Fig. 5.7. Simulated far field radiation pattern.

A measurement prototype is next fabricated using 18 Gauge copper wires and placed on a 3*0.8m^2 steel plate, as shown in Fig. 5.8. A vector network analyzer is used to measure both reflection coefficients and gain. The measurement results are added in Fig 5.6 (a) and (b) for comparison. It can be observed that the measured resonant frequency shifts to 1.535 GHz, which can be contributed to the finite size of the ground plane. The measured -10 dB bandwidth is 45 MHz. The simulated and measured antenna gain show a similar trend within the frequency band. The peak measured gain is 16.29 dB at 1.55 GHz. More fluctuations can be observed in the measurement data due to the finite ground plane and the multipath effects.

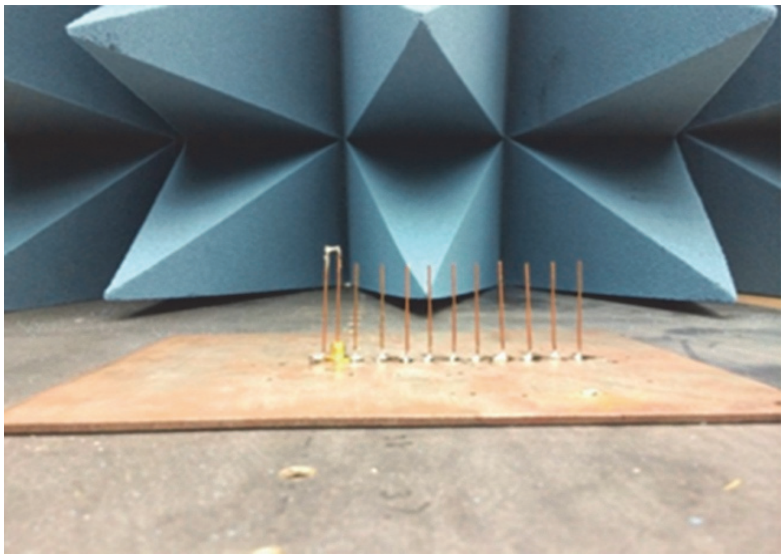

Fig. 5.8. A 10-element closely-spaced surface wave antenna prototype.

5.4 Summary

In this chapter a 1D closely-spaced, multi element parasitic array has been designed based on the surface wave propagation mechanism. It was shown that for a fixed length antenna array, there exists an optimum surface wave phase velocity which results in the maximum gain. The desired phase velocity can be achieved by carefully selecting the wire height and spacing. The antenna input impedance was also examined. It was shown that the input impedance needs to be boosted up using the folding technique. A full surface wave antenna array design with inter-element spacing of $0.05k_0$ was implemented, and the simulation results were similar to the measurements. The design provides a new way to implement a highly efficient and directive multi-element parasitic array.

CHAPTER SIX

Conclusions and Future Work

This dissertation presents a comprehensive study for broadband electromagnetic wave propagations and wearable antenna designs for WBAN applications. First wave propagations are investigated on a non-moving human body for LOS and NLOS channels using experimental and simulation methods. The ESPRIT algorithm is applied to extract the dominant propagation mechanism. Analytical models based on ground wave theories are derived and show good agreement with the experimental data. This research demonstrates that the dominant propagation mechanism is space wave and creeping wave for LOS and NLOS case, respectively. Then wave propagations on a moving human body are studied. The experimental platform and simulation modeling methods involving motion capture and VNA are proposed. Movement effects on wave propagations are examined. This research also found that the on-body creeping wave signals are able to classify human movement activities effectively. Finally, an electrically small wearable FCH antenna and antenna array are proposed for on-body applications. Human body effects on antenna performance are investigated. Highlights of this dissertation are discussed as follows.

1. While previous studies mainly focus on on-body signal propagation in several simple motion snapshots (e.g. 10 frames per second) during daily activities, in this dissertation, we are able to increase the sampling rate of motion snapshots to 120 frames per second by establishing an experiment platform to combine the motion capture system and VNA to simultaneously and continuously record the kinematical as well as EM data. The much higher sampling rate enables us to recreate the human simulation model with

arbitrary motions, and can provide a more accurate way to study EM propagations on moving humans.

2. While previous studies mainly focus on the on-body signal magnitude attenuation in the high frequency regime (e.g. 2.45 GHz), this dissertation covers broadband on-body signal transmission magnitude and phase data ranging from 300 MHz to 3GHz. This broad frequency range covers almost all medical frequency bands in current use. The additional phase data reveal valuable information on the wave propagation, and have been successfully utilized to classify motion activities and design surface wave antennas.

3. It is the first time to identify that the space wave is the dominant propagation mechanism for LOS on-body transmission. We have also verified that creeping wave is the dominant propagation mechanism for NLOS on-body transmission. With the identified dominant wave mechanism, we are able to select the optimal on-body channel and frequency band to design on-body antennas and enhance the transmission performance for the sake of link budgets. We can also use both wave mechanisms for motion recognition.

4. Previous studies mainly focus on optimizing conventional antenna performance (e.g. monopole) on the human body. In this dissertation we first apply the electrically-small FCH antenna in the context of WBAN. The FCH antenna couples on-body waves efficiently while the height is reduced by 80% compared to traditional monopoles. We introduce the 3D printing as a new antenna fabrication technique. The simulation and measurement results show very good agreement.

Future research can expand on the results of this study. Additional propagation mechanisms remain to be investigated for different on-body paths. For example, EM wave propagations on head, arms and lower limbs. Waves may also scatter from the body or

diffract from different cross-section levels. For wave propagations on moving humans, more complicated activities will be studied such as walking and running. Also the sample size of the experiments, such as the number of trials and the variety of human subjects, can be extended. For motion classifications, we will study the sensitivity of sensor position and orientation to the classification accuracy. In addition, more advanced signal processing techniques can be incorporated to extract physiological information such as heart beat rate from channels. For wearable antenna design, we are going to apply multi-element parasitic wire array technique to design multi-element parasitic FCH array and compare its radiation performance with single and two elements. We will also try to make FCH to be a textile antenna so it can be easily sewed on the clothes like a small button.

BIBLIOGRAPHY

[1] Body Area Network (BAN) Wikipedia [Online]. Available: http://en.wikipedia.org/wiki/Body_area_network

[2] Y. Hao and R. Foster, "Wireless body sensor networks for health-monitoring applications," *Physiol. Meas.*, vol. 29, no. 21, pp. 27-56, Oct. 2008.

[3] Hall, P. S., Hao, Y, "Antennas and propagation for body-centric wireless communications" Artech House, London, UK, 2006.

[4] J. M. Smith, "The doctor will see you ALWAYS," *IEEE Spectrum*, vol. 48, no.10, pp. 56-62, Oct. 2011.

[5] M. A. Hanson, H. C. Powell, A. T. Barth *et al*, "Body area sensor networks: challenges and opportunities," *Computer*, vol. 42, no. 1, pp. 58-65, Jan. 2009.

[6] G. K. Ragesh and K. Baskaran, "An overview of applications, standards and challenges in futuristic wireless body area networks," *International Journal of Computer Science Special Issues,* vol. 9, no.1, Jan. 2012.

[7] M. Patel and J. Wang, "Applications, challenges, and prospective in emerging body area networking technologies," *IEEE Wireless Communications,* vol. 17, no. 1, pp. 80–88, Feb. 2010.

[8] M. Chen, S. Gonzalez, A. Vasilakos, H. Cao, and V. Leung, "Body area networks: A survey," *ACM/Springer Mobile Network Application (MONET),* vol. 16, no. 2, pp.171 -193, Aug. 2010.

[9] Compliance & Regulatory Info Sheet Nr.1, Wireless Medical Devices & Connected Healthcare Applications, Jul. 2014. [Online]. Available: http://www.cetecom.com.

[10] P. S. Hall, Y. Hao, Y. I. Nechayv, "Antennas and propagations for on-body communication systems," *IEEE Antennas and Propagation Magazine*, vol. 49, no. 3, Jun. 2007.

[11] A. Fort, C. Desset, P. Wambacq And L. v. Biesen, "Indoor body-area channel model for narrowband communications," *IET Microwave, Antennas & Propagation*, vol. 1, no. 6, pp. 1197-1203, Dec. 2007.

[12] Y. I. Nechayev, P. S. Hall and Z. H. Hu, "Characterization of narrowband communication channels on the human body at 2.45 GHz," *IET Microwave, Antennas & Propagation*, vol. 4, no. 6, pp. 722-732, Jun. 2009.

[13] S. L. Cotton, Gareth. A. Conway and W. G. Scanlon, "A time-domain approach to the analysis and modeling of on-body propagation characteristics using synchronized measurements at 2.45 GHz," *IEEE Transactions on Antennas and Propagation*, vol. 57, no. 4, pp. 943-955, Apr. 2009.

[14] A. Fort, C. Desset, J. Ryckaert *et al.,* "Characterization of the Ultra-Wideband body area propagation channel," *IEEE International Conference on Ultra-Wideband*, Sept. 2005.

[15] T. Zasowski, F. Althaus, M. Stager *et al*, "UWB for noninvasive wireless body area networks: channel measurements and results," IEEE Conference on Ultra-Wideband Systems and Technologies, pp. 285- 289, Nov. 2003.

[16] A. Taparugssanagorn, C. Pomalaza-Ráez, A. Isola, R. Tesi, A.Rabbachin, M. Hämäläinen, J. Iinatti, "UWB Channel Modelling for Wireless Body Area Networks in Medical Applications," The 3rd International Symposium on Medical Information and Communication Technology, Montreal, Canada, 2009.

[17] N. Chahat, G. Valerio, M. Zhadobov and R. Sauleau, "On-body propagation at 60 GHz," *IEEE Transactions on Antennas and Propagation,* vol. 61, no. 4, Apr. 2013.

[18] A. Christ, W. Kainz, E. G. Hahn et al, "The Virtual Family—development of surface-based anatomical models of two adults and two children for dosimetric simulations," *Physics in Medicine and Biology,* vol. 55, no. 2, pp. N23-38, Jan. 2010.

[19] J. Ryckaert, P. De Doncker, R. Meys, A. de Le Hoye and S. Donnay, " Channel model for wireless communication around human body," *Electronic Letters*, vol. 40, no. 9, pp. 543-544, Apr. 2004.

[20] G. A. Way, W. G. Scanlon, S. L. Cotton and M. J. Bentum, "An analytical path-loss model for on-body radio propagation," URSI International Symposium on Electromagnetic Theory, pp. 332-335, Aug. 2010.

[21] R. Chandra and A.J. Johansson, "Effect of frequency, body parts and surroundings on the on-body propagation channel around the torso," 34th Annual International Conference of the IEEE EMBS, pp. 4533-4536, San Diego, California, Aug. 2012.

[22] G. A. Conway and W. G. Scanlon, "Antennas for over-body-surface communication at 2.45 GHz," *IEEE Transactions on Antennas and Propagation,* vol. 57, no. 4, pp. 844-855, Apr. 2009.

[23] M. Grimm and D. Manteuffel, "Electromagnetic wave propagation on human trunk models excited by half-wavelength dipoles," Loughborough Antennas & Propagation Conference (LAPC), pp. 493-496, Loughborough, UK, Nov. 2010.

[24] R. Chandra and A. J. Johansson, "An elliptical analytic link loss model for wireless propagation around the human torso," 6th European Conference on Antennas and Propagation (EUCAP), pp. 3121-3124, Mar. 2012.

[25] R. Chandra and A. J. Johansson, "An analytical link-loss model for on-body propagation around the body based on elliptical approximation of the torso with arms' influence included," *IEEE Antennas and Propagation Letters,* vol. 57, pp. 528-531, Apr. 2013.

[26] R. Chandra and A. J. Johansson, "A link loss model for the on-body propagation channel for binaural hearing aids," *IEEE Transactions on Antennas and Propagation,* vol. 61, no. 12, pp. 6180-6190, Dec. 2013.

[27] T. Alves, B. Poussot, and J.-M. Laheurte, "Analytical propagation modeling of BAN channels based on the creeping-wave theory," *IEEE Transactions on Antennas and Propagation*, vol. 59, no. 4, pp. 1269–1274, Apr. 2011.

[28] A. Fort, F. Keshmiri, G. R. Crusats, C. Craeye, and C. Oestges, "A body area propagation model derived from fundamental principles: Analytical analysis and comparison with measurements," *IEEE Transactions on Antennas and Propagation,* vol. 58, no. 2, pp. 503–514, Feb. 2010.

[29] G. Roqueta, A. Fort, C. Craeye, and C. Oestges, "Analytical propagation models for body area networks," in Proc. IET Seminar Antennas Propagations on Body-Centric Wireless Communications, pp. 90–96, Apr. 2007.

[30] A. M. Eid and J. W. Wallace, "Accurate modeling of body area network channels using surface-based method of moments," *IEEE Transactions on Antennas and Propagation,* vol. 59, no. 8, pp. 3022–3030, Aug. 2011.

[31] A. Lea, P. Hui, J. Ollikainen and R. G. Vaughan, "Propagation between on-body antennas," *IEEE Transactions on Antennas and Propagation,* vol. 57, no. 11, pp. 3619-3627, Nov. 2009.

[32] M. Grimm and D. Manteuffel, "Evaluation of the Norton Equations for the development of body-centric propagation methods," 6th European Conference on Antennas and Propagation (EUCAP), pp. 311-315, Mar. 2012.

[33] M. Grimm and D. Manteuffel, "Norton surface waves in the scope of body area networks," *IEEE Transactions on Antennas and Propagation,* vol. 62, no. 5, pp. 2616-2613, May 2014.

[34] C. Balanis and L. Peters, Jr., "Aperture radiation from an axially slotted elliptical conducting cylinder using geometrical theory of diffraction," *IEEE Transactions on Antennas and Propagation,* vol. AP-17, no. 4, pp. 507–513, Jul. 1969.

[35] P. H. Pathak, N. Wang, W. D. Burnside and R.G. Kouyoumjian, "A uniform GTD solution for the radiation from sources on a convex surface," *IEEE Transactions on Antennas and Propagation,* vol. 29, no. 4, pp. 609-622, Jul. 1981.

[36] J. R. Wait, "On the excitation of electromagnetic surface waves on a curved surface," *IRE Transactions on Antennas and Propagation,* pp. 445-448, Jul. 1960.

[37] J. R. Wait, "The ancient and modern history of EM ground-wave propagation," *IEEE Antennas and Propagation Magazine,* vol. 40, no. 5, pp. 7-24, 1998.

[38] K. A. Norton, "Propagation of radio waves over a plane earth", *Nature*, pp. 954-955, Jun. 1935.

[39] K. A. Norton, "The propagation of radio waves over the surface of the earth and in the upper atmosphere," *Proceedings of the Institute of Radio Engineers,* vol. 25, no. 9, pp. 1203-1236, Sept. 1937.

[40] K. A. Norton, "The calculation of ground-wave field intensity over a finitely conducting spherical earth," *Proceedings of the Institute of Radio Engineers,* pp. 623-642, Dec. 1941.

[41] P. R. Bannister, "Extension of quasi-static range finitely conducting earth-image theory techniques to other ranges," *IEEE Transactions on Antennas and Propagation,* vol. 26, no. 3, pp. 507-508, May 1978.

[42] P. R. Bannister, "Extension of finitely conducting earth-image-theory results to any range". Technical Report, 6885, NUSC Naval Underwater Systems Center, New London, CT, USA, 1984.

[43] Z. Nie, J. Ma, H. Cheng and L. Wang, "Statistical characterization of the dynamic human body communication channel at 45 MHz," 35th Annual International Conference of the IEEE EMBS, pp. 1206-1209, Osaka, Japan, Jul. 2013.

[44] T. Uusitupa and T. Aoyagi, "Analysis of dynamic on-body communication channels for various movements and polarization schemes at 2.45 GHz," *IEEE Transactions on Antennas and Propagation,* vol. 61, no. 12, pp. 6168-6179, Dec. 2013.

[45] A. Taparugssanagorn, B. Zhen, R. Tesi *et al.* "A UWB WBAN channel model based on a pseudo-dynamic measurement," *Annals of Telecommunications*, vol. 66, no. 3, pp. 177-185, Apr. 2011.

[46] N. Yamamoto, N. Shirakata, D. kobayashi *et al*, "BAN radio link characterization using an arm-swinging dynamic phantom replicating human walking motion," *IEEE Transactions on Antennas and Propagation,* vol. 61, no. 8, pp. 4315-4326, Aug. 2013.

[47] M. Gallo, P. S. Hall, Q. Bai *et al*, "Simulation and measurement of dynamic on-body communication channels," *IEEE Transactions on Antennas and Propagation,* vol. 59, no. 2, pp. 623-630, Feb. 2011.

[48] S. Swisaenyakorn, S. W. Kelly and J. C. Batchelor, "A study of factors affecting wrist channel characteristics for walking postures using motion capture," *IEEE Transactions on Antennas and Propagation,* vol. 62, no. 4, pp. 2231-2237, Apr. 2014.

[49] T. Aoyagi, Iswandi, M. Kim *et al,* "Body motion and channel response of dynamic body area channel," Proceedings of the 5th European Conference on Antennas and Propagation (EUCAP), Rome, pp. 3138-3142, Apr. 2011.

[50] M. Quwaider and S. Biswas, "Body posture identification using hidden Markov model with a wearable sensor network," Proceedings of the ICST 3rd International Conference on Body Area Networks, Brussels, Belgium, 2008.

[51] M. O. Munoz, R. Foster and Y. Hao, "Exploring physiological parameters in dynamic WBAN channel," *IEEE Transactions on Antennas and Propagation,* vol. 62, no. 10, pp. 5268-5281, Oct. 2014.

[52] S. Wang and G. Zhou, "A review on radio based activity recognition," *Digital Communications and Networks,* vol. 1, no. 1, pp. 20-29, Feb. 2015.

[53] L. Akhoondzadeh-Asl and P. S. Hall, "Surface wave and creeping waves excitation by body-worn antennas," Loughborough Antennas and Propagation Conference (LAPC), Loughborough, pp. 48-51, Nov. 2010.

[54] L. Akhoondzadeh-Asl, I. Khan and P. S. Hall, "Polarization diversity performance for on-body communication applications," *IET Microwave, Antennas and Propagation*, vol. 5, no. 2, pp. 232-236, 2011.

[55] Q. Wang, R. Hahnel, H. Zhang and D. Plettemeier, "On-body directional antenna design for in-body UWB wireless communication," Proceedings of the 6th European Conference on Antennas and Propagation (EUCAP), pp. 1011-1015, Jan. 2011.

[56] Y. Yao, J. Zhen and Z. Feng, "Diversity measurements for on-body channels using a tri-polarization antenna at 2.45 GHz," *IEEE Antennas and Wireless Propagation Letters*, vol. 11, pp. 1285-1288, Oct. 2012.

[57] E. F. Sundarsingh, S. Velan, M. Kanagasabai *et al,* "Polygon-shaped slotted dual-band antenna for wearable applications," *IEEE Antennas and Wireless Propagation Letter,* vol. 13, pp. 611-613, Mar. 2014.

[58] C. Deng, X. Liu, Z. Zhang and M. M. Tentzeris, "A miniascape-like triple-band monopole antenna for WBAN applications," *IEEE Antennas and Wireless Propagation Letter,* vol. 11, pp. 1330-1333, Nov. 2012.

[59] Q. H. Abbasi, M. Rehman, X. Yang *et al*, "Ultrawideband band-notched flexible antenna for wearable applications," *IEEE Antennas and Wireless Propagation Letter,* vol. 12, pp. 1606-1609, Dec. 2013.

[60] C. M. Lee and C. W. Jung, "Radiation-pattern-reconfigurable antenna using monopole-loop for Fitbit Flex wristband," *IEEE Antennas and Wireless Propagation Letter,* vol. 14, pp. 269-272, Oct. 2014.

[61] B. Ivsic, D. Bonefacic and J. Bartolic, "Considerations on embroidered textile antennas for wearable applications," *IEEE Antennas and Wireless Propagation Letter,* vol. 12, pp. 1708-1711, Jan. 2013.

[62] T, F. Kennedy, P. W. Fink, A. W. Chu *et al,* "Body-worn E-textile antennas: the Good, the Low-mass, and the Conformal," *IEEE Transactions on Antennas and Propagation,* vol. 58, no. 4, pp. 910-918, Apr. 2009.

[63] S. Agneessens and H. Rogier, "Compact half diamond dual-band textile HMSIW on-body antenna," *IEEE Transactions on Antennas and Propagation,* vol. 62, no. 5, pp. 2374-2381, May 2014.

[64] S. Velan, E. F. Sundarsingh, M. Kanagasabai *et al*, "Dual-band EBG integrated monopole antenna deploying fractal geometry for wearable applications," *IEEE Antennas and Wireless Propagation Letter,* vol. 14, pp. 249-252, Sept. 2014.

[65] M. R. Islam and M. Ali, "A 900 MHz beam steering parasitic antenna array for wearable wireless applications," *IEEE Transactions on Antennas and Propagation,* vol. 61, no. 9, pp. 4520-4527, Aug. 2013.

[66] L. Akhoondzadeh-Asl, Y. Nechayev, P. S. Hall and C. C. Constantiou, "Parasitic array antenna with enhanced surface wave launching for on-body communications," *IEEE Transactions on Antennas and Propagation,* vol. 61, no. 4, pp. 1976-1985, Apr. 2013.

[67] H. W. Ehrenspeck and H. Poehler, "A new method for obtaining maxi-mum gain from Yagi antennas," *IRE Transactions on Antennas and Propagation*, vol. 7, pp. 379-386, 1959.

[68] C. A. Balanis, Antenna Theory: Analysis and Design, Wiley, Hoboken, NJ, 2005.

[69] S. Lim and H. Ling, "Design of thin, efficient, electrically small antenna using multiple foldings", *Electronic Letters,* vol. 42, no.6, pp. 895–896, Aug. 2006.

[70] R. Fu, Y. Ye, N. Yang and K. Pahlavan, "Doppler spread analysis of human motions for body area network application," IEEE 22nd International Symposium on Personal, Indoor and Mobile Radio Communications," pp. 2209-2213, Sept. 2011.

[71] R. D'Errico and L. Ouvry, "Doppler characteristics and correlation properties of on-body channels," Proceedings of the 5th European Conference on Antennas and Propagation (EUCAP), Rome, pp. 2977-2981, Apr. 2010.

[72] L. Liu, S. Roy, F. Ouitin *et al,* "Statistical characterization and modeling of Doppler spectrum in dynamic on-body channels," *IEEE Antennas and Wireless Propagation Letters*, vol. 12, pp. 186-189, Mar. 2013.

[73] M. Hirvonen, C. Bohme, D. Severac and M. Maman, "On-body propagation performance with textile antennas at 867 MHz," *IEEE Transactions on Antennas and Propagation,* vol. 61, no. 4, pp. 2195-2199, Apr. 2013.

[74] D. Xue, B. A. Garner and Y. Li, "Extraction of on-body creeping wave mechanisms using the EPRIT algorithm," *Microwave & Optical Technology Letter*, vol. 57, no. 4, pp. 868-871, Apr. 2015.

[75] Internet resources of biological tissue properties [Online]. Available: http://niremf.ifac.cnr.it/tissprop/

[76] M. Muller, *Information Retrieval for Music and Motion*, Springer, 2007.

[77] H. Sakoe and S. Chiba, "Dynamic programming algorithm optimization for spoken word recognition," *IEEE Transactions on Acoustics, Speech*, *Signal Process*., vol. 26, pp. 43-49, Feb. 1978.

[78] A. Corradini, "Dynamic time warping for off-line recognition of a small gesture vocabulary," IEEE ICCV Workshop on Recognition, Analysis, and Tracking of Faces and Gestures in Real-Time Systems, Vancouver, BC, pp.82 – 89, Jul. 2011.

[79] G. Smith, K. Woodbridge and C. Baker, "Radar micro-Doppler signature classification using dynamic time warping*," IEEE Transactions on Aerospace Electronic System*s, Vol. 46, pp. 1078 - 1096, Jul. 2010.

[80] S. R. Best, "The radiation properties of electrically small folded spherical helix antennas," *IEEE Transactions on Antennas & Propagation,* vol. 52, no.4, pp. 953-960, Apr. 2004.

[81] S. R. Best, A study of the performance properties of small antennas," technical report, The MITRE Corporation, Oct. 2007.

[82] S. Lim, R. L. Rogers and H. Ling, "A tunable electrically small antenna for ground wave transmission," *IEEE Transactions on Antennas & Propagation,* vol. 54, no.2, pp. 417-421, Feb. 2006.

[83] K. Shinyama and S. Fujita, "Study of the electrical properties of a biodegradable plastic," Proceedings of the 7th International Conference on Properties and Applications of Dielectric Materials, pp. 707-710, Jun. 2003.

[84] T. H. O'Donnell and A. D. Yaghjian, "Electrically small superdirective arrays using parasitic elements," IEEE Antenna & Propagation International Symposium, Albuquerque, NM, pp. 3111-3114, Jul. 2006.

[85] Z. Bayraktar, P. L. Werner and D. H. Werner, "The design of miniature three-element stochastic Yagi-Uda arrays using particle swarm optimization", *IEEE Antennas Wireless & Propagation Letters*, vol. 5, no. 1, pp. 22-26, Mar. 2006.

[86] S. Lim and H. Ling, "Design of electrically small, pattern reconfigurable Yagi antenna," *Electronic Letters,* vol.43, no. 24, pp. 1326-1327, Dec. 2007.

[87] D. Arceo and C. A. Balanis, "A compact Yagi-Uda antenna with enhanced bandwidth," *IEEE Antennas Wireless & Propagation Letters* vol. 10, pp. 442-445, May 2011.

[88] Y. Li, "Wave propagation along a one-dimensional metal cut-wire array," *Journal of Electromagnetic Waves Applications*, vol. 27, pp. 3-13, Oct. 2013.